UNIVERSITÀ DEGLI STUDI DI PADOVA

Dipartimento di Fisica e Astronomia "Galileo Galilei"

Master Degree in Astrophysics and Cosmology

Final Dissertation

A systematic investigation of candidate high-redshift galaxies in JWST deep fields

Thesis supervisor

Prof. Giulia Rodighiero

Thesis co-supervisors

Dr. Laura Bisigello, Dr. Andrea Grazian

Candidate

Giorgia Girardi

Academic Year 2022/23

A systematic investigation of candidate high-redshift galaxies in JWST deep fields.

Abstract

Thanks to the deep JWST survey carried in the SMACS 0723 cluster, there has been the discovery of an interesting population of objects not observed by the previous optical telescope, such as HST, and whose nature is still under investigation. The aim of this work is to compare the physical parameters obtained through the spectral energy distribution modelling technique applied on a sample of 19 galaxies present in this field, chosen for their very red near-infrared colours, being undetected at $\lambda_{obs} < 2\mu$m. Aiming to provide an accurate systematic investigation, the photometric analysis of these sources has been carried out through several software tools. Hence, this work intends to find discrepancies among the results obtained through the different photometric analysis, confronting the outputs obtained, as well as to check their consistency, in order to understand how much the choice of the technique can influence the results and therefore our understanding of the nature of high-redshift galaxies properties. In a future perspective, this kind of investigation can be enlarged adding various others photometric databases of deep JWST surveys, along with considering alternative tools for both photometric analysis and spectral energy distribution fitting.

Contents

CONTENTS

Executive Summary

In this work, in Chapter 1 an overview regarding the first year of activity of the James Webb Space Telescope is provided, focusing on the results that might be in disagreement with the standard ΛCDM model. These concern the ultraviolet (UV) luminosity function retrieved by high-redshift galaxies, at $z > 10$, which is found to exceed the prediction of various cosmological models focused on the primeval Universe. However, we report some complementary works that furnish possible physical explanations to account for this overabundance of galaxies at $z \gtrsim 10$, without having to discard the actual majorly accepted cosmological model. Given the importance of understanding if the detection of these high-redshift candidates are confirmed, and therefore if their physical properties are robust, the aim of this thesis is to compare the results obtained from different photometric techniques and starting from different images reduction, to investigate the importance of the analysis choices in the estimation of the galaxies' parameters.

In Chapter 2, the procedure employed in this work to obtain the galaxies' physical parameters is described. First, the sample of candidates analyzed in this work is presented, explaining how they were previously chosen in the study carried on by Rodighiero et al. [1]. In addition, some brief excursions are made, in order to present the belonging field of these sources (Section 2.1.1) and the techniques to retrieve the photometric redshift (Section 2.1.2). Secondly, the photometric tools and the spectral energy distribution (SED) fitting code applied to recover the results are introduced through a concise overview, explaining how they were employed for the analysis. This SED fitting code has been run over the fluxes obtained through several photometric analysis, specifically 3 of them: the two options of the `Sextractor` software (Section 2.2.1), i.e. the total (or Auto) flux and the aperture flux, and the photometry tool by Marasco et al. [2] (hereafter Marasco tool, Section 2.2.2). The `Sextractor` Auto option provides directly the total estimated flux of the sources, while the Aperture one provides the fluxes at the various radii, having to correct them in second moment to properly account for the missed flux lying outside the aperture size (the so called aperture correction).

Ultimately, in Chapter 3 the results of this analysis are reported, along with a discussion regarding the difference among physical parameters estimated through the SED fitting technique, employing the `Bagpipes` code, highlighting the inconsistencies or the agreement between the estimations. Two out of the three photometries resulted in agreement, therefore showing a consistency even changing the methods used, while the discrepancy of the third method is probably due to the choice of the aperture size (see Section 3.1).

The importance of future spectroscopic confirmations is also underscored, in order to be able to really draw robust conclusions regarding the nature of these very red, high-redshift galaxies and therefore about our understanding of the physics behind the evolution of the Universe.

Chapter 1

The *James Webb Space Telescope*

1.1 James Webb science program

The James Webb Space Telescope[1] (JWST) represents a profound leap forward in the field of astrophysics, a testament to the unceasing evolution of astronomical knowledge and technological prowess. The story of JWST's conception and development is deeply entwined with its predecessor, the Hubble Space Telescope (HST), and the remarkable scientific revelations it unveiled.

In the years leading up to its launch in 1990, HST was anticipated to make relatively modest contributions to the study of galaxies at redshifts $z \gtrsim 2$. The prevailing assumption was that distant galaxies, due to their presumed large and featureless nature, would offer little advantage for study through HST's high spatial resolution, characterized by diffraction-limited capabilities. However, as the initial deep exposures were obtained with HST, it became evident that this presumption was inherently flawed. Combining data from HST and the Spitzer Space Telescope has enabled simultaneous measurements of the rest-frame ultraviolet (UV) and optical SEDs of distant galaxies, allowing to infer star-formation rates (SFRs) and stellar masses of early-forming galaxies, unveiling that remote galaxies surprisingly possess small and compact star-forming regions [3]. Even the faintest and most remote galaxies were found to be barely resolvable by HST, marking a transformative discovery in the world of astrophysics.

This realization ignited a series of extensive targeted observations of the high redshift universe, culminating in the groundbreaking Hubble Deep Field (HDF) and

---

[1]Official website: https://webb.nasa.gov/

subsequent follow-on programs. These programs pushed HST to the limits of its sensitivity, revealing a multitude of galaxies that, unfortunately, proved too faint for spectroscopic follow-up using contemporary facilities. To address this challenge, astronomers pioneered techniques to estimate the "photometric" redshift of these galaxies by fitting assumed template spectra to their broadband colors (see Section 2.1.2).

The most common of these techniques is the one based on the Lyman Break. However, this method does not account for the emission obscured by dust, thus the identification carried on with this technique tends to exclude the more massive galaxies, given that they are the ones presenting the major dust content [4].

Exploiting different techniques, such as the one proposed by Wang et al. [5] (explained in Section 2.1.2), and thanks to the Spitzer space telescope, a population of red galaxies completely missed even by HST has been found. But it was not until the arrival of JWST that the nature of these very red sources has started being unrevealed.

The limitations of this "poor man's spectroscopy" became increasingly evident, prompting the need for a more advanced and capable instrument. It was this need, particularly in the context of exploring the early universe, that fueled the conceptualization of JWST, conceived as the natural successor to HST [6].

This visionary observatory was designed to unravel the Universe's first generations of stars, pushing the boundaries of what was achievable beyond Hubble's capabilities. These nascent stars and galaxies, residing at distances so vast that their light had been stretched all over into the infrared spectrum, had remained hidden from human observation up to its launch.

Furthermore, JWST's significance is not limited to studying the origins of stars and galaxies. It has four primary objectives, each with profound implications for our understanding of the cosmos [7, 8, 9]:

1. *The End of the Dark Ages: First Light and Reionization.* JWST's first science goal is to detect the light from the Universe's first objects that coalesced after the Big Bang, marking the end of the dark ages. Being capable of observing at wavelengths longer than 1 micron is essential for studying these first galaxies. The search for objects that reionized the Universe is also on the agenda, necessitating both imaging and spectroscopic capabilities.

2. *The Assembly of Galaxies.* JWST aims to study how galaxies evolved from their first light origins to the diverse galaxy types seen today. This goal demands

high spatial resolution and spectroscopy, as well as the ability to observe many galaxies simultaneously.

3. *Probing Star Birth and Formation.* The observatory's infrared sensors can penetrate the dust and gas shrouding stellar nurseries, revealing the intricacies of star formation and the production of heavy elements, up to the genesis of planetary systems. It will provide high sensitivity and spatial resolution in the 5-28 μm range, essential for understanding the birth of stars and planets.

4. *Exploring the Origin and Evolution of Planetary Systems, including the search for life.* JWST has the potential to directly detect large planets around nearby stars, while its high resolution offers insights into planetary system behavior during their formation. With the discovery of exosolar planets, JWST will characterize them and study how planetary systems form. Its mid-infrared imager will help explore low surface brightness objects, and coronagraphic imaging will be pivotal in finding and understanding giant planets.

Apart from that, it will also be able to help determining the Geometry, Age and Fate of the Universe: JWST is poised to contribute significantly to the study of the accelerating expansion of the Universe, driven by the presence of dark energy [10].

To meet its ambitious scientific goals, JWST had to overcome several challenges, requiring revolutionary developments in telescope technology, such as the primary mirror segment assemblies and wavefront sensing and control. Its journey from conception to reality spanned over two decades and involved a distributed team of experts across diverse engineering disciplines. The observatory's design, with its 6.5 meter primary mirror composed of 18 hexagonal segments, each supported by an adjustable backplane structure, was a radical departure from conventional space telescope architectures. To operate at cryogenic temperatures, JWST utilizes passive cooling through a five-layer sunshield, while its system and instruments, which include infrared-sensing cameras and spectrometers, needed to be custom-developed for the rigors of infrared observations. Its structure can be appreciated in Figure 1.1.

Figure 1.1: In this figure, the structure of JWST observatory is shown.

Credits: https://science.nasa.gov/mission/webb/spacecraftoverview/
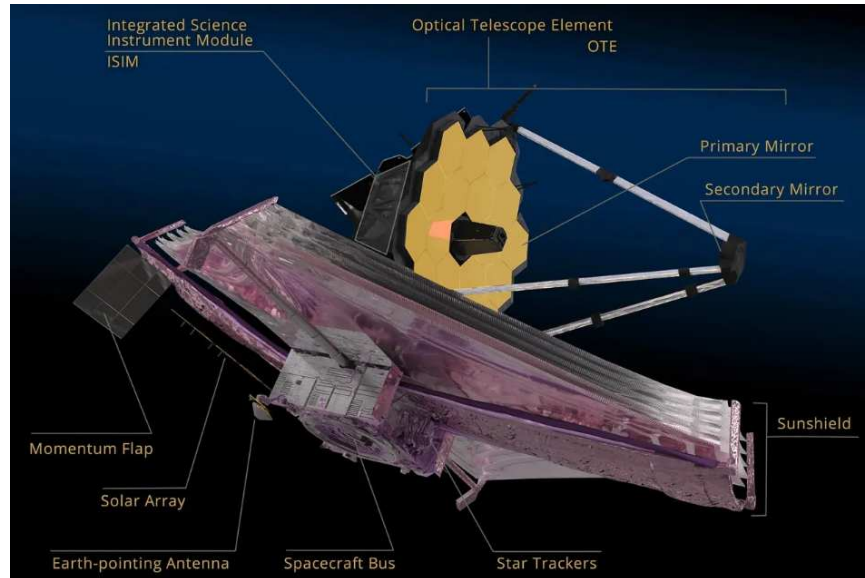
In conclusion, JWST stands as a legacy to the remarkable evolution of astronomical knowledge and technological progress, opening up unprecedented opportunities to explore the universe. Its origins are deeply rooted in the unforeseen revelations brought about by HST, challenging long-held assumptions about the nature of distant galaxies. As it embarks on its mission, JWST is already performing beyond its design objectives, promising even higher sensitivity and more stable observations than originally planned [11, 12].

Its mission also aligns with the leading research topics in modern astrophysics, offering insights into the solar system, exoplanets, star formation, galaxy evolution and cosmology, providing a foundation for understanding the grand objectives of studying the origins of life, the birth of stars and galaxies and the mysteries of the universe's earliest light [13].

1.2 James Webb instrumentation

JWST is a collaborative effort, led by the United States' National Aeronautics and Space Administration (NASA) in partnership with the European Space Agency (ESA) and the Canadian Space Agency (CSA). The project's partnership is divided with 80% contributed by NASA, 15% by ESA, and 5% by CSA, with NASA's Goddard Space

Flight Center (GSFC) taking the lead in managing the mission.

To address the inquiries mentioned in the previous section effectively, a highly capable telescope is essential, thus the JWST has been constructed to be a groundbreaking undertaking featuring several pioneering technologies that will delve deeper into the cosmos, beyond the capabilities achievable by its predecessors, Spitzer and Hubble.

Some of its key components and features include:

- An enormous 18-segmented primary mirror, measuring 6.5 meters in diameter and coated in gold. This mirror boasts adjustable optics and integrated wavefront sensing capabilities.

- A colossal sunshield, measuring 21×14 square meters, constructed from five layers of Kapton material, each 25 to 50 micrometers thick. This sunshield passively cools the observatory to a cryogenic temperature of $\sim 35/40$ Kelvin, necessary to achieve the sensitivity required to meet its scientific objectives.

- An array of advanced instruments optimized for infrared observations, featuring high-resolution imaging, multiplexed spectroscopy and coronagraphy observing modes. JWST's sensitivity spans from the red part of the visible spectrum at 0.6 microns to mid-infrared wavelengths of 28.8 microns.

- A primary mission goal of 10 years, positioning the observatory in a thermally stable solar orbit at the second Lagrange point.

The launch and deployment of JWST represented a significant technical challenge. In its fully deployed configuration, the observatory spans over 10 meters in two dimensions and over 20 meters in the third dimension, resulting in the problem that conventional launch vehicles are unable to transport such a large primary mirror. The constraints of the ESA's Ariane 5 launch vehicle, with a diameter of 4.6 meters and a length of 16.2 meters, necessitated careful engineering to allow the observatory to fit within the rocket. This challenge has led to the development of a new innovative deployable design that enables its launch within Ariane 5 rocket: following launch, JWST's components unfold and deploy, including the solar panel and the huge primary mirror.

As an infrared observatory, JWST's performance is critically contingent on maintaining a stable thermal environment while effectively controlling stray light. Its sunshield serves as the primary defense against radiation from the Sun, Earth, Moon and other stray light sources and it is expected to reduce incident radiation on the

observatory's top side by a factor of 10 million, decreasing it to milliwatt levels. The design also incorporates various elements to mitigate stray light from celestial objects, zodiacal light within the solar system, the Milky Way, and the observatory's own self-emission. These elements include a "frill" around the primary mirror, a thermal shield called "bib" beneath the primary mirror, a baffle, pupil mask and field stop in other parts of the optical system. JWST's optics are engineered to provide diffraction-limited performance at wavelengths above 2 microns, ensuring excellent image quality from the optics to the science instruments across most of its wavelength range. In addition, to fully leverage the capabilities of its high-resolution instrumentation, precise wavefront sensing and alignment are essential to ensure.

The detectors for JWST are cooled to temperatures below 40 Kelvin to minimize dark current and read noise, especially in the 0.6 to 5 micrometer range. By positioning JWST in an L2 orbit and with the help of the sunshield, passive radiators effectively cool the Integrated Science Module so that active cooling is only required for detectors operating at wavelengths longer than 5 micrometers. The success of the sunshield and the outer shell cooling of the Spitzer Space Telescope corroborates the feasibility of cooling JWST detectors to approximately 35 Kelvin without active cooling.

Unlike the HST, JWST's instruments are not upgradable. Consequently, the initial suite of instruments has been meticulously designed with cutting-edge technologies to ensure their competitiveness throughout the mission's lifespan.

In line with its grand objectives, the JWST provides four groundbreaking instruments, each of which plays a vital role in advancing our understanding of cosmic reionization science. All of the technical details of these instruments, which are MIRI [14], NIRCam [15], NIRISS [16] and NIRSpec [17], are taken by the work of Robertson et al. [3], Rieke et al. [7] and Kalirai et al. [13].

1.2.1 MIRI

The Mid-Infrared Instrument (MIRI) represents a collaborative effort with an European consortium led by the United Kingdom Astronomy Technology Center and the Jet Propulsion Laboratory. The detectors in MIRI must operate at temperatures below 7 Kelvin, necessitating an electric cryocooler for additional cooling beyond what passive radiators can provide. MIRI offers a diverse array of observing modes, including imaging, coronagraphy, and spectroscopy, which together enable a wide range of scientific investigations. The detectors used in MIRI are 144 conduction devices made of arsenic-doped silicon.

MIRI stands as a versatile instrument, offering four primary capabilities:

1. *Photometric Imaging*: MIRI extends JWST sensitivity into the mid-infrared, covering wavelengths from 4.9 micrometers up to 28.8 micrometers. High-resolution imaging is available across the range of 5.0 to 27.5 micrometers, with a fine pixel scale of 0.11 arcseconds, over a field of view spanning $74'' \times 113''$. This pixel scale surpasses the resolution of Spitzer's InfraRed Array Camera (IRAC), which presents a pixel scale of $1.22''$, and Multi-Band Imaging Photometer (MIPS), with a pixel scale $\approx 2.5''$, and even Hubble's Wide Field Camera 3 (WFC3/IR), operating in the near-infrared. The sensitivity of MIRI is generally $\approx 1 - 2$ orders of magnitude higher than Spitzer [18]. It incorporates eight broad imaging filters: in addition to F560W, F770W and F1000W, there are the long-wavelength channel wide filters F1280W, F1500W, F1800W, F2100W and F2550W.

2. *Low-Resolution Slit and Slitless Spectroscopy*: MIRI offers low-resolution spectroscopy that spans a wavelength range from 5 to 12 micrometers, with increasing resolving power spanning from 40 at 5 micrometers to 160 at 10 micrometers. Slitless observations are valuable for high-precision time-series spectrophotometry of stars with transiting exoplanets, offering fast readout times for observations of bright stars.

3. *Medium-Resolution Integral Field Spectroscopy*: MIRI's medium-resolution spectrometer employs four integral field units (channels) to deliver significantly higher resolving power and spatially-resolved spectroscopy. This ranges from approximately 1330 to 3750 over the wavelength range of 4.9 to 28.5 micrometers. The integral field units split the field of view into spatial slices, producing a composite 3-dimensional data cube that combines information from each slice.

4. *Coronagraphy*: MIRI offers two types of coronagraphs for high-contrast imaging at mid-infrared wavelengths, enabling direct imaging of young and self-luminous exoplanets, as well as the study of debris disks and quasar/active galactic nuclei (AGN) host galaxies. The first type is a Lyot coronagraph, exploiting a traditional focal plane mask at 23 micrometers with a field of view of $30'' \times 30''$. The second type is estabilished by three four-quadrant phase masks at 10.65, 11.4 and 15.5 micrometers, each providing a field of view of $24'' \times 24''$. Since each phase mask has a limited range of action, more of them were equipped to offer a wavelenght wider coperture. The latter type offers the advantage of observing closer to the central source in the region where the traditional mask is opaque.

1.2.2 NIRCam

The Near Infrared Camera (NIRCam) plays a pivotal role within the JWST by offering a versatile imaging capability across near-infrared wavelengths. It encompasses two independent HgCdTe detector modules, each pointing to adjacent fields on the sky with a separation of 44 arcseconds and each one allows simultaneous exposure of short and long wavelength channels. Within each module, a dichroic mirror splits the beam into the short wavelength channel, covering a range of 0.6 to 2.3 micrometers, and into the long one, extending from 2.4 to 5.0 micrometers. Within a module, the two channels observe the same field. These two detector modules collectively cover a $2.2' \times 2.2'$ area, equivalent to 9.7 square arcminutes. The filter suite includes a total of 29 filters, divided in 10 broadband filters, 11 medium band filters and 3 narrow band filters, offering a wide range of spectral resolutions. The filters available are shown in Fig. 1.2 with their respective throughputs.

Figure 1.2: In this figure, the NIRCam and JWST optical telescope element (OTE) filter throughputs are shown.


Credits: https://jwst-docs.stsci.edu/jwst-near-infrared-camera
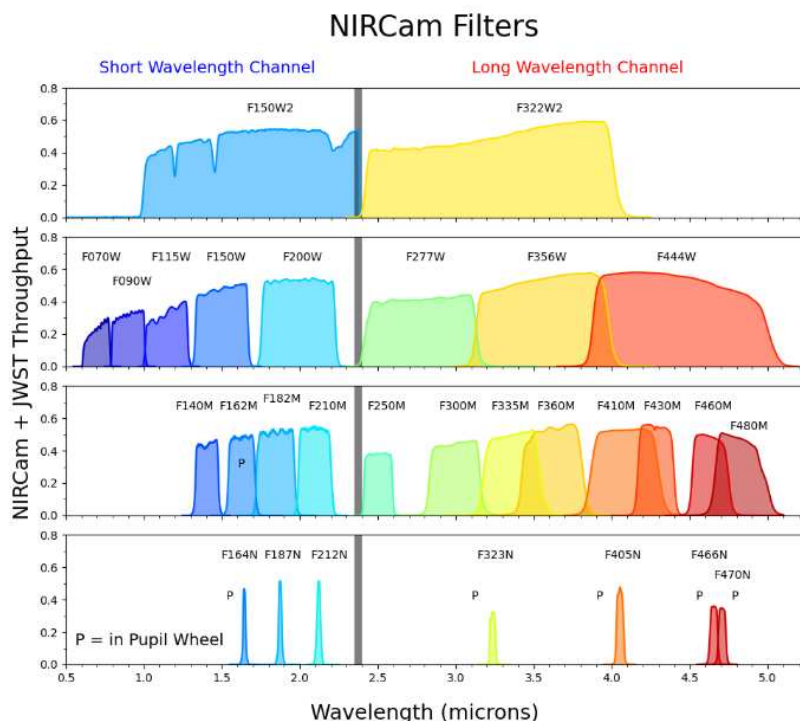
In this work, images taken at the F090W, F150W, F200W, F277W, F356W and F444W bands by this instrument are going to be used. NIRCam's imaging mode

can be used in various configurations, including full-frame, subarray and multi-field mosaic setups and its detectors feature a pixel scale of 0.032 arcseconds on the short wavelength channel and 0.064 arcseconds on the long wavelength channel. In Fig. 1.3, the images of a high redshift galaxy taken from different space telescopes are reported. It's visible how much the achievable resolution differs among the three instruments (HST, Spitzer, JWST) , being much higher in JWST case, thus highlighting its power to probe the very early Universe.

Figure 1.3: In this figure, the candidate galaxy EGS_z910_40898 is reported in the work by Finkelstein et al. [19], comparing the detections through three different space telescope: HST, Spitzer and JWST.
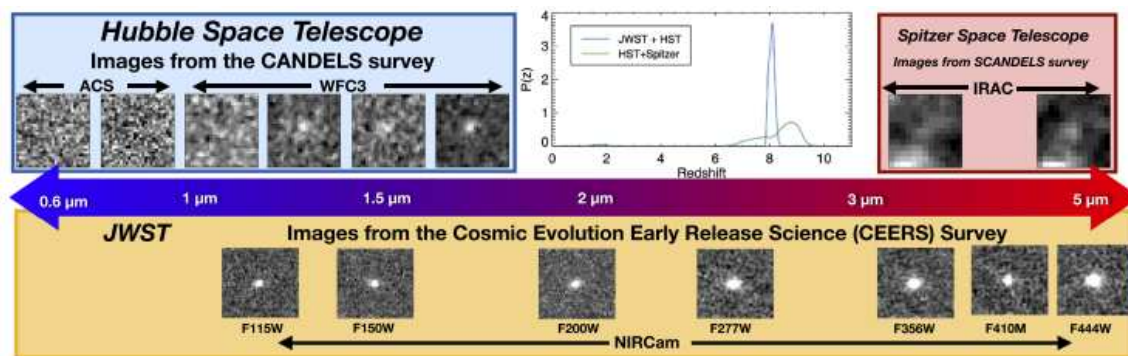
Credits: Finkelstein et al. [19]

In addition to high-resolution imaging, NIRCam extends its utility by enabling wide-field slitless grism spectroscopy on the long-wavelength channel, which allows the acquisition of spectra for every object within the field of view, with spectral resolving power decreasing from 1600 at 4 micrometers to 1130 at 2.4 micrometers. Rectangular subarrays can be also utilized for time-series grism observations of single sources, for shorter times frame.

NIRCam's coronagraphy mode is designed for high-contrast imaging, suppressing the light from bright objects to reveal fainter companions. It provides inner working angles ranging from 0.13 to 0.88 arcseconds half-width half-maximum (HWHM) and delivers a contrast of approximately 10^{-5} at 0.5 arcsecond separation and 10^{-6} at 1.5 arcsecond separation. This mode can be exploit for diverse applications, such as the discovery of exoplanets, the study of central region sources particularly bright (as galaxies which host AGN) and to get images of the environment around massive stars.

NIRCam's importance extends beyond its imaging capabilities. It serves as the

facility wavefront sensor responsible for maintaining the alignment of JWST's primary mirror, a critical requirement for ensuring high sensitivity and spatial resolution. A representation of its engineering can be appreciated in Fig. 1.4.

Figure 1.4: In this figure, the NIRCam Engineering Diagram is reported.

Credits: https://webb.nasa.gov/content/observatory/instruments/nircam.html
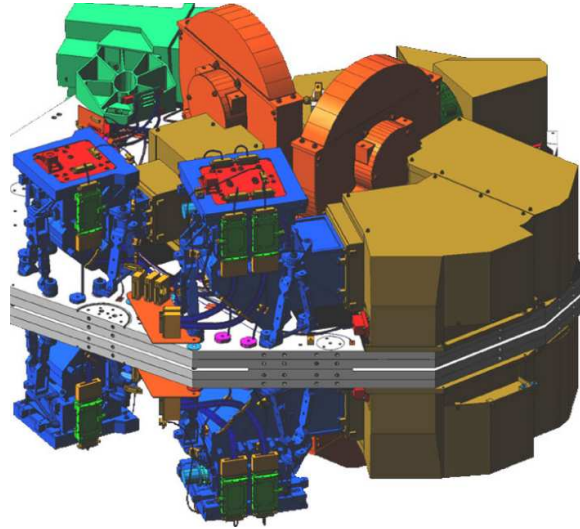
1.2.3   NIRISS

The Near Infrared Imager and Slitless Spectrograph (NIRISS) within the JWST offers a diverse range of capabilities across the near-infrared spectrum. NIRISS combines imaging, spectroscopy and interferometry functions, providing astronomers with a versatile tool to explore the cosmos.

NIRISS excels in wide-field slitless spectroscopy (WFSS), with a spectral range spanning from 0.8 to 2.2 microns and a spectral resolving power of about 150 over a field of view measuring 133" × 133". This mode enables the study of complex source scenes, allowing for the separation and analysis of spectra from different sources.

NIRISS also offers single-object slitless spectroscopy over almost the same wavelength range (0.8-2.8 μm), but with a higher spectral resolving power (R $\sim$ 700). This mode comes with two rectangular subarrays optimized for time-resolved spectroscopy of bright objects. It is particularly valuable for high-precision and spectrophotometrically stable observations, such as those focused on transiting exoplanets.

The instrument's imaging capabilities resemble those of the long-wavelength

channel of NIRCam, up to 5 μm, and can operate in parallel to enhance JWST's near-infrared survey efficiency. NIRISS boasts a $2.2' \times 2.2'$ field of view with a pixel scale of $0.065''$.

NIRISS also features aperture mask interferometry, an innovative technique that has a wide range of applications, including the detection of brown dwarfs and exoplanets orbiting around host stars up to 9 magnitudes brighter, the study of winds surrounding massive stars, measurements of nearby AGN structures and similar investigations. To properly execute this technique, a seven-aperture non-redundant mask and three medium band filters or one wide red band are involved. With this mode is possible to obtain high-contrast imaging, thanks to the effectively reducing of the JWST's aperture size into seven smaller apertures, achieved through the pupil mask. The resulting interferogram presents a central diffraction core surrounded by faint fringes, allowing for high-contrast imaging at separations of 70 to 400 milliarcseconds, particularly at wavelengths of 3.8, 4.3, and 4.8 μm.

Furthermore, NIRISS operates independently but is packaged together with Webb's Fine Guidance Sensor, making it a powerful and versatile component of the JWST's scientific instrument suite. In addition, this instrument is also able to observe in parallel mode with both NIRSpec or NIRCam.

1.2.4 NIRSpec

The Near Infrared Spectrograph (NIRSpec) on the JWST is a crucial instrument, offering comprehensive spectroscopic capabilities across the near-infrared spectrum from approximately 0.6 to 5.3 micron, created to complement the imaging capabilities of NIRCam and NIRISS. NIRSpec was meticulously designed to address the fundamental scientific goal of enabling high-resolution spectroscopic observations of the most distant galaxies observed by HST and to extend these observations to the even more remote objects identified by JWST, with the purpose of being able of precisely determine their redshifts and apply on these spectra a range of modern astrophysical diagnostic tools.

NIRSpec recognizes the need for longer exposure times in spectroscopy compared to broad-band imaging, especially for obtaining adequate signal-to-noise spectra of remote and faint galaxies. Thus, from the beginning the leading idea was that NIRSpec would be equipped with significant multi-object capability, enabling the simultaneous capture of spectra from approximately 100 objects across a field of view matching that of NIRCam.

The selection of a slit mechanism for NIRSpec was a matter of extensive debate.

Ground-based methods like customized aperture plates and fiber optics were deemed impractical for space-based applications, while an image-slicer approach was considered too large and expensive. A mechanical slit-jaw device, while more feasible, had limitations in terms of the number of movable slits it could accommodate. As a result, the choice was made to implement a novel Micro-ElectroMechanical System (MEMS) device, with the options of having either an array of tiltable micro-mirrors or an array of individually addressable microshutters. The microshutter array (MSA) was chosen as it allowed for a simpler optical design and to provide superior contrast and reduced diffraction effects and it consists of 250.000 magnetically actuated slitlets, allowing for the simultaneous targeting of multiple objects.

Even if NIRSpec was primarily designed for multi-object observations of faint, high-redshift galaxies, during the design phase efforts were made to ensure that NIRSpec could also be versatile enough to address a wide array of astrophysical topics.

With these purposes in mind, NIRSpec can perform low-resolution (R = 30-330) prism spectroscopy over the entire wavelength range and high-resolution (R = 500-1340 or R = 1320-3600) grating spectroscopy over a slightly narrower range. For both of these options, the instrument offers three primary spectroscopic modes, each one with varying spectral resolution: single slit spectroscopy, integral field spectroscopy on a field of $3.1'' \times 3.2''$ and multi-object spectroscopy over a field of view measuring $3.6' \times 3.4'$. The latter significantly enhances the efficiency of spectroscopy of distant sources and it is made possible by the microshutter array. NIRSpec has a flexible suite of dispersers and filters, providing a range of different spectral resolutions and wavelength coverage, including both prism and grating spectroscopy modes. The instrument's versatility is what makes it capable of accommodating the different scientific needs. The instrument includes seven main components: foreoptics, filter wheel, slit plane, collimator optics, grating wheel, camera optics and detector array. To maintain its operational temperature, NIRSpec is passively cooled to approximately 37 K, similar to the rest of the JWST instruments, and features trim heaters to manage temperature control. In addition, the instrument's three electronic boxes are placed on a separate warmer bench. Lastly, NIRSpec is the largest of the four instruments on JWST, with a reflective optical train and a software model for precise light path tracing.

Furthermore, NIRSpec plays a crucial role in achieving the fine-tuning of instrument pointing due to the expected limitations in JWST's absolute pointing accuracy following target field slews, employing autonomous Target Acquisition procedures to address this challenge.

1.3 James Webb first results

The launch of the JWST has indeed opened a new observational window in the Universe. It has already identified a significant number of candidates at redshifts greater than 10 in just its initial observations [20, 21, 22, 23, 24, 25]. Some of these high-redshift candidates exhibit unexpected levels of dust content. The JWST has also facilitated the statistical investigation of optically faint and optically dark galaxies, broadening our insights into galaxy populations beyond what was previously feasible with near-infrared observatories such as Spitzer [1].

Over the past decade, many studies pointed out that the the number density of galaxies at $z > 6$ sharply decreases towards higher and higher redshifts [26, 27, 28, 29], reaching even a dearth at $z > 10$ [30]. Before the launch of JWST, the prevailing consensus in the field leaned towards the notion that the epoch of cosmic reionization had effectively concluded at a redshift of around $z \approx 6.2$ [31] and must have begin around $z \approx 17.2$, as the study of the 21 cm HI absorption measurements of the Cosmic Microwave Background (CMB) suggests [32]. However, this is a controversial result and the advent of JWST has ushered in a new era of exploration, challenging these established results and adding layers of complexity to our understanding of reionization and the nature of early galaxies.

Overabundance of galaxies at $z > 10$

The role of AGN as a source of ionizing radiation has been investigated in the work of Pallottini et al. [33], although their rarity and the challenges associated with distinguishing them make it difficult to quantify their contribution to cosmic reionization. Deep near-infrared surveys have established that galaxies were the primary contributors to cosmic reionization, with radiation from AGN playing a less dominant role.

In his paper, the UV luminosity density (ρ_{UV}) is exploited as a way to measure the cosmic SFR density (SFRD), because the rest-frame UV emission from galaxies is closely related to the presence of newly formed massive stars, and its evolution with redshift is studied. JWST surveys are expected to provide more insight into this aspect, which could help reshape our understanding of the role of galaxies in cosmic reionization, depending on their luminosity.

The discovery of very bright, distant galaxies during the epoch of reionization could potentially alter our conclusions about the relative importance of bright versus faint galaxies in contributing to cosmic reionization.

The overabundance of galaxies observed at $z > 10$ by the JWST, which current models cannot explain, is also discussed and various cosmological and astrophysical scenarios have been proposed to account for this phenomenon, including modifications to the ΛCDM cosmology, feedback-free starburst scenarios and stochastic variability in the SFR (see Section 1.3.2). Each scenario presents unique challenges and implications that require further exploration and modeling to fully understand the overabundance of galaxies at such high redshifts. This overabundance is shown through a plot in the work of Finkelstein et al. [19], reported in Fig. 1.5.

Figure 1.5: This figure reports the observed surface densities in the study conducted by Finkelstein et al. [19], which result to be higher than nearly all predictions, even including all sources of uncertainty, highlighting an observed overabundance of high-redshift galaxies with respect to model predictions. This discrepancy implies that these theoretical predictions lack the full complement of physics describing star formation in the early Universe.
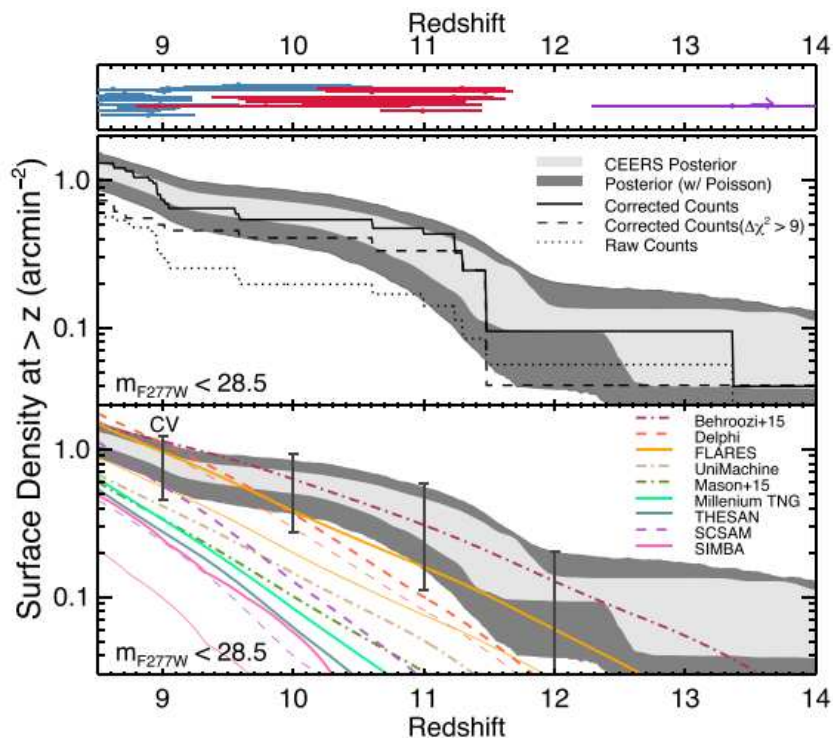
Credits: Finkelstein et al. [19]

Indeed, JWST's Early Release Observations (ERO) [34], a pivotal set of data released in 2022, have become a focal point in this evolving narrative. As we can appreciate in the work of Yan et al. [35], these observations have provided crucial in-

sights into the high-redshift Universe, particularly through the lensing cluster SMACS 0723-73 (see Section 2.1.1), a field previously observed by the HST in the Reionization Lensing Cluster Survey (RELICS) [36]. Observing this field we can appreciate the phenomenon of gravitational lensing, which occurs due to the presence of massive foreground clusters and plays a fundamental role in enhancing our ability to detect and study these early galaxies, helping us to reach otherwise too faint and too distant galaxies thanks to the effectively magnification of the light from background galaxies. The lens model developed for SMACS 0723-73, based on the Light-Traces-Mass approach, has provided essential insights into the magnification factor (μ) at different source locations, shedding light on the true nature of the observed high-redshift candidates.

These candidates, commonly referred to as dropouts since they are individuating through the dropout technique (see Section 2.1.2), are found to be well above $z \approx 11$ through the studying of their characteristic colors and their Lyman break shift. While this finding is promising, Yan and his team invite to exercise caution and consider the possibility of new types of contaminants or systematic errors, which could lead to a wrong estimation of the photometric redshift. The confirmation of these candidates as genuine high-redshift galaxies is a critical step in advancing our understanding of the early Universe.

The available data also hints at the nature of these high-redshift candidates. The SED fitting (see Section 2.4) is an invaluable tool for estimating redshift and galaxy physical properties, including stellar mass and SFR. The SED analysis executed in this paper has indicated that their median ages are approximately 34 million years, suggesting that these galaxies have only recently begun their formation processes. The median stellar masses, estimated at around $8.2 \times 10^7\,M_\odot$ for F200W dropouts and $14 \times 10^7\,M_\odot$ for F150W dropouts, align with this picture. These galaxies exhibit moderate median SFRs, ranging from 19 to $52\,M_\odot\,\mathrm{yr}^{-1}$, indicating that they have been assembling their stars at these rates over their lifetimes.

A particularly intriguing aspect of these observations is the difference in the surface densities of F150W and F200W dropouts. The former, representing a brighter population of candidates, exhibits a surface density four times that of the latter. This disparity in surface densities can not be due to any bias present in their observations, therefore if these candidates are indeed confirmed as high-redshift galaxies, it suggests that a rapid increase in the number density of galaxies over a relatively short cosmic timespan must have happened, indicatively over ~ 140 Myr from $z \approx 17.3$ to $z \approx 12.7$.

In light of these discoveries, the implications for our understanding of cosmic reionization and the early Universe are profound. The presence of a larger population

of high-redshift galaxies than previously anticipated challenges our existing models and theories (see Section 1.3.2) and could reshape our understanding of the processes that drove galaxy formation and the reionization of the universe.

However, it is essential to reiterate that many of these high-redshift candidates remain unconfirmed, and their true nature must be established through follow-up observations, ideally with JWST's spectroscopic capabilities. Only through comprehensive spectroscopic investigations we can solidify our understanding of these early galaxies and their role in the cosmic reionization epoch.

The ERO data near the galaxy cluster SMACS 0723 has been analyzed also by Adams et al. [20], leading to the remarkable discovery of a galaxy candidate at an extremely high redshift of $z \approx 16$, whose presence was also confirmed by Atek et al. [37].

A different lensing cluster (WHL0137-08), already observed by RELICS program as well, provided similar results in the discovery of high-redshift galaxy candidates. The strong lensing effect on one of these candidates allowed to reveal details of its morphology and star formation and through the SED fitting was possible to estimate the physical properties of these galaxies, including stellar masses, ages, specific star formation rates and more [38].

To summarize, the recent discoveries stemming from JWST's Early Release Observations have introduced a new level of complexity to our understanding of high-redshift galaxies and their connection to the timeline of cosmic reionization. The data suggest that the story of the early universe is far more intricate and nuanced than previously imagined, with the potential for high-redshift galaxies to be more abundant and diverse than earlier models predicted. These findings provide the groundwork for future research and exploration, which will undoubtedly continue to shape our evolving narrative of the cosmos.

JWST Cycle 1

Among the noteworthy investigations is the JADES (JWST Advanced Deep Extragalactic Survey) project, which stands out as a prime example of JWST's capabilities. Conducted during JWST's Cycle 1, JADES employed the advanced NIRCam instrument to conduct medium-band surveys at wavelengths of 2 and 4 μm and provides also NIRSpec data. This pioneering initiative unveiled the remarkable capacity of JWST to not only measure but also characterize strong emission lines up to the remarkable value of $z = 10$, being able to characterize the candidates with a precision that before was exclusive of the $z < 2$ range, opening an incredible new window in

this filed of study [39].

The JEMS (JWST Extragalactic Medium-band Survey) was also conducted during JWST's Cycle 1, using five medium-band filters at 2 and 4 μm wavelengths, employing NIRCam filters over the HUDF and coordinated parallel NIRISS images with F430M and F480M filters in the CANDELS footprint in GOODS-S (Great Observatories Origins Deep Survey-South).

These data have been proven to be capable of measuring and characterizing strong emission lines at all redshifts from $0.3 < z < 20$, constraining physical parameters in high-redshift galaxies with high efficiency [40].

JWST findings: blue monsters

A particularly intriguing revelation from JWST's observational campaigns is the discovery of enigmatic "blue monsters", as investigated in the work of Ziparo et al. [41]. These are a unique class of galaxies at super-early epochs, characterized by their strikingly blue spectra (with a spectral index $\beta \sim -2.6$) and minimal dust attenuation ($A_V \sim 0.02$). This seemingly paradoxical combination of intense blue colors and negligible dust obscuration has posed an intriguing challenge to astrophysicists.

Two primary scenarios have been proposed by these authors to explain the peculiar properties of these "blue monsters." The first scenario suggests that super-early galaxies maintain low levels of dust attenuation due to the ejection of a significant fraction of their dust content. This ejection of dust is primarily driven by the intense radiation pressure exerted by the galaxy's newly born, massive stars. This intriguing hypothesis highlights the importance of the galaxy being in a starburst phase, associated with high dust ejection rates. Moreover, the results align with the observations indicating the absence of [O III] 88-μm lines, which could be attributed to the high escape fraction of ionizing photons.

An alternative scenario involves the spatial segregation of dust within these super-early galaxies. In this scenario, dust, primarily residing within opaque Giant Molecular Clouds (GMCs), is physically separated from the transparent regions that emit in the ultraviolet. This spatial segregation of dust not only accounts for the blue spectra observed in these galaxies but also predicts the existence of far-infrared (FIR) dust continuum emission. Crucially, this continuum emission can be detected by ALMA (Atacama Large Millimeter/submillimeter Array), providing a potential confirmation of this phenomenon. The non detection of this emission found by Poppidan et al. [34] favours the ejection scenario, which predicts a value of FIR continuum emission not detectable.

An important result comes from Bouwens et al. [42], who provided new estimates of the UV luminosity function (LF) at different redshifts: $z \approx 8 - 9$, $z \approx 10 - 11$ and $z \approx 12 - 13$. The LF estimates at $z \approx 12 - 13$ were higher than recent determinations using JWST data, with the caveat that these results had large uncertainties due to being based on only two identified sources within a small volume. The results suggested that the UV luminosity and SFRD may experience a milder evolution than expected by many theoretical models, exceeding the predictions of constant star formation efficiency models. This departure from theoretical predictions implied that star formation in the earliest galaxies might be substantially more efficient, showing significant variations in the main-sequence evolution, or the mass-to-light ratio of stars might be significantly lower, possibly indicating a modified initial mass function (IMF).

The standard model continues to be questioned by the presence of extremely high-redshift galaxies, such as the one found by Donnan et al. [24] at $z \approx 16.4$ in the COSMOS field. The sample here analyzed was exploited to derive the UV LF and the evolution of the ρ_{UV} and consequentially the estimate of the declining cosmic SFRD, finding that the high-redshift LF evolves into a form best described by a double power-law function, as opposed to a Schechter function, at least up to $z \approx 10$.

A discovery of exceptionally luminous candidate galaxies at redshifts greater than 10 is also reported in the work of Casey et al. [43], using data from the COSMOS-Web Survey. The high stellar mass and baryon fractions observed in these galaxies suggest that they have experienced rapid and burst-driven star formation, which outpaces the growth of their underlying dark matter halos. This may be attributed to episodes of star formation that are much faster than those expected in the typical star-forming history of galaxies. The rapid growth of these galaxies, driven by stochastic bursts of star formation, may contribute to the observed change in the shape of the UV LF from a double power law at $z \approx 8$ to a Schechter function. The discovery of these luminous galaxies challenges earlier expectations and theories, therefore the authors explore the possibility that alternative cosmological models could account for the high number of massive halos at early times, such as Early Dark Energy (EDE) models.

Overabundance of bright galaxies in the same field is also found in the work of Franco et al. [44], with a detection almost twice the expected number of galaxies at $z \geq 9$ in the volume of this survey.

Even in the GLASS field (observed during the GLASS-JWST Early Release Science Program [45]) similar results were obtained by Castellano et al. [21], with the detection of two bright sources with magnitudes around $M_{UV} \approx -21$ placed at redshifts $z = 10.6$ and $z \approx 12.2$, which presence suggests a non evolving LF,

challenging again the previous beliefs based on LF extrapolations at lower redshifts. Nevertheless, the authors remember that these results are subjectes to the cosmic variance due to the limited area and to the possible presence of a foreground cluster that may increase the candidates luminosity.

Belonging to the CEERS field there's another candidate presented by Naidu et al. [23]. This galaxy presents two possible redshift solutions: around $z \approx 17$ and $z \approx 5$. If the galaxy is indeed at $z \approx 17$, its physical properties and morphology are consistent with galaxies at redshifts greater than 10. However, its unexpectedly high stellar mass and UV luminosity for its cosmic age make it a remarkable and challenging discovery. The authors provide possible explanations, such as a quiescent galaxy with ionized gas or a dusty starburst.

On the other hand, if the galaxy is at $z \approx 5$, this could have important implications for our understanding of galaxy evolution and the presence of a lower-redshift population in high-redshift candidate samples.

JWST findings: evolution of the SFRD

Indeed, spectroscopic confirmation is crucial for obtaining robust results on the UV luminosity functions and cosmic SFRDs. The results of the study of Harikane et al. [25] suggests that there is a mild redshift evolution in the UV LFs and cosmic SFRDs from approximately $z = 9$ to 12, confirming previously discussed results and the tension with theoretical models prediction of a rapid decline in cosmic SFRD beyond $z = 10$. The authors suggest that this result could be explained by a higher star formation efficiency in galaxies at these redshifts, shown to be approximately 5% or higher at $z \approx 12$ than the one inferred at lower redshifts.

Another explanation considered was the presence of AGN activity, which despite the fact that the quasar luminosity functions declined rapidly at higher redshifts is plausible, given that some faint AGNs in galaxy samples at $z > 4$ were reported. In fact, one of the candidates found by Yan et al. [46] was confirmed to be an AGN [47]. An additional possibility explored in this work is a top-heavy IMF at high redshifts. In the early Universe, the IMF might favor the formation of more massive stars, affecting the UV-to-SFR conversion factor.

Cosmic variance could also affect the observed SFRDs, especially considering the relatively small survey volume, but the results indicated that the SFRD at $z \approx 12$ was higher than model predictions even beyond the uncertainty associated with cosmic variance.

In the conclusion of their work, the authors underline that the accurate identifying of low-redshift interlopers that might mimic high-redshift galaxies is essential in order to obtain reliable results.

JWST findings: an abundant population of AGN at $z > 8$

A really interesting discovery is the presence, reported in the paper by Larson et al. [48], of an accreting supermassive black hole (SMBH) at a redshift of $z \approx 8.7$ using spectroscopy and imaging data from JWST's CEERS Survey. The galaxy hosting this SMBH was initially identified as a photometric Lyα-break dropout candidate and its true nature was revealed through the spectroscopic detection of significant broad Hβ emission lines, indicative of AGN activity. The finding of a SMBH at such an early cosmic epoch was not expected, therefore the authors address the challenges of explaining its presence.

The detection of AGN at such high redshift is not isolated, since a similar outcome has been found by Scholtz et al. [49]: an extremely luminous galaxy hosting an AGN is found at a redshift of $z \approx 10.6$ through the measurements of extended Lyα emission, whose halo's radial surface brightness is more consistent with quasars than star-forming galaxies.

The region studied in this work is considered a strong candidate for a protocluster core, with a dark matter halo mass consistent with a Coma-like cluster progenitor at $z \approx 10.6$.

In summary, JWST's transformative findings regarding super-early galaxies have profound implications for our understanding of galaxy formation and evolution in the early Universe. These discoveries underscore the complexity and diversity of the high-redshift Universe and emphasize the importance of multi-wavelength observations in decoding the enigmatic nature of these distant celestial objects. JWST's ongoing mission promises to unveil even more secrets and further enrich our understanding of the cosmos, paving the way for future breakthroughs in the field of observational astronomy. The observations and analyses conducted thus far represent only the beginning of a new and exciting chapter in the quest to understand our Universe.

1.3.1 Role of dust

Dust is a fundamental component of galaxies, exerting a profound influence on their observed SED and derived physical properties. It presents a challenge to our understanding of galaxy evolution, impacting the estimation of many physical properties

derived using UV/optical rest-frame data and introducing uncertainties, particularly at higher redshifts. This is due to the fact that rest-frame UV data have long been crucial for studying high-redshift galaxies, however, these measurements are highly susceptible to dust attenuation. Previous satellites, such as Spitzer and Herschel, were able to properly quantify the role of the dust, but only more recently, thanks to JWST, it's starting to be possible to delve deeper, at higher redshift and with better spatial resolution.

One perplexing aspect is the uncertainty surrounding the cosmic SFRD, especially beyond redshift $z > 3$ [50]. Studies based on UV data at these redshifts have reported a pronounced drop in SFRD at $z > 2$ [27, 30], while observations in the FIR and radio wavelengths have shown a less dramatic decline in SFRD, or in some cases, a plateau, at z > 2 [51]. This inconsistency is a central theme in recent extragalactic astrophysics research.

The integration of JWST data with submillimeter and millimeter observations has the potential to further enrich our understanding of galaxies in the high-redshift Universe, helping to better understand the effect of the dust in their analysis. This synergy between JWST and these complementary observatories allows for the identification and characterization of various galaxy populations, such as dusty star-forming galaxies (DSFGs) at $z \gtrsim 5$ and Lyman break galaxies (LBGs) at redshift above 10. The former category is particularly important to recognize, due to its peculiar color properties when observed through JWST/NIRCam filters: they mimic the Lyman break at higher redshift, presenting a drop out in the bluest filters while being well detected in the redder filters, making more difficult the identification of real ultra-high redshift LBGs. This intriguing behavior highlights the limitations of relying solely on dropout selection techniques for the identification of high-redshift galaxies, creating the necessity to be able to distinguish lower redshift contaminants in samples of candidate $z > 10$ Lyman break galaxies, emphasizing the complexity of identifying such high-redshift systems [52].

Candidate dusty dwarfs

An interesting aspect of dust in star-forming galaxies is its positive correlation with stellar mass [53]. This correlation has been observed in numerous studies, with more massive galaxies generally exhibiting higher dust attenuation. In contrast, galaxies with stellar masses below $10^{8.5}$ solar masses experience less dust attenuation. This is unsurprising since intense star-forming activity generally corresponds to a large dust content, considering that dust is produced by stellar processes like pulsating moderate-mass stars and supernovae.

The pursuit of dusty low-mass galaxies necessitates deep infrared observations. However, this is problematic with observatories like HST and Spitzer, as these galaxies appear extremely faint in the optical rest-frame due to the combination of low stellar mass and high dust extinction. What is more, the correlation between stellar mass and dust extinction appears to remain consistent only up to redshift $z \sim 3$, with the possibility of decreasing correlations at higher redshifts.

Exploiting `Bagpipes` (see Section 3.4.1), the study of Bisigello et al. [54] conducted on early photometric observations from CEERS revealed that 81% of the galaxies forming the F200W-dropout sample had redshifts below 2. The CEERS field covers a substantial area, enabling the selection of rare sources and increasing the statistics of prior surveys. The F200W-dropout galaxies displayed a median stellar mass of $10^{7.3}$ M_* and a median dust extinction of 4.9 magnitudes. The entire F200W-dropout sample exhibited A_V values greater than 0.9, indicating a significant dust content.

Despite the potential for dust attenuation, the SFR of these galaxies was relatively low, with a median of $0.01 M_\odot yr^{-1}$. These low SFR values resulted in total IR luminosities (8-1000 μm) of around 10^7 solar luminosities, whose low value is the reason why such galaxy populations remained largely unexplored even with FIR observatories.

A detailed examination of the SFR-stellar mass plane, which are reported in Fig. 1.6, revealed that a fraction of these galaxies could be classified as starburst galaxies. These starbursts, defined as galaxies significantly above the main sequence of star formation, constituted 26% of the F200W-dropout sample at $z \leq 1$ and 27% at $1 < z \leq 2$, which is consistent with the percentages for galaxies found at similar redshift, but not dusty. These findings imply that while dust attenuation may affect the SFR estimates, the high dust content of these galaxies does not necessarily stem from a starburst episode.

Figure 1.6: These plots report the SFR-stellar mass planes, moving from $z = 0$ up to $z = 7$, of the F200W-dropout sample (coloured points) compared with the complete CEERS sample (black dots).
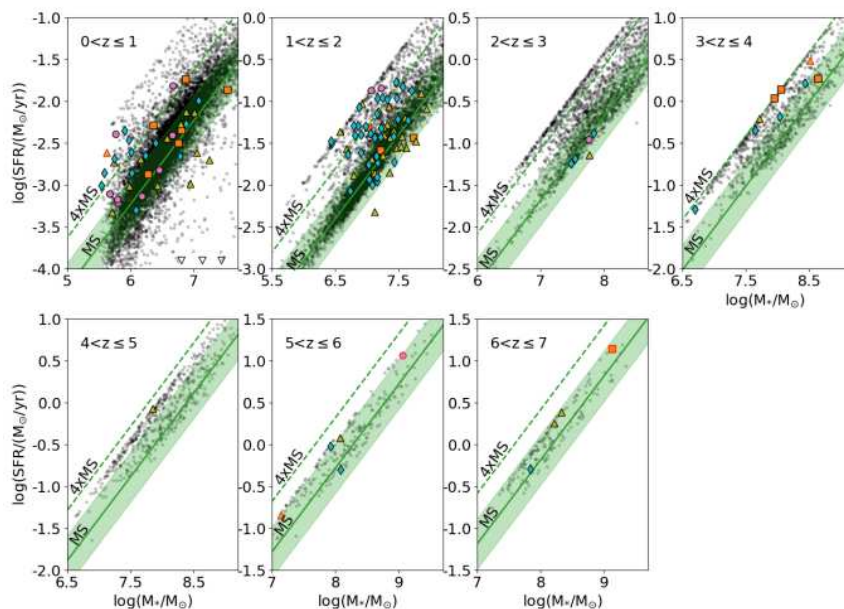
Credits: Bisigello et al. [54]

Nevertheless, several caveats should be acknowledged. The estimated SFR is based on the SED analysis of rest-frame UV-to-optical or optical-to-near-IR data, depending on the redshift. In the absence of FIR observations, these SFR estimates may be underestimated, particularly for the most dusty objects. In addition, intrinsic correlations exist between SFR and stellar mass, given that both are derived from the SED fitting. The assumed delayed star formation history and the minimum allowed age of 1 million years limit the specific star formation rate (sSFR) to values below $10^{-7.9}$ per year, a value in agreement with other works.

The galaxy's physical properties are based on a limited number of photometric points with relatively high signal-to-noise ratios, therefore meaning that the photometric redshift retrieved could be not right. Among the F200W-dropout sample, only five objects (4% of the sample) exhibited SFR values at least four times lower than the main sequence, indicating exceptionally low SFR. These objects, when considered with aperture photometry, align well with SED templates for star-forming galaxies, suggesting that an alternative, non-passive solution is plausible.

Remarkably, the F200W-dropout sample, in general, displayed a very high level of dust extinction. This is even more striking when compared to galaxies of similar

stellar mass within the CEERS dataset. Whereas the F200W-dropouts had a median A_V of 4.7, all the galaxies in CEERS had a median A_V of 0.48. Median A_V values across various stellar mass bins in the CEERS sample correlated with average relations between dust extinction and stellar mass, confirming that the elevated dust extinction in the F200W-dropout sample was not solely an artifact of the adopted SED fitting procedure.

The emergence of this exceptional population of extremely dusty dwarf galaxies, representing 0.5% of galaxies with stellar masses ranging from $10^{5.8}$ to $10^{7.2}$ solar masses at $z < 1$ and 0.8% of galaxies with stellar masses from $10^{6.8}$ to $10^{8.2}$ solar masses at $z = 1 - 2$, underscores their rarity and non-representative nature of the general dwarf galaxy population at these redshifts.

It's noteworthy that the observational area covered in these studies is four times larger than previous observations in SMACS 0723. Despite this expanded scope, no galaxies associated with redshifts greater than 10 were identified. However, a number of objects in the sample exhibited a probability greater than 10% of being at these extreme redshifts. By integrating the probability distribution at redshifts greater than 10 for each of these objects, it's statistically expected that the sample includes 17 galaxies at redshifts greater than 10. These galaxies, however, require spectroscopic follow-up for confirmation.

Conversely, the SED-fitting analysis did not identify any galaxy candidates at redshifts greater than 9. The rarity of dusty high-redshift sources in this sample contrasts with findings in other fields (see Section 2.1.2).

The enigmatic nature of dust and star formation rates continues to be a focal point of study. While these findings provide valuable insights, numerous questions remain unanswered. Future spectroscopic observations and data at longer wavelengths will be instrumental in further unraveling the mysteries surrounding galaxies with remarkable dust content and their implications for our understanding of the Universe.

Meanwhile, until these follow ups are not available, this work aims to provide an answer regarding how much the photometry of these objects can influence the precision of their physical properties estimations and trying to quantify the relevance of the SED fitting tool choice in the final results.

1.3.2 Tension with ΛCDM model

In the preceding section, a variety of results derived through the first year of JWST observations have been presented, all of which point to a lack of agreement with the

model expectations. To gain a deeper understanding of this discrepancy, the theoretical framework that leads to these unfulfilled predictions is briefly overviewed, from the formalism behind them to the cosmological model to which this work referred.

Press-Schechter formalism

The Press-Schechter (PS) formalism stands as a fundamental concept in cosmology, offering a structured framework for estimating the mass distribution of collapsed dark matter clumps. These clumps serve as the foundational structures for galaxy formation, galaxy groups and galaxy clusters, making the study of their properties a vital component of understanding the large-scale structure of the Universe.

Modeling the mass function of these clumps poses a significant challenge because the process of non-linear gravitational collapse remains elusive from a theoretical perspective. To address this challenge, researchers have employed approximations to estimate this critical function [55].

Early efforts at approximating the mass function were made by researchers such as Doroshkevich (1967). However, the most substantial advancement in this field came with the introduction of the Press-Schechter (PS) formalism in 1974 [56], which has since become a cornerstone of cosmological research.

The PS formalism outlines a structured methodology for estimating the mass function [57]:

- *Smoothing.* To begin, the initial density field is smoothed on a specific scale, denoted as R, in which the variance of the field is represented as $\Lambda \equiv \sigma^2(R)$. Smoothing is essential as it prevents the onset of non-linear behavior at very small scales.

- *Linear Evolution.* The formalism involves tracing the linear evolution of the density field. During this process, the density at each point in space is rescaled using a time-dependent function known as the linear growing mode, represented by $b(t)$.

- *Threshold for Non-Linearity.* Clumps or regions in the density field are identified as non-linear when the linearly evolved density surpasses a specific threshold, denoted as δ_c (approximately equal to 1). This threshold signifies the point of gravitational collapse.

- *Fraction of Collapsed Mass.* The PS formalism calculates the fraction of mass that has undergone gravitational collapse, denoted as Ω ($< \Lambda$). This calcula-

tion is based on the probability that the linearly evolved density surpasses the threshold δ_c.

- *Determining the Mass Function.* The mass function $n(M)$ is derived based on the fraction of mass that has undergone gravitational collapse and the typical mass that forms within a region of size R, in accordance with a "golden rule."

The PS formalism has demonstrated remarkable success, particularly when compared with extensive N-body simulations. These comparisons have validated the PS formula as a reliable approximation, especially for masses equal to or larger than the characteristic mass (M_*) forming at a given redshift [58].

The threshold parameter δ_c within the PS formula aligns closely with the value predicted by the spherical collapse model, approximately 1.69. However, as the Universe evolves, this threshold tends to decrease, reaching values around 1.5 at later cosmic epochs.

The "fudge factor" of 2 in the PS formalism, initially subject to debate, was ultimately elucidated [59]. This factor accounts for the inclusion of smaller structures in larger collapsing ones, even if their density does not surpass the threshold, playing the role of normalizing the mass function. The precise alignment of the factor of 2 in the PS formula occurs when the linear density field is smoothed using a sharp filter in k-space.

In conclusion, the PS formalism plays a pivotal role in cosmology, offering a reliable and valuable method for estimating the mass function of dark matter clumps. Despite its theoretical simplifications and initial controversies, it stands as an effective tool for comprehending the large-scale structure of the Universe and making predictions concerning the formation and characteristics of cosmic structures, ranging from galaxies to galaxy clusters. Furthermore, variants from the standard PS formalism are provided: these include the Sheth & Tormen one [60] and the Extended PS [61].

The ΛCDM model

The ΛCDM (Lambda Cold Dark Matter) model is the prevailing and widely accepted standard cosmological model for describing the large-scale structure and evolution of the Universe. It provides a comprehensive framework that incorporates various key components to explain the observed properties of the cosmos. It consists of two primary components:

1. Λ (Lambda). This term represents the cosmological constant, which was intro-

duced by Albert Einstein into his theory of General Relativity. The cosmological constant is associated with dark energy, a mysterious and repulsive force that is responsible for the observed accelerated expansion of the Universe. In the ΛCDM model, Λ serves as the energy density associated with dark energy, counteracting the attractive force of gravity.

2. CDM (Cold Dark Matter). Dark matter is a form of matter that does not emit, absorb, or interact with electromagnetic radiation (light). It exerts gravitational influence, holding galaxies and galaxy clusters together. The term "cold" refers to the fact that dark matter particles are non-relativistic, meaning they move at speeds significantly less than the speed of light. This characteristic is essential for the growth of cosmic structures, given that this slowness in their motion is what allows them to clump together and form structures over cosmic time scales. In the ΛCDM model, dark matter is a dominant component, accounting for a significant portion ($\sim 80\%$) of the total mass in the Universe.

In summary, the ΛCDM model is built on the foundation of General Relativity and combines the effects of dark energy (Λ) and cold dark matter (CDM) to explain the expansion, large-scale structure and evolution of the Universe. It provides an accurate description of the observed universe, accounting for phenomena like the cosmic microwave background radiation, the large-scale distribution of galaxies, and the accelerated expansion of the cosmos. This model has become the standard framework for cosmologists and its predictions align well with various cosmological observations and experiments [62].

The ΛCDM cosmological model, despite its overall success in explaining the large-scale structure of the Universe, is facing intriguing challenges emerged with the possibility of studying increasingly younger galaxies, started with the HST and going on with the latest observations from the JWST. As previously mentioned, these challenges arise from the discovery of primordial galaxies at high redshifts, which exhibit characteristics that appear to be at odds with the predictions of the model.

The comparison between IR and rest-frame UV and optical observations has highlighted the existence of sources that were previously overlooked, even by the deepest HST surveys. The presence of such sources underscores the limitations of previous observations and their potential biases in our understanding of stellar mass assembly in the Universe.

Recent studies, such as the ones reported in Section 1.3 [24, 42, 25], have revealed a surprisingly high mass function for these early galaxies when compared to the ΛCDM framework. While the model has successfully described the formation and

distribution of structures on large scales, the abundance of such massive early galaxies seems to be in tension with its predictions. Additionally, the star formation rates in these galaxies appear to be exceptionally high, further raising questions about whether the ΛCDM model can fully account for these findings.

However, it is important to note that the tension between the observations and the model is not yet conclusive. Several factors may contribute to these discrepancies, including uncertainties in redshift estimations and stellar mass measurements. Errors in redshift estimations, especially for candidates selected using photometric data, can significantly impact our understanding of these high-redshift galaxies. In addition to that, other factors that need to be considered include a more efficient star formation at high redshift, a different IMF and the possibility that some of these galaxies are AGN.

These tensions between the observed data from JWST and the ΛCDM model underscore the need for further studies and confirmations. It is clear that this area of research is still in its early stages and additional investigations are essential to provide a definitive answer. The recent discovery of primordial galaxies with JWST is a significant step in our understanding of the Universe's early epochs, and more observations and analyses are required to resolve the discrepancies and refine our cosmological models.

Without claiming to cover the topic exhaustively, which would be impossible in just few pages, in the next section some studies which instead claim that there is no reason to discard the standard model, suggesting possible explanations to explain the observed data, are presented.

UV slopes evolution

Through measuring the rest-frame UV continuum slopes (β) of galaxies in the redshift range $8 < z < 16$ using a combination of JWST ERO and ERS NIRCam imaging and ground-based near-infrared imaging, Cullen et al. [63] investigated whether there is any evidence for an evolution in the typical UV colors of galaxies at these redshifts.

The results indicated that even the faintest galaxies uncovered by JWST at $z \approx 8 - 16$ had UV colors no bluer than the bluest galaxies in the local Universe. They also found evidence for a $\beta - M_{UV}$ relation, in which brighter UV galaxies tend to have somewhat redder UV slopes. However, compared to galaxies at $z \approx 5$, the galaxies in this sample were bluer.

These findings suggest that galaxies at high redshift ($z > 8$) are generally bluer,

although there is not substantial evidence for a large fraction of ultra-blue galaxies. The galaxies in the sample appeared consistent with young, metal-poor and moderately dust-reddened galaxies predicted by theoretical galaxy formation models at these redshifts, therefore not observing observations in contrast with the predictions by the actual standard model.

Feedback-Free starbursts

Another possible explanation that can resolve the tension between the recently JWST discoveries and the ΛCDM model regards the concept of "Feedback-Free starBursts" (FFBs) in galaxies at redshifts $z \sim 10$ and above introduced by Dekel et al. [64]. The key factor in achieving high-efficiency conversion of accreted gas to stars in the brightest galaxies is the characteristic density of $\approx 3 \times 10^3 cm^{-3}$ in star-forming clouds, leading to a free-fall time of ~ 1 Myr, which is shorter than the delay between a starburst and the onset of effective stellar winds and supernova feedback.

These FFBs are expected to occur at relatively low metallicities. At these redshifts, the low metallicities and high-density conditions result in shorter cooling times down to star formation temperatures. This density threshold for efficient star formation is achieved in the cold-flow regime, where atomic cooling times are much shorter than the halo free-fall time. Additionally, high surface density is required, in order to make radiative feedback ineffective in suppressing star formation.

In conclusion, Dekel and his team present a theoretical framework proposing a model based on specific conditions and processes that can lead to this high-efficiency star formation. This model predicts that galaxies with FFBs are expected to have relatively high stellar densities with relatively low dust attenuation and a morphology of a thick compact disk with giant clumps if the galaxies are massive, otherwise lower mass galaxies could have smoother or non-disc-like structures.

The study suggests potential implications for the survival of FFB clusters as globular clusters in today's brightest cluster galaxies and the efficient formation of massive black holes. It also raises questions about the potential effect on the cosmological reionization process.

It is important to note that these are theoretical predictions, and further validation and quantification are required through simulations. The proposed novel concept of FFB phenomenon has the potential to shed light on the processes governing star formation in the early Universe.

Expulsion of dust during the earliest phases of galaxy formation

Another work pointing that there can be an explanation for the apparent discrepancies found is the one by Ferrara et al. [65], in which they present a minimal galaxy evolution model including dark matter Halo Mass Function (HMF), supernova feedback and dust attenuation calibrated on ALMA REBELS results to predict the galaxy luminosity function at redshift $z = 7$. They found a correlation between UV luminosity and SFR: the effective optical depth (τ_{eff}) is found to be proportional to the SFR raised to the power of 1.45, suggesting that galaxies brighter than a certain magnitude at $z = 7$ likely have a significant contribution from AGN. The study predicts that luminous infrared galaxies (LIRG) contribute less than 1% of the cosmic SFR density at $z \approx 7$. In addition, the model predicts negligible dust attenuation at redshifts around 11.5 and 13.75, which is supported by the very blue UV slopes (β) of the highest redshift candidates identified by JWST studies, and suggests that dust may have been efficiently expelled during the earliest phases of galaxy formation at high redshifts.

The study indicates that the luminosity function at $z = 7$ is evolving and it provides predictions for the abundance of bright JWST candidates at different redshifts, resulting in values not inconsistent with the ΛCDM paradigm.

A top-heavy IMF

Ferrara et al. [65] explore also the possibility that an explanation for the observed UV luminosity excess could be the presence of a top-heavy IMF due to very low metallicities in early galaxies.

This explanation is also cited by Finkelstein et al. [19], who exploiting the CEERS program, analyzed the properties of a sample including 26 robust candidate galaxies at $z > 8.5$, discovering an observed abundance of modestly bright galaxies in significant excess from predictions. From this sample they estimated the $z \approx 11$ rest-UV luminosity function, finding that the observed UV luminosities appear to be enhanced by approximately 1.8 to 2.5 times.

They suggest that a plausible physical explanation could be a top-heavy IMF due to the presence of very low metallicities. The paper discusses potential explanations, including changes in dust attenuation, star formation laws, galactic feedback and numerical simulation resolution, that could reconcile the observations with model predictions, showing that their results are not incompatible with the standard model.

Deriving the stellar masses of their sample and comparing them to the maximum

expected mass according to ΛCDM, also the work by Franco et al. [44] finds no tension between observations and theory. These data belong to the COSMOS-Web survey.

The gravitational lensing was exploited by Hsiao et al. [66] with the observations of the lensed galaxy MACS0647–JD. These observations cover a wide range of NIRCam filters, providing insights into the spectral properties of this galaxy at redshift 10.6. MACS0647–JD is lensed and observed in three components. Hsiao and his team delensed the galaxy to determine its intrinsic properties, finding that this galaxy is quite blue in its spectral characteristics, indicating a star-forming region relatively free from dust, as well as a more massive component. A possible merging or interaction of two clumps within this galaxy is studied, finding large SFRs, though not exceeding theoretical limits.

Mason et al.[67] retrieved a theoretical upper limit on the UV LF for galaxies at redshifts around 10, assuming maximum star formation efficiency and young ages (10 million years), which is fully consistent with the recent observations detecting an excess of bright galaxies compared to theoretical models. Therefore, the authors declare that there is no formal tension between current observations at redshifts greater than 10 and the formation of galaxies within the context of CDM halos.

Dust attenuation plays a significant role in shaping the Schechter function of the UV LF model at redshifts around 10. If dust attenuation is minimal in galaxies during their first few hundred million years, this could explain observations that indicate a power-law LF at redshifts around 8. Indeed, understanding dust attenuation at redshifts greater than 8 is essential for interpreting high-redshift observations.

The study finds that most currently observable galaxies are exceptionally bright because they are young and rapidly assembling. This suggests that galaxies observed at redshifts around 10 are likely the most extreme examples in terms of star formation and they may not be representative of the overall galaxy population.

Ultimately, the paper predicts that in JWST Cycle 1, deeper surveys reaching even fainter magnitudes will detect older galaxies (around 100 million years old) that are more typical of the population at fixed mass. The initial JWST observations of galaxies at redshifts around 10 will be dominated by very young galaxies with extremely high star formation rates.

In another paper by Muñoz et al.[68], the focus is on breaking the degeneracies in galaxy-formation models at redshifts greater than 10. The paper highlights that the first JWST-derived UV LFs at redshifts greater than 10 show more UV-bright galaxies than predicted by current models and emphasizes that galaxy-clustering measurements are crucial for resolving these discrepancies. Clustering measurements can

provide a more robust check than studying the bright end of the UVLF alone, which is susceptible to systematic effects such as AGN contamination and dust.

The study employs a semi-analytic model calibrated to HST UV LFs at redshifts less than or equal to 10 and shows that the level of stochasticity and the star-formation efficiency are highly degenerate at each redshift. However, clustering measurements tentatively suggest a tight connection between halos and galaxies at redshifts around 4 to 6 with low stochasticity. The authors extend this analysis to the first JWST UV LFs, demonstrating that while both increased stochasticity and higher mean UV emission can fit them. The biases can help distinguish between the two galaxy formation scenarios, since the large stochasticity one predicts consistently lower biases.

Lastly, the results from other simulations (FIRE-2 simulations) that aim to reproduce the observed abundance of UV-bright galaxies at redshifts greater than 10 are discussed by Sun et al. [69]. The simulations, incorporating bursty star formation histories, successfully reproduce the observed population of UV-bright galaxies at high redshifts without the need for additional factors like enhanced star formation efficiency, top-heavy IMFs, AGN contributions or Population III stars and show that the galaxy-scale star formation efficiency does not significantly change over the redshift range of 5 to 12. The study indicates that the bursty star formation history commonly predicted for galaxies during cosmic dawn is essential for explaining the bright end of the UV LF at redshifts greater than 10. The results from these simulations have implications for the understanding of bursty star formation, selection effects in rest-UV-selected samples and the use of high-redshift galaxies as cosmological probes.

In conclusion, the question is still open and at the moment no conclusive results were found, neither to discard the ΛCDM model nor to completely resolve all the issues. As already said throughout this work, spectroscopic confirmations are indeed essential to step forward in understanding the physics behind such high-redshift galaxies and consequently all the repercussions on our understanding regarding the history of the Universe.

Meanwhile, given the novelty of JWST observations, assessing the impact of different photometric extractions on the physical properties of these high redhsift galaxies, which is the aim of this thesis, is a crucial step to investigate a possible tension with cosmological models, while waiting for the spectroscopic follow ups.

1.4 This thesis

In this context, with all the new findings by JWST that can potentially revolutionize what is actually acknowledged up to now, it is fundamental to understand whether these results are robust or if, instead, the photometric accuracy is not enough to draw definitive conclusions regarding the physics behind the evolution of galaxies into what we observe in our local Universe.

At this aim, it is pivotal to asses the impact of both the choices regarding the tools exploited during the photometric analyses and the reduction applied on the original images on the retrieval of their physical properties.

Therefore, a systematic investigation carried out on the estimations obtained through different reductions and employing different softwares is the main scientific result of this thesis. In particular, this work quantifies the impact of the software tools adopted to derive the photometry of high-redshift galaxies in multi-wavelength imaging from JWST and their effects on the SED fitting analysis to retrieve the physical parameters of these galaxies (such as redshift, stellar mass, SFR and dust extinction).

Chapter 2

Methods

As reported in Chapter 1, spectroscopic confirmations are currently needed in order to drive real conclusions on the properties of all the candidates identified through photometric means and consequently to finally reach robust understanding of the physics regarding the reionization of the Universe and the stellar-mass assembly of galaxies.

Nowadays, however, these spectroscopic analyses have still to wait, due to the high request for JWST observational time and therefore the difficulty to have proposals approved, and additionally for the expensiveness of carrying out this kind of inquiries.

In this context, it is helpful to conduct an accurate systematic investigation, with the purpose of trying to shed light on the reliability of the estimations and the results obtained up to date.

In this section, the different photometric techniques adopted in this work to derive the multi wavelength photometry of the sample previously individuated by Rodighiero and her team [1] will be described in detail, along with the SED fitting code employed for the retrieval of their physical parameters.

2.1 Sample selection

2.1.1 SMACS 0723-73

The globally publication on July 13 of the James Webb Space Telescope Early Release Observations (ERO) data marked a significant milestone in the field of astronomy.

These ERO data are the first set of science-grade observations from JWST, which is poised to usher in a new era in our understanding of the cosmos. Notably, JWST has extended our reach into the early Universe, going beyond the redshift limit of $z \sim 11$ imposed by HST thanks to its NIRCam instrument's capability extending to ~ 5 μm, covering a total of six broad bands. Among the targets selected for JWST ERO observations is the massive galaxy cluster SMACS 0723-73, a well-known "cosmic telescope" due to its gravitational lensing properties [35]. The image of this galaxy cluster (RA: 7:23:8.56; DEC: -73° 26' 59.18") has been known as Webb's First Deep Field and its visible in Fig. 2.1.

Figure 2.1: The SMACS 0723 field captured by JWST NIRCam instrument.

Credits: https://esawebb.org/images/webb-first-deep-field/

The concept of gravitational lensing, effectively creating natural telescopes from massive galaxy clusters, has been an invaluable tool for discovering and studying the most distant galaxies. Over the last twenty years, these space laboratories have allowed us to first reach galaxies at z $\sim$ 4.92 [70], to ten years later be able to move onto z $\sim$ 7.5 [71]. More recently cluster-lensing surveys, including the Cluster Lensing and Supernovae Survey with Hubble (CLASH) [72] and the Hubble Frontier Fields (HFF) [73], have permit to obtain a vast selection of high redshift candidates at $z > 8$. These surveys have enabled the estimation of the star formation rate density at $z = 9 - 10$ and provided magnification opportunities to access intrinsically faint, low-mass galaxies, improving our understanding of the faint-end slope of the UV LF [74]. However, they were not explicitly optimized for discovering high-redshift

candidates suitable for comprehensive follow-up studies.

The Reionization Lensing Cluster Survey (RELICS) aimed to fill this gap [36]. This survey targeted 41 massive galaxy clusters detected by the Planck survey, with imaging spanning from 0.4 to 1.7 μm (HST) and 3.0 to 5.0 μm (Spitzer). Its mission was to discover the best and brightest high-redshift candidates from the first billion years after the Big Bang, in order to provide the best possible sample for the first JWST observations, which is now able to investigate their properties and luminosity functions.

2.1.2 Selection of the candidate dropouts

In this section, the procedure that led to the construction of the sample later analyzed in this work is going to be presented. This selection was made by Rodighiero et al. [1], of whom work is reported and summarized. A short explanation of how these kind of sources are selected is included, highlighting that each method successfully target a precise class of galaxies.

Dropout technique

The Lyman-dropout technique is a powerful method employed in the field of astronomy to identify and study high-redshift galaxies, particularly those in the early Universe. This technique relies on the identification of a characteristic feature in the spectra of these galaxies, known as the Lyman break, which is defined as a significant drop in the flux of a galaxy's SED at a specific wavelength, precisely 912 Å if the measurements are executed in the galaxy's rest-frame. This abrupt decline is due to the presence of a spectral discontinuity created by the Lyman limit, beyond which hydrogen in the interstellar medium absorbs photons in the ultraviolet range. Even massive, young stars, which are prolific emitters of ultraviolet radiation, emit relatively few photons below this limit.

However, due to the increasing absorption by the intergalactic medium (IGM), this drop is shifted at longer wavelength moving toward higher redshift, arriving at 1216 Å rest-frame when moving at $z \gtrsim 5$. In the context of high-redshift galaxies, the Lyman-dropout technique capitalizes on the near-ubiquity of this Lyman break feature in their spectra. The method involves conducting ultradeep imaging, often in multiple specific filters, near the Lyman limit. These filters are chosen to isolate the Lyman break itself and the blue continuum on either side of the break, making it possible to see that the spectral energy distribution of a high-redshift galaxy typ-

ically exhibits a sharp decline in flux near it, effectively "dropping out" the Lyman continuum in the SED. This drop can be observed in Fig. 2.2, where in the work of Donnan et al. [24] this technique is effectively exploited to recover the redshift of a galaxy. One of the advantages of this technique is that it is not particularly sensitive to assumptions about the intrinsic spectral energy distribution or self-absorption of the galaxies near this wavelenght.

Figure 2.2: In this figure, the Lyman Break is employed to identify the redshift of this galaxy at $z \sim 16.7$. The decline in flux at wavelenghts shorter than the Lyman limit is evident.
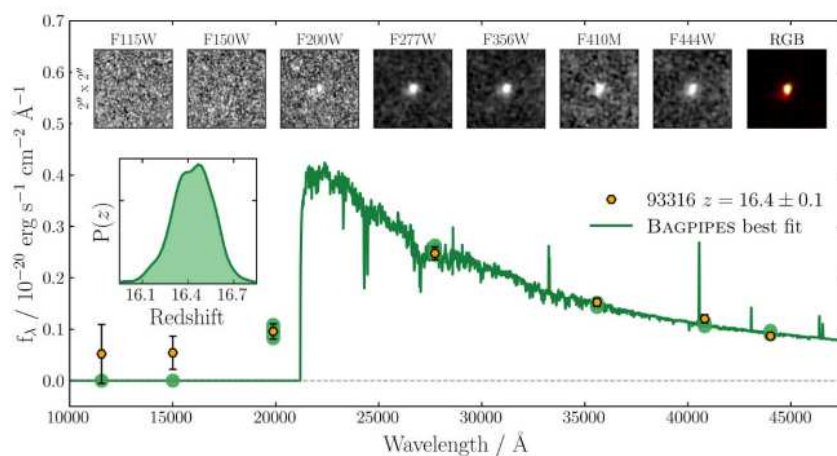
Credits: paper by Donnan et al. [24].

Practically, this technique is applied to blank fields of the sky, where astronomers perform deep imaging. By examining the colors of galaxies, researchers can readily differentiate high-redshift galaxies, exhibiting the Lyman-dropout signature, from other objects in the field. This differentiation is based on the distinctiveness of the Lyman break in the SED, coupled with the observed colors.

The Lyman-dropout technique has been instrumental in discovering and studying galaxies at high redshifts, significantly extending our understanding of the early universe. It is particularly useful for identifying galaxies in the epoch of reionization, as they are likely to be intrinsically faint and challenging to detect through other means. This technique has complemented other approaches such as gravitational lensing and deep blank-field surveys, enabling astronomers to probe the characteristics and properties of galaxies during the first billion years of the universe's existence [75].

However, while this method is relatively straightforward, it is also prone to sub-

stantial incompleteness and contamination. Notably, the LBGs selection is predisposed to significant biases towards relatively young, massive and actively star-forming galaxies, often overlooking the most massive or dust-obscured ones in the ultraviolet spectral range, since this selection method is applied mainly in the H band, which corresponds to the UV rest-frame for galaxies at $z > 3$, and therefore does not account for dust emission and consequently for the star formation hidden by the dust itself.

Alternative, independent near-infrared color criteria have been proposed to extend the catalog of high-redshift populations. To do so, Wang et al. [5] have outlined a method that enables a relatively precise selection of galaxies at redshifts greater than 3, introducing a novel color criterion, $H - [4.5] > 2.25$, for identifying Extremely Red Objects with distinct H and IRAC colors, termed HIEROs, which predominantly consist of obscured and dusty systems, including sources emitting submillimeter radiation. These galaxies typically possess substantial stellar masses ($M_* \gtrsim 10^{10} M_\odot$) and exhibit high star formation rates (SFR $\gtrsim 200 M_\odot yr^{-1}$) at an average redshift of around 4. They are characterized by low number densities and vigorous ongoing star formation processes, contributing to the SFRD in the redshift range between 3 and 5. Furthermore, they make up a substantial fraction ($\sim 50\%$) of the high-mass end of the stellar mass function. Determining the number density and star formation properties of these galaxies is essential to obtain a complete view of both galaxy stellar mass functions and cosmic SFR densities at high redshifts.

Regardless the importance of discovering the properties of these galaxies, most of their physical characteristics remain unproved, with only a few instances of spectroscopic confirmation documented in the literature.

Heavily obscured galaxies

The images of the deep survey conducted with the James Webb in the SMACS 0723 cluster are analyzed in the work of Rodighiero and her team [1], who examined the NIRCam and MIRI images, with the purpose of identifying sources in the F444W band that lacked counterparts in the F200W band, resulting in F200W dropouts. The candidates selection process was meticulous, leading to the identification of a robust sample of 19[1] sources. These candidates were visually inspected to remove any spurious or contaminated objects, ensuring a high-quality sample.

---

[1]In the paper 20 sources are mentioned, but due to a typo Morar (ID_R23 = 18) was a repetition of another object.

The authors conducted a comprehensive photometric analysis on the selected sources. They extracted cumulative light profiles from sky-subtracted images, accounting for contamination from both point-like and extended sources. The background and noise levels were determined in order to subtracted the former from the images. The radial profiles and growth curves of the sources were extracted, allowing for the measurement of fluxes using variable apertures tailored to each target. Flux uncertainties were estimated using a Monte Carlo approach. The photometric technique is explained more in detail in Section 2.2.2.

Going further on with the analysis, the redshift and the physical properties of the galaxies were derived using `Bagpipes` [76] (see Section 2.4.1), which was applied considering a wide range of stellar population models and explored various star formation histories, ages and extinction values. The code was able to provide insights into the redshifts, stellar masses and star formation rates of the selected sources. To rule out the possibility of false positive, the authors also considered the spectral properties of local brown dwarfs as potential models to fit the observations, retrieving that there is no candidate where this model is preferred.

Ultimately, the authors discuss the various classes of sources identified in their deep JWST survey within the SMACS0723 cluster, focusing on the physical properties of the identified populations. The following main classes of sources are outlined:

1. **Low-Redshift Contaminants ($z < 3$):**

   - *Red and Dusty Low-z Dwarf Galaxies.* Four sources are consistent with templates of galaxies at $z < 0.5$, characterized by low stellar masses ($log(M_*/M_\odot) \sim 5 - 7$, values even lower than Low Surface Brightness (LSB) galaxies at $z = 0$) and SFRs in line with the faint end of the Main Sequence (MS) in the local Universe. These JWST dwarves exhibit significantly higher extinction values, with A_V up to ~ 5.5 mag, with respect to the standard UV selection.

   - *Low-Mass Star-Forming Sources at Cosmic Noon.* These candidates are galaxies at $z \sim 1 - 3$ with stellar masses $log(M_*/M_\odot) \sim 7 - 9$, probing the faint end of the Main Sequence.

2. **Distant Sources ($3 < z < 13$):**

   - $3 < z < 7$ *Dusty Star-Forming Systems.* Approximately 40% of the sample is situated on the MS at $z \sim 4 - 6$, with some of the candidates filling its obscured faint end that was previously missed by LBGs. In particular, two

of these sources exhibit a color difference (F200W-F444W) close to the definition of HIEROs due to their significant extinction ($A_V \sim 3$) and notably, about half of the entire sample display such red colors, emphasizing the importance of identifying these previously undiscovered populations, not detected even by HST and Spitzer. Nonetheless, these galaxies could play a significant role in the formation of massive galaxies in the present universe. The presence of very low mass galaxies but with high dust amount at these redshift was completely unexpected.

- *A Quenched, Dusty, and Massive Galaxy at $z \sim 5$?* The most extreme red source in the sample, which present a color difference F200W-F440W ~ 7 mag, can only be explained by templates of a massive, quenched galaxy at $z \sim 5.4$ with substantial dust extinction ($log(M_*/M_\odot) \sim 11.56$ and $A_V = 4.7$ mag). Given its extremely redness, additional checks were made in order to strengthen the reliability of the nature of this candidate. They regard this source, Klama (ID_R23 = 2), as a highly likely candidate for a quiescent galaxy with still intact dust content, which could suggest that it has undergone a recent quenching process.

- *Extinguished High-z Star-Forming Sources ($7 < z < 13$).* Leaving the dust parameter in the SED fitting free to assume any value up to $A_V = 6$ has led to the individuation of four objects at $z > 8$ with mature stellar populations ($log(M_*/M_\odot) \sim 9 - 11$) that differ from previously detected JWST sources at similar cosmic epochs due to their extreme dust content ($A_V = 0.4 - 5.8$ mag). This discovery highlights the potential existence of obscured systems in the early Universe that are currently unexplained by theoretical models. Pennar (ID_R23 = 1) is the only candidate that has been detected also in two MIRI bands, resulting in a more precise photometric redshift estimate of $z = 12.1$.

To summarize, the survey's findings were significant, uncovering a mixed population of very red sources with a wide range of properties. Notably, the study identified evolved systems at $8 \lesssim z \lesssim 13$ with unexpectedly high dust content, challenging current model predictions. Additionally, an extremely red source at redshift $z \sim 5$ was identified, resembling a passive, quenched galaxy filled with dust.

In the end, the paper underscores the potential of JWST in uncovering new galaxy populations, and while the classification of these sources remains speculative, the results open avenues for future spectroscopic follow-ups to confirm their distances and nature. The findings also raise intriguing questions about the evolution of dust production and dust lifetime in the early Universe, particularly in the context of high-redshift galaxies.

These results are reported graphically in Fig. 2.3, where the stellar masses and the SFRs of every object are plotted. Thus, while waiting for additional spectroscopic analyses, the goal in this thesis is to execute an additional investigation on this original sample, now using newly processed images, through the means of the photometric tools and SED fitting technique presented in the next sections, aiming to verify if the retrieved physical parameters are consistent with the ones obtained in this previous survey.

Figure 2.3: The plots obtained in the work of Rodighiero and colleagues, plotting the characteristics of their sample.
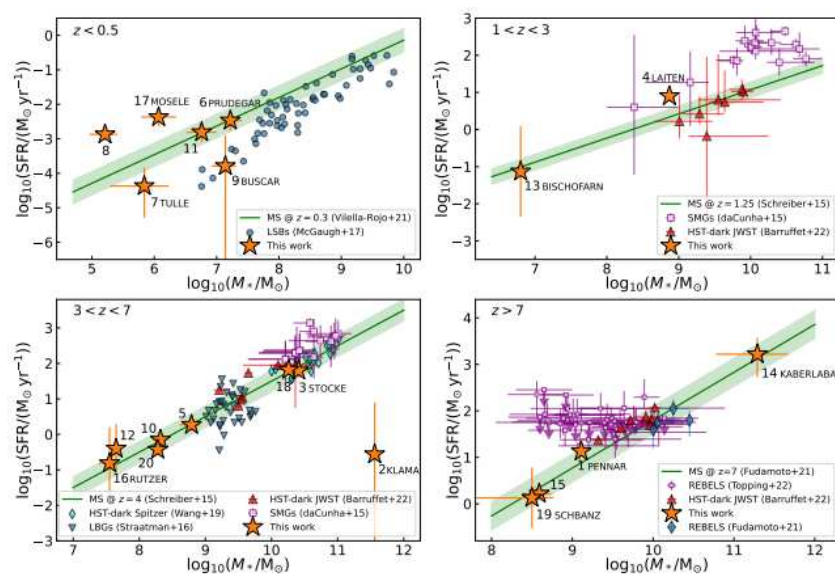
2.2 Photometric tools and comparison

In this section, the tools exploited in this study are presented, describing how they were used to acquire the sample to be analyzed.

2.2.1 Sextractor

SExtractor[2] , short for Source Extractor, is a powerful software designed for the automated analysis of astronomical images. Its primary purpose is to detect, deblend,

---

[2]Documentation available here: https://sextractor.readthedocs.io/en/latest/references.html

measure and classify sources within these images. Developed with a strong focus on handling large digital images, it has the capability to process images of considerable size, with minimal human intervention, making it particularly well-suited for the analysis of extensive extragalactic surveys.

A significant portion of contemporary astronomical research relies on catalogs of objects derived from images rather than the images themselves. These catalogs are used for various studies, such as number counts, clustering properties, or color and magnitude distributions. The accuracy and reliability of the source extraction process are of utmost importance for the success of these research efforts.

Furthermore, `SExtractor` represents a new software generation specifically engineered for batch-processing large digital images, such as those produced by modern CCD arrays, and it has been instrumental in the analysis of recent photometric galaxy surveys. The software's analysis workflow consists of six main steps:

1. *Background Estimation.* To detect faint objects and measure their flux accurately, it is essential to estimate the background level across the entire image. This requires constructing a "background map", which is generated by an estimator, which is a combination of $\kappa.\sigma-$ clipping and mode estimation, analogous to the one adopted in DAOPHOT program [77].

2. *Detection.* The software uses thresholding to identify sources without making prior assumptions about their shapes. An adaptive aperture technique is used to extract connected pixels from a "template frame" created by convolving the original image with an appropriate convolution mask. This method allows for robust detection of both stars and galaxies.

3. *Deblending.* To handle merged objects that have been extracted as a single source, `SExtractor` employs a multiple isophotal analysis technique. This technique is designed to distinguish between extended, single entities and close or interacting pairs of galaxies. It works by analyzing the distribution of light within objects and deciding whether to extract them as separate entities.

4. *Filtering the Detections.* Spurious detections can occur in the presence of shallow-profile objects, such as elliptical galaxies, when low thresholds are used. `SExtractor` incorporates a cleaning procedure that assesses whether an object would still be detected if there were no neighboring objects.

5. *Photometry.* In addition to isophotal and circular aperture magnitudes, `SExtractor` estimates the "total" magnitude of an object. This total magnitude is computed using an adaptive aperture that is effective in both non-crowded and crowded

regions. The software adapts the aperture size to optimally estimate total magnitudes for different types of objects.

6. *Star-Galaxy Separation.* Distinguishing between stars and galaxies is crucial for extragalactic studies. SExtractor employs a neural network for star-galaxy classification, which has been trained using simulated images. This classification is based on a set of parameters derived from the intensity profiles of objects.

In summary, this software is a versatile tool for automating the analysis of astronomical images. It excels in speed, robust deblending and the estimation of "total" magnitudes, making it ideal for large-scale extragalactic surveys. The incorporation of neural networks for star-galaxy classification further enhances its capabilities, ensuring accurate and reliable results for various types of astronomical objects [78].

Preliminary test and creation of the sample's catalogue

To start this work, a trial run of the software was executed by applying it to the astronomical images[3] provided in the work by Valentino et al. [79], to check if the catalogs generated by this software settings were in agreement with those presented in the aforementioned research's CEERS field. This step was done to ensure that the set-up of the program used later in the analyses was fine. In Table 2.1, the most significant input parameters that were used are reported.

---

[3]Images available at this link: https://erda.ku.dk/archives/7166d013c1ca1371aac3c57b9e73190d/published-archive.html

Table 2.1:: In this table the most significant input parameters that were used for the trial run are listed.

DETECT_MINAREA	5
DETECT_THRESH	1.3
ANALYSIS_THRESH	1.3
FILTER_NAME	tophat_4.0_5×5.conv
DEBLEND_NTHRESH	32
DEBLEND_MINCONT	0.005
CLEAN_PARAM	1.0
WEIGHT_TYPE	MAP_WEIGHT
PHOT_APERTURES	7
PHOT_AUTOPARAMS	2.5, 3.5
PHOT_PETROPARAMS	2.0, 3.5
PHOT_AUTOAPERS	0.0,0.0
SATUR_LEVEL	50000.0
MAG_ZEROPOINT	29.101920203307476
MAG_GAMMA	4.0
GAIN	0.0
PIXEL_SCALE	0.03
SEEING_FWHM	0.145
STARNNW_NAME	default.nnw
BACK_TYPE	MANUAL
BACK_VALUE	0.0
BACK_SIZE	64
BACK_FILTERSIZE	3

After establishing that the software performed as anticipated and produced a catalog comparable to the one published by Valentino and colleagues, it has been employed on the astronomical images from the SMACS0723 field, taken from the release published by Brammer[4], in which the imaging datasets are already uniformly reprocessed with updated calibration files and `grizli==1.8` software, already correcting for background.

In the repository both the science data and the variance weights are provided, so the weight map option had to be chosen. It was made run with the same input parameters used in the trial run, since the images were taken by the same instrument,

---

[4]The repository is available here: https://github.com/gbrammer/grizli/blob/master/docs/grizli/image-release-v6.rst

NIRCam, and processed with the same recipes, therefore having to apply the same zero point.

The software provides the single mode, that is the default one, and also the "double image mode", where detections are made on one image while measurements are carried out on another. Repeatedly running `SExtractor` with various "measurement images" while keeping the same "detection image" allows to end up with a set of catalogs having the same sources measured through different channels. The detection image will generally be chosen in the band where the data are the deepest, but in this case the band F444W was chosen as the detection band due to the red nature of the objects in the sample, in spite of not being the deepest available. Clearly both images must have the exact same dimensions, which was not the case for F090W, F150W and F200W with respect to our detection band, therefore this issue had to addressed. It has been overcome through the `SWarp` code[5], which allowed to resize the images based on the F444W header. An analogous procedure was also apply for the weight images.

Once the images' sizes finally matched, `SExtractor` was run once in single image mode on the F444W band image, and then in double image mode for all the remaining bands, using the 4 μm one as detection image, as mentioned above. Since the images at different wavelength present a different spatial resolution, which is quantified by the FWHM, all of them were reported to the worst spatial resolution available, the F444W band, through a convolution with an appropriate convolution kernel. Doing so, it was possible to acquire a total of six catalogues, one for each band, listing all the sources individuated by the software inside the SMACS 0723 field.

To create the sample analyzed in this work, these catalogues were cross-matched with the original sample of 19 galaxies found by Rodighiero and her team. This operation has been carried out through exploiting `TOPCAT` tool[6] [80], which allows to manipulate fits tables in a very efficient way, using a matching radius of 0.5 arcseconds.

From this cross-match, a sample of 18 sources was retrieved, leaving behind one of the objects from the original sample (Mosele, ID_R23 = 17). This non detection is probably due to the new reduction carried on the analysed images, resulting in this new `SExtractor` run not detecting it. Therefore, the IDs of this new sample match the ones from the original paper up to object 16, changing instead with our ID 17 and 18 being the original 19 and 20. The conversion along with the names of the galaxies are shown in Table 2.2.

---

[5]More informations at this link: https://www.astromatic.net/software/swarp/

[6]Official website: https://www.star.bristol.ac.uk/mbt/topcat/

Table 2.2:: The names assigned to the sources found by Rodighiero et al. [1], along with their IDs (R_23), compared to the IDs used in this work. For completeness, the position of all the objects is reported.

Name	ID_R23 (first reduction)	ID (this work)	RA [degrees]	DEC [degrees]
PENNAR	1	1	110.81984	-73.44500
KLAMA	2	2	110.70258	-73.48474
STOCKE	3	3	110.68293	-73.48773
LAITEN	4	4	110.78913	-73.47118
ORKENTAAL	5	5	110.73869	-73.49350
PRUDEGAR	6	6	110.85997	-73.46795
TULLE	7	7	110.76725	-73.48409
LAMARA	8	8	110.73693	-73.48984
BUSCAR	9	9	110.66423	-73.50227
BALDE	10	10	110.67664	-73.49635
SCHACHER	11	11	110.73417	-73.47841
TAAL	12	12	110.69481	-73.48168
BISCHOFARN	13	13	110.64479	-73.49004
KABERLABA	14	14	110.63818	-73.48639
HOLLAR	15	15	110.85694	-73.43675
RUTZER	16	16	110.77265	-73.44171
SCHBANZ	19	17	110.78847	-73.45555
BERGA	20	18	110.69837	-73.46309
near_KLAMA	missing	19	110.70252	-73.48462

For each one of the object in this new sample, which can be observed in their F444W cutouts in Fig. 2.4, SExtractor provides an estimation of the total flux and one at the aperture value specified in the input file default.sex, listed in Table 2.1. An aperture of 7 pixels of diameter has been chosen, corresponding to a radius of $\approx 0.1''$, through the conversion with the NIRCam pixel scale equal to 0.03 pixel/arcseconds.

Figure 2.4: The F444W cutout for all of the objects in the sample, where the source Klama and the companion have been collocated lastly one next to the other. All the cutouts are 71 pixels × 71 pixels, corresponding to ≈ 2.4″ × 2.4″.
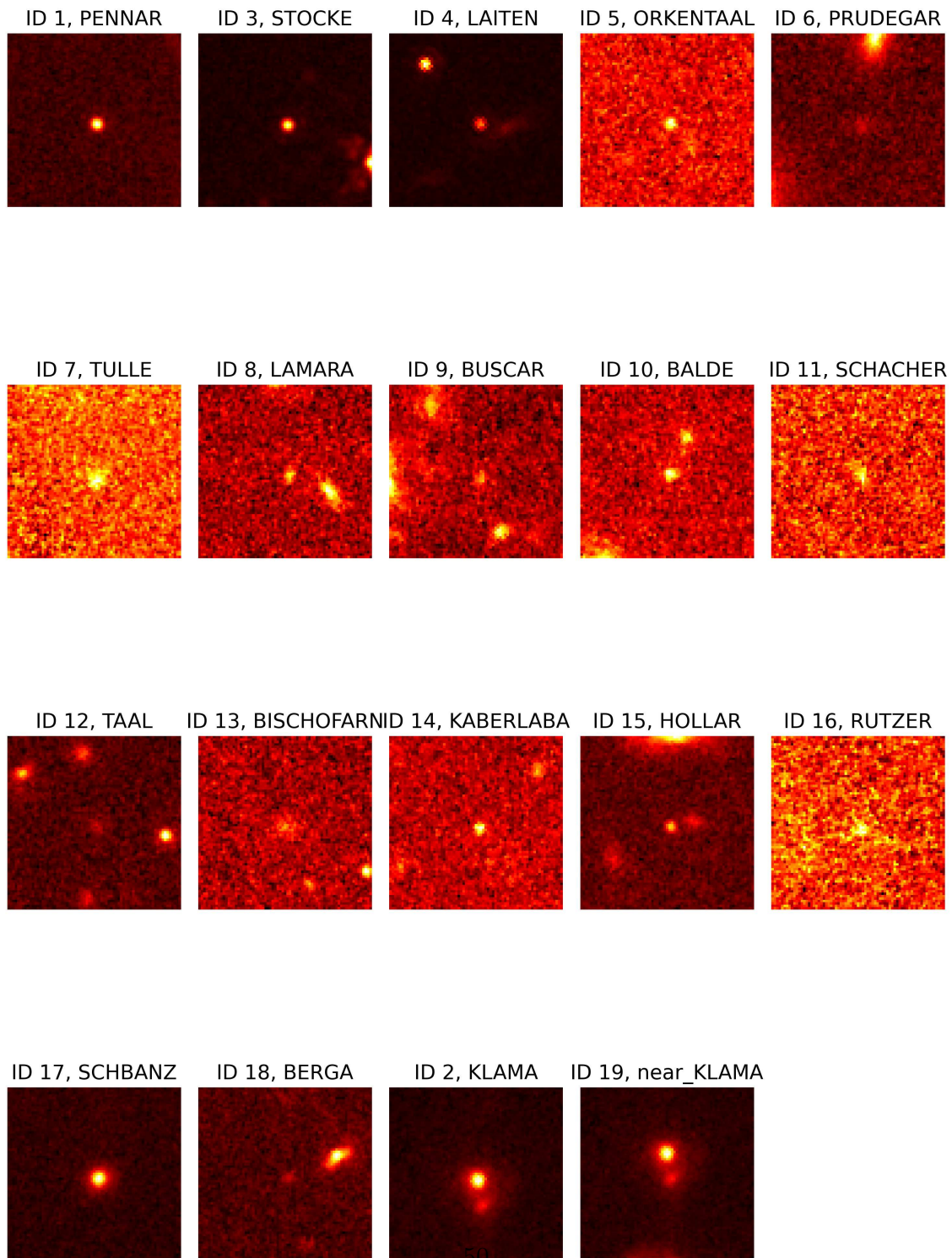
Looking at the output values, it was noticed that Klama (ID = 2) had a flux in the bluest bands incoherent with its non-visibility in them, being too high to be really referred to this source. Therefore, checking the segmentation maps, the blending of this object with a nearby companion was found, due to the small angular separation of about $0.44''$ (for comparison, the FWHM in the F444W band is of $0.145''$). Given this delicate situation, different strategies needed to be applied to be able to obtain a robust estimation of its flux. All of these discussion are relegated in an apposite section (see Section 2.3).

2.2.2 Marasco tool

The second method applied on the sample to obtain the photometry of these objects is the Marasco tool [2]. This approach is centered on extracting cumulative light profiles from sky-subtracted images while mitigating contamination from point-like sources like foreground stars and background galaxies, claiming to yield more precise measurements than traditional aperture photometry.

This procedure begins by defining a region within the image where the galaxy's contribution is negligible and the sky dominates using an ellipse, the parameters of which are manually adjusted based on the characteristics of the images. This delimitation should ideally encompass the galaxy's radial extent, inclination and position angle. Once set, these parameters remain constant for images of the same system in different bands. The outer boundary of this contour is manually adjusted for each image based on data quality and spatial extent. Pixels outside it define the 'sky' region of the image, comprising a combination of a smooth background, point-like sources such as unresolved background stars and galaxies and occasionally, resolved nearby systems.

To determine the average background intensity b and its standard deviation σ, an automatic method that filters out contamination from other components is employed. The pixel intensity distribution in the sky region is modeled using a two-component model, which includes a Gaussian and a Schechter function. This model accounts for the positive tail introduced by point-like sources. The derived background intensity is subtracted from the image.

In some cases, the model fit to the sky intensity distribution does not converge. In such instances, the determination of b and σ is executed using a sigma-rejection method applied to the filtered distribution. Occasionally, the background value is manually adjusted until the cumulative intensity profile shows the desired convergence.

Moving to the galaxy region within this border, this area can also be contaminated by point-like sources. To address this, the galaxy region is divided into concentric ellipses with the same parameters as the initial one and their intensity distribution is filtered using a sigma-rejection technique. This approach ensures that only valid data are included in the radial profile, stopping when the signal-to-noise ratio falls below one.

The cumulative radial profile, or 'growth curve', is constructed using the cleaned image. The outermost data points of the profile are crucial in assessing the quality of the photometry. If these data points show a flattening, it indicates that the sky background has been correctly determined and additional flux from the galaxy beyond the outermost annulus is negligible.

However, a flat profile can be influenced by factors such as poor masking of point-like sources. To address this, the background value can be adjust manually, if necessary. A change of slope in the outer region could also indicate a background calculation error.

The masking of point-like sources within the galaxy region carries the risk of inadvertently removing genuine galaxy features, particularly bright star clusters. Parameters for the masking method are selected so that the fractions of masked pixels in the sky region and galaxy region are statistically similar, minimizing the removal of true galaxy features. Fewer features are typically masked near the galaxy's center, where the surface brightness is higher than possible contaminants.

Uncertainties in the flux measurements are calculated as the quadratic sum of two components: errors due to image noise ϵ_σ and methodological errors ϵ_{met}. Image noise errors are determined by producing multiple stochastic realizations of the cleaned, background-subtracted image, considering pixel intensity and sky background. Each realization provides an estimate of the galaxy flux, therefore the error associated to the image noise is determined as the standard deviation of these measurements. Methodological errors, on the other hand, are evaluated by repeating the entire photometric analysis procedure with variations in key parameters. These parameters are randomly selected within specified ranges. The standard deviation of the resulting flux estimates is used to compute the error associated to the methodology.

In most cases, ϵ_{met} is the primary source of uncertainty, while ϵ_σ is relevant primarily in images with very low signal-to-noise ratios. This approach is tailored to provide robust and accurate photometry, offering a balanced compromise between accuracy and computational efficiency.

To apply this method, it is necessary to provide the cutouts of each one of the

objects, for all the six bands available. These cutouts were derived implementing a `Python` code to get a 101×101 pixels cutout centered on the source, corresponding to $\sim 9 \, \mathrm{arcsec}^2$. To make the photometry code running properly, the empirical FWHM of the Point Spread Function (PSF) for each band in arcseconds had also to be provided. They were retrieved on the official documentation page of NIRCam instrumentation[7].

Finally it was possible to run this code, adjusting manually the parameters when needed. The plot retrieved from one of the sources is shown in Fig. 2.5, to exhibit an example of the output retrieved. In particular, the mask value had to be manually changed in various cases, either to increase the mask coverage or to reduce it, due to the masking of the central source. In some cases, the output flux was zero, indicating a not properly functioning of the code. Looking carefully, it was noticed that this problem was present when the code could not calculate the position angle and/or the inclination of the galaxy. For these seven objects (ID $= 3, 6, 9, 11, 13, 14, 18$), these coordinates have been manually inserted based on the ones retrieved by the program itself on another band, in order to fix them. In this way the tool was able to provide an estimation of the fluxes for each source at each band.

Figure 2.5: An example from the object ID $= 17$ to show the outputs obtained from the Marasco tool.
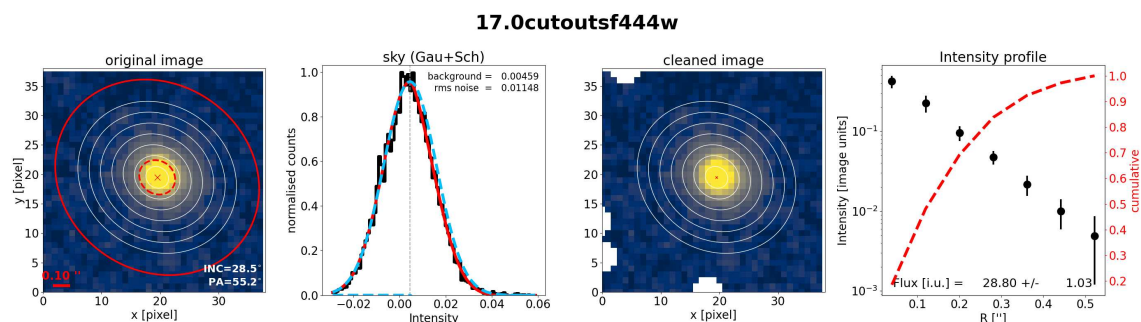
2.2.3 Excluded softwares

When this thesis was first thought of, the idea was to include even more photometric techniques in order to achieve a higher completeness in our investigation. However, these softwares ended up to not be included in this work. In the next sections, the not utilized softwares are briefly presented, explaining why they were not the most suitable choices for our analyses.

---

[7]Available at: https://jwst-docs.stsci.edu/jwst-near-infrared-camera/nircam-performance/nircam-point-spread-functions

T-PHOT

`T-PHOT`[8] [81], developed by the Astrodeep collaboration, is an innovative photometry software tailored for precision measurements in complex, deep extragalactic regions and it builds upon earlier software like `TFIT` [82] and `CONVPHOT` [83].

`T-PHOT` leverages high-resolution data as priors for object position and morphology. These priors can be 2D profiles from the high-resolution image, obtained from a detection catalog and segmentation map, input analytical models, such as Galfit stamps, or a list of positions for unresolved objects.

By convolving these data with a convolution kernel, `T-PHOT` generates low-resolution templates for accurate photometric measurements on a lower resolution image of the same area. Compared to its predecessors, `T-PHOT` offers significant improvements in speed (up to 100 times faster than `TFIT` with equivalent settings), precision and versatility. It has demonstrated its effectiveness across a wide range of images spanning from far-infrared to ultraviolet wavelengths, making it a valuable tool for photometric analysis.

Originally, this project intended to incorporate the `T-PHOT` software into the analysis pipeline as well. However, this proved unfeasible due to the absence of an updated version, with the available one being compatible only with environments utilizing `Python 2.7`. Furthermore, the primary suitability of `T-PHOT` is for point-like sources, whereas a varied sample is present in this work.

Galfit

Galfit version 3[9] is a two-dimensional fitting algorithm, designed for the analysis of structural elements in digital images of celestial objects, particularly galaxies. This innovative method enhances existing 2D fitting algorithms by accommodating unconventional features like irregular, curved, logarithmic and power-law spirals, rings and truncated shapes, providing more options than traditional parametric profiles.

These new features can be flexibly combined and applied to multiple model components of various profile types, enabling the generation of realistic galaxy model images. Despite the potential complexity, fundamental parameters such as the Sersic

---

[8]Documentation available at: http://www.astrodeep.eu/t-phot/

[9]Galfit home page: https://users.obs.carnegiescience.edu/peng/work/galfit/galfit.html

index and effective radius retain their intuitive interpretations.

The enhanced capabilities of this algorithm offer opportunities to quantify galaxy asymmetry, assess low surface brightness tidal features both inside and outside luminous galaxies, achieve more realistic dissection of galaxy subcomponents in the presence of prominent rings and spiral arms and provide a means to evaluate uncertainties during the decomposition of galaxy subcomponents [84].

At the beginning of this thesis, it was thought to use Galfit for its ability of calculating the redshift of near sources in an independent way, in order to be able to understand whether they are interacting at the same redshift, or just close on the line of sight but physically separated. Regrettably, in the case where its application was needed the most, concerning the complex blending of Klama and its companion (see Section 2.3), it was not useful, since it was unable to converge to a solution regarding the redshifts of these two proximate sources.

2.2.4 Fluxes correction

Aperture photometry is a fundamental technique in astronomical image-data analysis used to measure the brightness of celestial objects, from stars to galaxies. It calculates the object's intensity by summing the measured counts within a specific region, called the "aperture", that encloses the object while subtracting the estimated sky background. Typically, this area is centered on the object of interest, although its precise placement does not significantly affect the outcome of the calculation. In certain cases, however, it may be desirable to slightly offset it from the source's center to mitigate any influence from nearby sources. The simplest form is circular, but its shape may be adapted to suit the specific characteristics of the astronomical object being studied. For instance, a spiral galaxy observed at an oblique angle might necessitate an elliptical one. The choice of its size affects signal-to-noise ratios and larger apertures introduce more noise.

The estimation of the sky background is carried out by defining an annulus centered on the source, under the assumption of uniform background across the aperture. The shape of this annulus may be either circular or elliptical, with the annular region being at least as large as the aperture itself to exclude a significant portion of the source's signal for accurate background estimation. The geometric parameters, such as the inner and outer major and minor radii of the elliptical annulus, determine the number of data samples employed in background estimation. These parameters need to strike a balance, ensuring that the calculation remains local to the source while providing a sufficient number of samples to minimize statistical uncertainty effectively

[85].

Out of the three methods used to retrieve flux estimates, two of them are aperture techniques. This means that the output is not the expected flux value produced by the totality of the source, but just the one inside a specific radius, as just explained. In the case of `SExtractor` aperture photometry, the radius must be manually chosen and it was decided to fix it at $\sim 0.1''$ (corresponding to a diameter of 7 pixels, as previously mentioned), while in the case of the Marasco tool the radius is picked by the program itself, selected to optimize the photometry. The value of this radius is given by the parameter `morph.Rlast_arcsec`.

The radius choice for the `SExtractor` aperture photometry was made with the purpose of capturing a representative portion of the source's radiance without risking to include some nearby sources' emission, given that companions are present for some of the objects in our sample.

To correctly compare the fluxes from the different methods, the reconstruction of the total flux emitted by the source also for these two cases where it is not directly provided is necessary, therefore accounting for the source intensity extending beyond the selected region, through the application of an "aperture correction". In theory, this correction is always required due to limited bandwidth considerations, but in practice, it may be omitted for sufficiently large radii.

This correction is applied through the multiplication of the aperture flux with a correction factor, operation that allows to end up with the total flux. For the band F090W the specific file "Encircled Energy" available in the NIRCam instrument documentation[10] was used, which provides the correction factors to apply for a given radius, expressed in arcsec, in NIRCam images; while for the remaining bands the correction factors provided by Finkelstein et al., empirically obtained from studying stars present in the CEERS field [19], have been used. These latter correction factors are provided in a file where each line corresponds to a pixel, starting to count from the center of the image. Therefore, the wanted values were the ones found at the third line for the `SExtractor` aperture photometry fluxes, while the parameter `morph.Rlast_arcsec` had to be converted from arcseconds to pixels for the Marasco tool. To properly convert between pixels and arcseconds the NIRCam scale was necessary, equivalent to 0.03 pixel/arcseconds.

---

[10]NIRCam documentation: https://jwst-docs.stsci.edu/jwst-near-infrared-camera/nircam-performance/nircam-point-spread-functions

2.3 Klama

Klama (ID = 2) is the most interesting source in the sample and its analysis provided many complications, due to the presence of a nearby galaxy. Their closeness made it really hard to distinguish the light coming from one source by the one's companion, degrading the reliability of the results. Therefore, other strategies needed to be exploited with respect to the rest of the sample to achieve a satisfactory outcome and in this section they are going to be presented. Due to its role in our investigation, the Klama's companion was thus insert in the sample, being assigned to the ID 19. The duo and the nearby structure are visible in Fig. 2.6.

Figure 2.6: In this cutout Klama, the companion and the arched structure below them are visible. These complex of galaxies will be studied in a future paper (see Section 3.4.1).
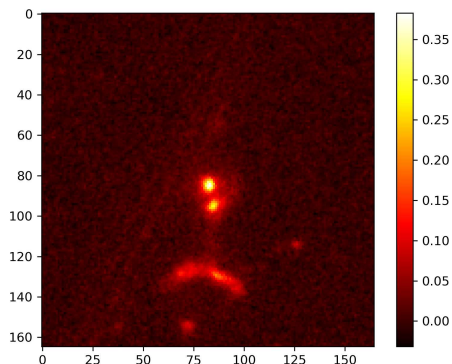
2.3.1 Sextractor

To be able to properly deblend the two targets, the parameters setting used for all the other objects, as listed in Table 2.1, was not useful. Indeed, it was necessary to change some values in order to successfully account the two galaxies as separated sources, especially changing the parameters linked to the selected threshold value above which a detection is counted and the ones establishing the deblend settings, such as the minimum contrast necessary for deblendig. In Table 2.3 the parameters that had to be changed are listed, reporting the new value assumed in this Sextractor run. The not listed ones are kept equal to the previous running of the software. Both the aperture and the total photometry of the Klama and the companion were retrieved.

In this way it has been possible to obtain a catalogue where these two sources are considered individually. As before, the procedure is the same as done for the other 17 objects: the aperture flux must be corrected to be comparable with the total one, for each band.

Table 2.3:: Parameters changed in the default.sex file to successfully deblend the Klama and the companion.

DETECT_MINAREA	3
DETECT_THRESH	1
ANALYSIS_THRESH	1
DEBLEND_NTHRESH	64
DEBLEND_MINCONT	0.0005

2.3.2 Marasco tool

To correctly consider in the analysis the sole contribution of the Klama's flux, and not the addition related to the companion, the radius inside which the flux was computed had to be manually reduced, delimiting the source from the background. It was necessary to arrive at a radius equal to $0.1''$ to obtain a decent result, imposing the parameter `RMAX_arcsec` $= 0.1$. Various possibilities were explored, such as keeping a slithgly bigger radius (0.2 arcsec) and increasing the mask value, but the solution presented here was the one that allowed to obtain the most satisfactory output.

Again, the same correction procedure was applied to retrieve the estimation of the total flux emitted by Klama and the companion separately.

2.3.3 Spatially resolved

`piXedfit` [86] is a Python package designed for analyzing spatially resolved properties of galaxies using multiband imaging data alone or in conjunction with integral field spectroscopy data. The package consists of six modules and its primary focus is on pixelized SED fitting. The SED-fitting module employs Bayesian inference with two posterior sampling methods: Markov Chain Monte Carlo (MCMC) and random dense sampling of parameter space (RDSPS).

Notably, the RDSPS method offers comparable fitting results to MCMC but is significantly faster. The package also includes a parallel computing module for efficient analysis of large datasets. `piXedfit` is modular, allowing users to run specific

modules independently. For example, the SED-fitting module can be used for integrated SED fitting without the necessity of employing other modules. This modularity enhances the versatility of `piXedfit`, making it beneficial for various applications.

The SED fitting in `piXedfit` is executed by the `piXedfit_fitting` module, capable of performing SED fitting on both photometric and spectrophotometric SEDs. Overall, `piXedfit` appears to be a comprehensive and efficient tool for analyzing spatially resolved properties of galaxies [87].

Therefore, to analyze the delicate situation presented by Klama and its companion, this tool has been exploited in order to maximize the photometric information of this system. The spatially resolved SED fitting approach has been already successfully applied to estimate photometric redshifts in two dimensions and stellar population properties on a pixel-by-pixel basis in JWST samples [88, 89].

The photometric redshift and the physical properties of the system have been obtained from spatially-resolved SED fitting on the same pixel scale of the JWST observation, $\approx 0.3''$. The procedure consists of starting with the PSF-matching of every image to the one from F444W band, proceeding with the measurements of the flux and associated error in every pixel at each filter, to finally being able to apply the SED-fitting method, deriving the physical properties of the individual pixels.

The results of this analysis will be presented in a future paper (see Section 3.4.1).

2.4 SED fitting

2.4.1 Bagpipes

`Bagpipes`[11], short for Bayesian Analysis of Galaxies for Physical Inference and Parameter EStimation, is a powerful `Python` tool designed to generate detailed model galaxy spectra and fit them to a wide range of observational data. This versatile software utilizes the `MULTINEST` nested sampling algorithm to infer the physical properties of galaxies and perform parameter estimation.

In the realm of astrophysics and galaxy studies, understanding the physical attributes and evolutionary history of galaxies is crucial. This entails modeling the light emitted by galaxies across a wide range of wavelengths, contingent upon the physical parameters governing these systems. These parameters encompass properties

---

[11]Official documentation at: https://bagpipes.readthedocs.io/en/latest/

such as the age of stellar populations, stellar metallicity and star formation history (SFH). In order to gain insights into these parameters, astrophysicists employ models that can be compared to observational data, which includes both spectroscopic and photometric information, often referred to as the SED.

`Bagpipes` represents a significant advance in the field of galaxy spectral modeling. It overcomes the limitations of traditional methods, such as data compression or the use of pre-calibrated spectral indices. With the development of advanced Bayesian statistical techniques and nested sampling algorithms, `Bagpipes` facilitates the exploration of high-dimensional parameter spaces, allowing for more accurate and comprehensive modeling of galaxy properties.

The core feature of `Bagpipes` lies in its ability to efficiently generate complex model galaxy spectra, spanning from the far-ultraviolet to microwave regimes. Users can specify the level of complexity by incorporating various model components, such as dust and nebular-emission prescriptions, as well as diverse SFH components. The software then uses these components to create an internal model of a galaxy spectrum. The generated model can provide spectral data over a user-defined wavelength range, photometric fluxes through specific filters and emission-line fluxes. These spectra are critical for matching with observed data to infer galaxy properties.

The `Bagpipes` models are composed of several components, including:

1. *Simple Stellar-Population (SSP) Models.* These are a function of wavelength, stellar population age, stellar metallicity and the initial mass function (IMF). The 2016 version of the Bruzual & Charlot [90] models is integrated into `Bagpipes`.

2. *Star Formation History (SFH).* This component describes the rate of star formation as a function of time and is composed of one or more SFH components. Users can employ multiple SFH components to describe various star formation epochs.

3. *Transmission Functions.* `Bagpipes` accounts for ionized gas in the interstellar medium, emission and absorption processes, ionized continuum emission and emission from warm dust within HII regions. The software also includes a transmission function for neutral ISM, which deals with diffuse dust attenuation and emission.

4. *Nebular-Emission Models.* `Bagpipes` employs a nebular-emission model that describes emission from HII regions of different ages, factoring in the metallicity of the ionized gas.

5. *Dust Models.* `Bagpipes` supports various dust models, such as the Calzetti law [91], the Milky Way dust law [92] and a flexible model [93]. These models account for dust attenuation and emission in galaxy spectra.

To model spectral features accurately, `Bagpipes` introduces the concept of spectral resolution, enabling the consideration of velocity dispersion effects. The software can convolve the spectrum with a Gaussian kernel in velocity space to represent velocity dispersion in the observed galaxy.

The second crucial aspect of `Bagpipes` is its capability to fit these detailed models to the observations, provided whether in the form of observed spectra or photometry. Users define prior probability distributions for the model parameters and insert the data with the respectively uncertainties and the software refines these parameters based on them, employing Bayesian inference. The likelihood function, taking into account Gaussian and independent uncertainties, integrates the data into the parameter estimation process.

`Bagpipes` employs the `MULTINEST` nested sampling algorithm to derive the posterior distribution of parameters and the evidence value for a given model, prior distribution and observational data. This approach is highly efficient in exploring high-dimensional, multimodal and degenerate parameter spaces, often encountered in galaxy spectral fitting. The outcome is a comprehensive understanding of the physical properties of galaxies and their evolution.

`Bagpipes` is an invaluable tool for astrophysicists seeking to infer the properties of galaxies based on observed spectral and photometric data. It streamlines the process of modeling complex galaxy spectra and conducting accurate parameter estimation, enhancing our understanding of the universe's evolutionary processes and the properties of distant celestial objects [94].

This tool was exploited to extrapolate the physical parameters of the 19 galaxies present in the sample analyzed in this work, and it has been run three times, each one based on one of the three different photometric fluxes provided, obtained through the three different photometric techniques applied and explained in Section 2.2.

In Table 2.4, the prior parameters ranges provided to the code are listed. These ranges represents the limits inside which the code must explore the parameter space in order to find the estimation values that allow to retrieve a better fit to the observed data.

Table 2.4:: Input parameters for `Bagpipes` code.

redshift	0, 20
dust	
type	Calzetti
A_V [mag]	0, 6
nebular emission	
logU	-4, -2
delayed tau model	
age [Gyr]	0.001, 15
tau [Gyr]	0.01, 10
metallicity $[Z_\odot]$	0, 2.5
mass-formed $[log_{10}(M_*/M_\odot)]$	6, 12.5

As visible in the table, dust, SFH and nebular emission components have been exploited. The SFH is taken as a delayed τ model, with the parameter *age* representing the time since SF began, the *tau* one establishing the timescale of the decrease and the *mass-formed* putting a limit on the mass created in a single starburst. The delayed τ model is analytically described by the equation $t \times e^{-(t/\tau)}$ and consists of an exponential growth followed by a decrement. For the nebular emission component, the $log_{10}U$ represents the ionization parameter, while for the dust component a Calzetti law [91] is assumed, with the absorption free to vary up to $A_V = 6$ magnitudes. Lastly, the redshift has been let free to assume any value up to 20.

Thanks to `Bagpipes`, all the most important physical parameters describing the 19 galaxies were retrieved, which are going to be discussed in the next chapter.

Chapter 3

Results and Discussion

In this chapter, the photometric and SED fitting results will be showcased, engaging in a brief discussion for each retrieved parameter. Emphasis will be placed on understanding the coherence among outcomes derived from various techniques and assessing their alignment with initial estimates from the previous analyses by Rodighiero and her team [1], to also evaluate the impact of the reduction performed on the images.

3.1 Photometric comparison

To better understand the comparison between the fluxes obtained with the different techniques, they have been plotted to visually depict the agreement or disagreement. In this work a measurement has been considered as such only if respecting the condition of signal to noise ratio SNR > 3, with the SNR being calculated as *flux value/associated error*, otherwise being counted as non detection. Therefore, in the following plots, only the points with at least one valid flux measurements are reported, excluding the ones with both the measurements under the threshold value. For the cases in which just one is valid, the invalid one is reported as upper limit, thus indicated by a red arrow symbol in the direction of the limit. This upper limit has been calculated as 3 times the error both for the measurements from `SExtractor` and in the analyses conducted with the Marasco code, in which the upper limit parameter provided by the tool itself, which is in fact an estimate of the noise, has been exploited. The bisector is reported, to facilitate the understanding of the plots, which are represented in logarithmic scale. All the fluxes presented in this work are in the unit of Jansky.

Firstly, the comparison between the fluxes obtained by the Marasco tool and

SExtractor Auto mode are presented. In the F090W band (Fig. 3.1), the shortest wavelenght available, the majority of the measurements are non detections, as can be deducted by the low number of candidates plotted. Nonetheless, these few points displayed show a good agreement between the different values, with the exception of the objects 2 and 4, which is not relevant given that they both present one of the two measurements just as an upper limit, therefore not being a real detection. In the F150W (Fig. 3.2) and F200W (Fig. 3.3) bands, the situation is slightly better, with more sources detected, but still not ideal. Moving towards longer bands, it is possible to appreciate how the number of detections improves, as visible in Figure 3.4 (F277W), Figure 3.5 (F356W) and Figure 3.6 (F444W), all showing a better concordance among the two methods, having the points distribution less scattered along the bisector line. Notably, the points are distributed along a straight line, but not precisely on the bisector: it seems that a small offset is present.

Figure 3.1: Fluxes estimates from Marasco tool versus SExtractor Auto in the F090W band.
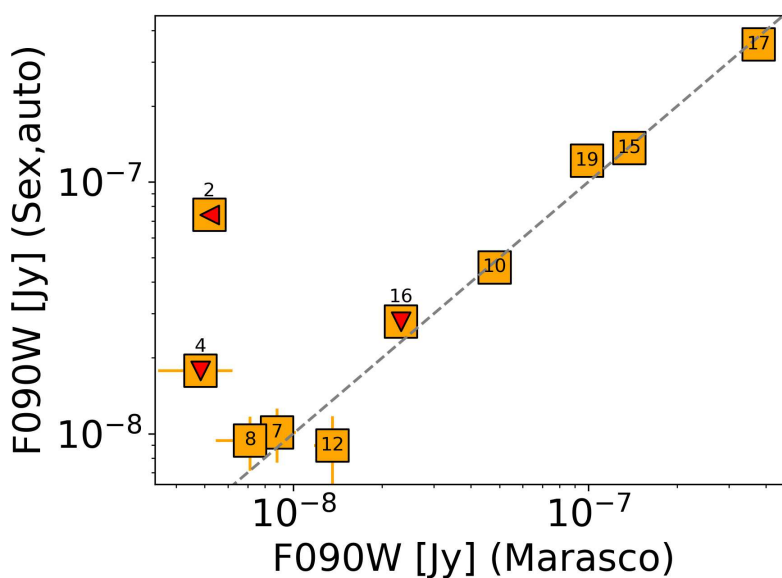
Figure 3.2: Fluxes estimates from Marasco tool versus `SExtractor` Auto in the F150W band.

Figure 3.3: Fluxes estimates from Marasco tool versus `SExtractor` Auto in the F200W band.

Figure 3.4: Fluxes estimates from Marasco tool versus `SExtractor` Auto in the F277W band.
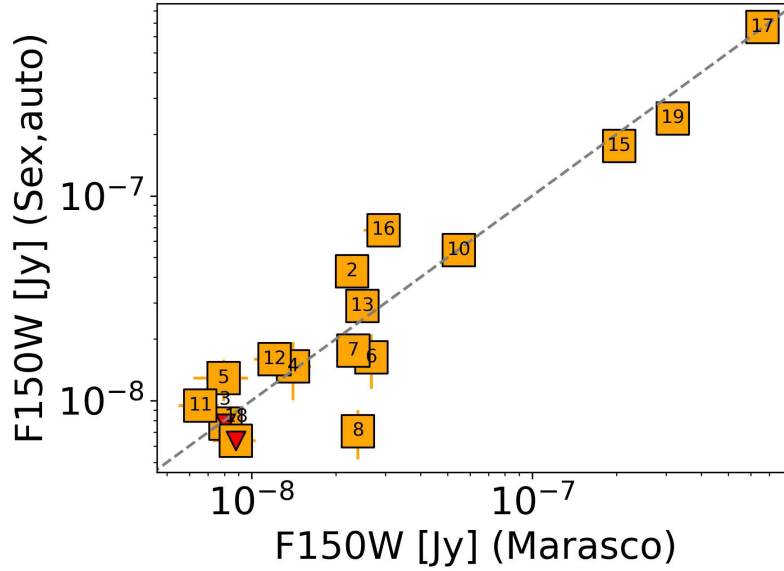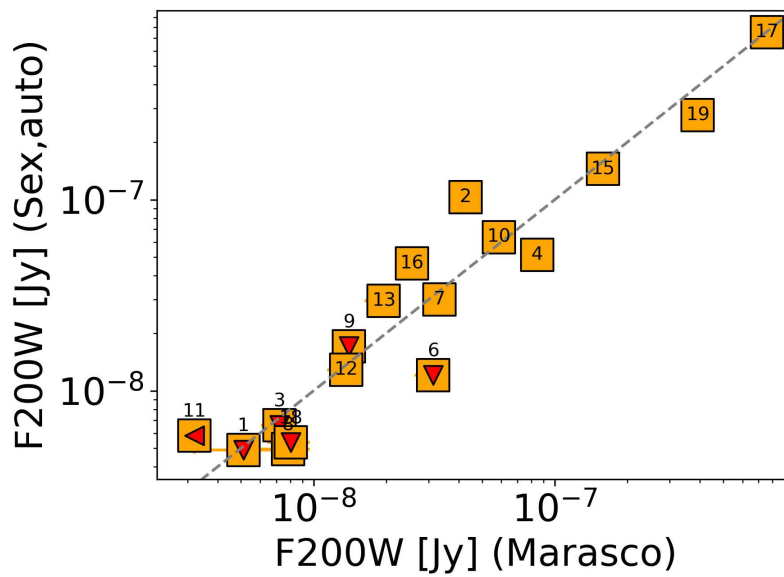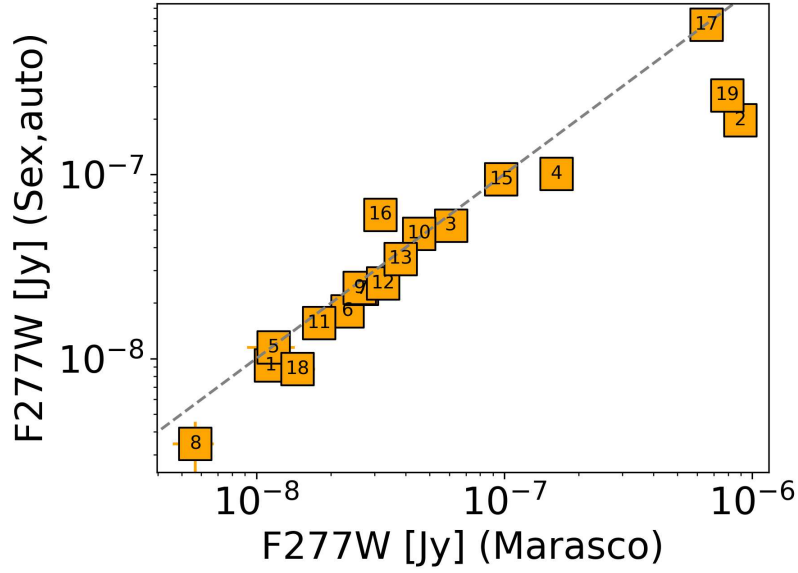

Figure 3.5: Fluxes estimates from Marasco tool versus `SExtractor` Auto in the F356W band.
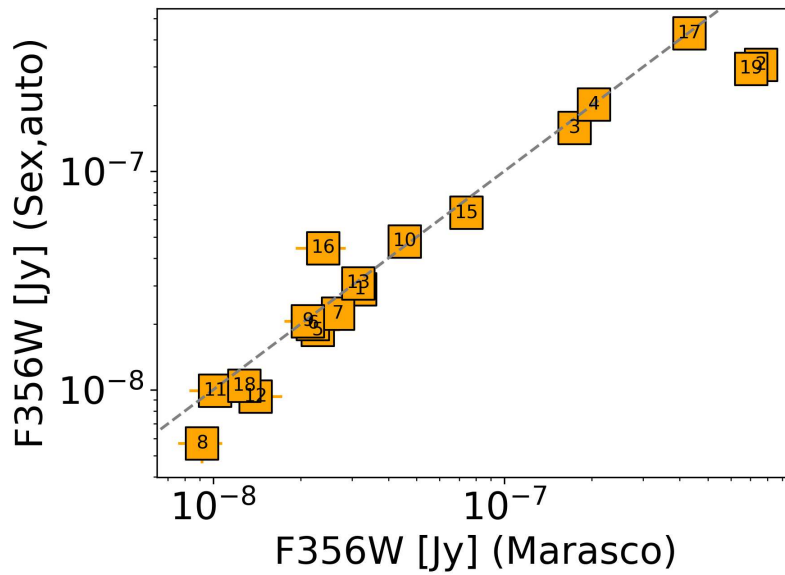
Figure 3.6: Fluxes estimates from Marasco tool versus `SExtractor` Auto in the F444W band.
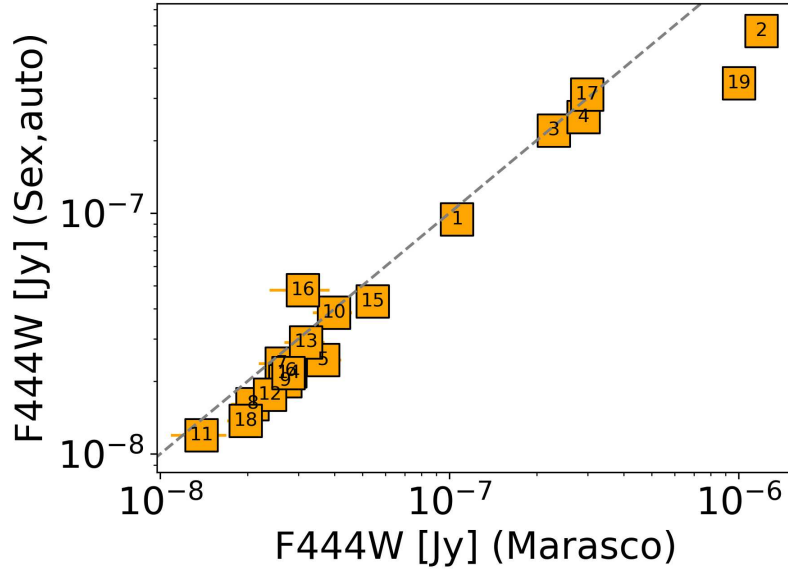
Secondly, the fluxes obtained by `SExtractor` Auto versus the `SExtractor` Aperture ones are plotted. In all the six available bands (Fig. 3.7), the discrepancy between these estimates is evident, with just few points being close to the bisector line. To not overload this work, we avoid reporting also the graphics of `SExtractor` Aperture versus Marasco tool, since they would be essentially the same as in this case, given the same behaviour of the latter in comparison with the `SExtractor` Auto.

Figure 3.7: Fluxes estimates from `SExtractor` Aperture versus `SExtractor` Auto in all the six available bands.
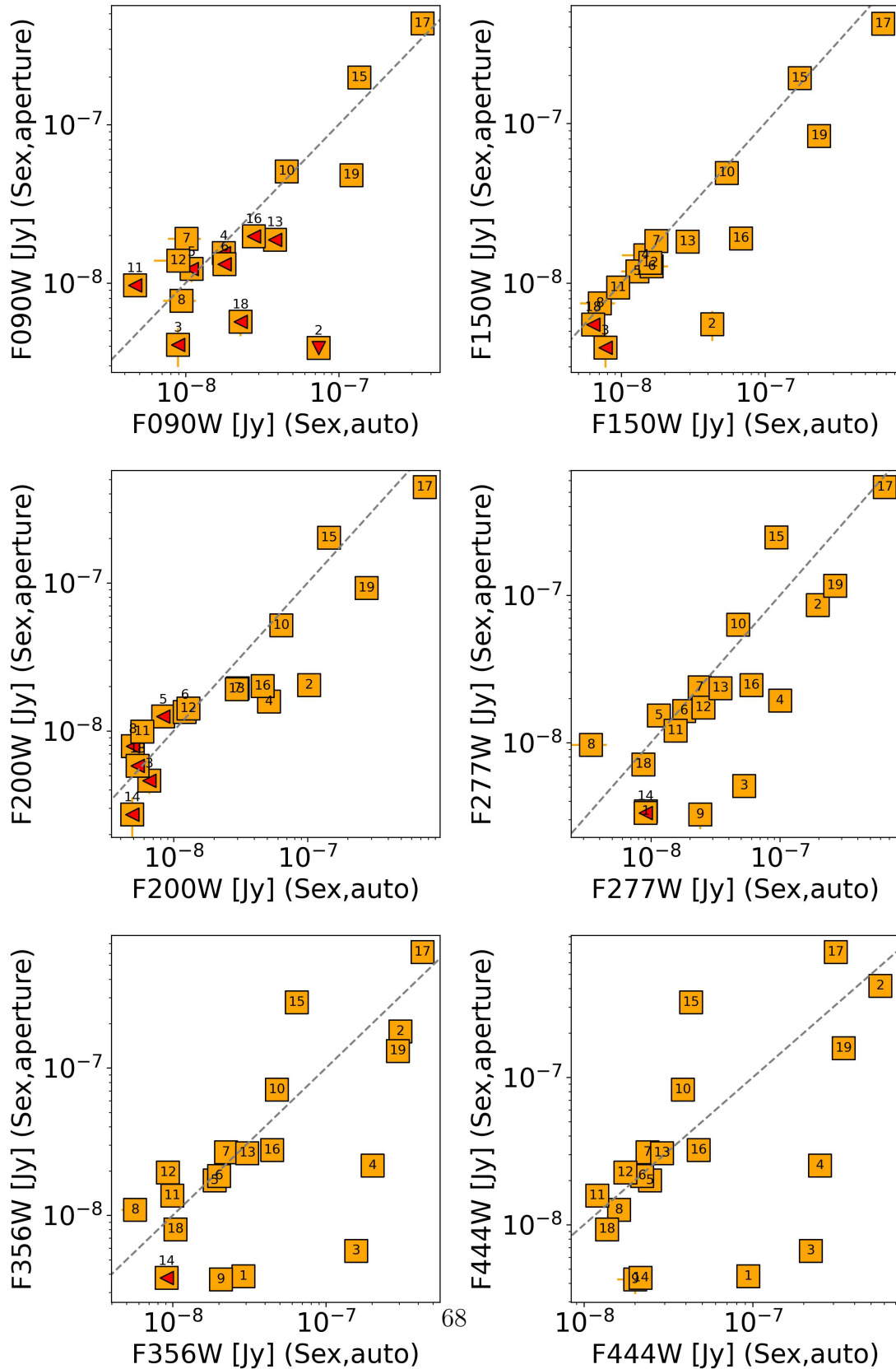
To better quantify the difference among the output fluxes of the three methods, the median of the ratio between the flux value of one method and another's has been computed with their associated standard deviations, representing their errors, for all the six bands. The ratio between the two fluxes estimates was considered valid, and therefore used in the calculation of the median, only if both of the measurements respected the threshold value of SNR > 3. The median results are listed in Table 3.1, always in the unit of Jansky.

Table 3.1:: In this table we report the median of the ratios between the three photometric results and their associated standard deviations.

Filters	Median Marasco/Sex_Auto	Median Marasco/Sex_Aper	Median Sex_Auto/Sex_Aper
F090W	0.99 ± 0.20	0.93 ± 0.47	0.81 ± 0.64
F150W	1.03 ± 0.51	1.5 ± 1.0	1.1 ± 1.8
F200W	0.97 ± 0.53	1.5 ± 1.3	1.5 ± 1.3
F277W	0.87 ± 0.34	1.6 ± 3.7	1.4 ± 2.6
F356W	0.90 ± 0.30	1.2 ± 6.9	1.1 ± 6.3
F444W	0.79 ± 0.23	1.7 ± 8.8	1.3 ± 8.3

What has been said before looking at the plot can be now be appreciated by the median values. The errors associated with the agreement between Marasco and the `SExtractor` Auto are sensibly lower than the one linked to the `SExtractor` Aperture comparison with any of the other methods, reflecting the behaviour previously showed in the plots.

From this table, it can be appreciated that the `SExtractor` Aperture estimates are systematically lower then the other methods', except for the bluer filter. This underestimation of the Aperture technique is probably due to the choice made for the radius (of $\sim 0.1''$, see Section 2.2.1), that even with the proper correction applied still enclose too little emitted light coming from the source. This choice was made to avoid nearby contaminants, such as for Klama (ID = 2, see Section 2.3), explaining why in this particular case the method provides instead a good estimate of the flux.

3.2 Physical parameters obtained

We report the dust absorption (A_V), the star formation rate (SFR), the redshift (z) and the stellar mass (M_*) retrieved by utilizing the photometry obtained with the 3 methods, each one with the relative errors. In Table 3.2 these parameters'

estimations coming out from the input fluxes values obtained from the Marasco tool photometric analyses are listed, in Table 3.3 the same results but starting from the photometry obtained by `SExtractor` Auto mode and lastly the values obtained from the `SExtractor` Aperture technique in Table 3.4. Since the `Bagpipes` code does not provide the errors directly, they have been computed using the 16th and 84th percentiles, subtracting the value found at 16% of the probability distribution from the value of the peak and subtracting from the value at the 84% of the distribution the peak one, to obtain the errors reported here. Since the errors estimation is not complete, due to the difficulty of quantifying all of them, and that physical parameters estimation based only on photometric data cannot reach such a high precision, all the error values have been rounded at maximum the second decimal unit, even if presenting less than two significant digits, because a more precise estimation is not reliable. When a value smaller than 0.01 was present, it has been rounded at this threshold value.

Table 3.2:: In this table we report the output estimates retrieved by `Bagpipes` with the Marasco tool input fluxes.

ID	z	M_* $[log_{10}(M_*/M_\odot)]$	SFR $[M_\odot yr^{-1}]$	A_V [mag]
1	$10.1^{+1.1}_{-3.7}$	$11.15^{+0.34}_{-0.83}$	1121^{+1341}_{-991}	$3.94^{+0.42}_{-0.31}$
2	$3.00^{+0.02}_{-0.03}$	9.47 ± 0.02	$29.6^{+1.1}_{-1.4}$	$5.07^{+0.04}_{-0.05}$
3	$4.86^{+0.04}_{-0.07}$	$10.28^{+0.07}_{-0.08}$	75^{+21}_{-13}	$3.63^{+0.17}_{-0.15}$
4	$11.83^{+0.26}_{-8.41}$	$10.19^{+0.39}_{-0.51}$	187^{+135}_{-176}	$1.69^{+0.89}_{-0.30}$
5	$5.9^{+2.2}_{-3.7}$	$8.71^{+0.38}_{-0.77}$	$2.8^{+5.1}_{-2.6}$	$1.36^{+0.50}_{-0.32}$
6	$9.44^{+0.63}_{-1.17}$	$8.36^{+0.22}_{-0.29}$	$2.26^{+0.58}_{-0.87}$	$0.10^{+0.11}_{-0.07}$
7	$0.19^{+0.07}_{-0.05}$	$6.29^{+0.32}_{-0.31}$	0.00 ± 0.01	$1.97^{+0.45}_{-0.48}$
8	$1.14^{+0.06}_{-0.02}$	$6.08^{+0.08}_{-0.06}$	0.01 ± 0.01	$1.39^{+0.29}_{-0.27}$
9	$11.6^{+3.1}_{-11.2}$	$8.31^{+0.79}_{-1.36}$	2^{+10}_{-2}	$1.27^{+4.27}_{-0.79}$
10	$0.19^{+0.69}_{-0.02}$	$6.3^{+1.3}_{-0.2}$	$0.00^{+0.04}_{-0.01}$	$0.53^{+0.19}_{-0.25}$
11	$2.96^{+0.25}_{-0.15}$	$7.09^{+0.31}_{-0.18}$	$0.13^{+0.15}_{-0.05}$	$1.84^{+0.26}_{-0.23}$
12	$3.49^{+0.13}_{-0.36}$	$7.61^{+0.36}_{-0.28}$	$0.41^{+0.19}_{-0.16}$	$0.53^{+0.19}_{-0.22}$
13	$7.12^{+0.18}_{-0.13}$	$8.38^{+0.24}_{-0.28}$	$2.35^{+1.14}_{-0.95}$	$0.52^{+0.17}_{-0.23}$
14	$9.7^{+1.6}_{-3.7}$	$11.12^{+0.66}_{-1.11}$	1044^{+4058}_{-989}	$5.55^{+0.34}_{-0.59}$
15	0.03 ± 0.01	$5.72^{+0.13}_{-0.06}$	0.00 ± 0.01	$0.20^{+0.16}_{-0.12}$
16	$0.76^{+2.19}_{-0.36}$	$7.16^{+0.67}_{-0.59}$	$0.02^{+0.41}_{-0.01}$	$0.28^{+0.48}_{-0.20}$
17	0.31 ± 0.01	$8.31^{+0.05}_{-0.10}$	0.00 ± 0.01	$0.04^{+0.04}_{-0.03}$
18	$8.9^{+1.1}_{-1.8}$	$8.58^{+0.24}_{-0.38}$	$2.8^{+1.8}_{-1.6}$	$0.74^{+0.33}_{-0.22}$
19	$3.15^{+0.16}_{-0.39}$	$9.41^{+0.09}_{-0.12}$	$27.8^{+4.8}_{-5.4}$	$1.58^{+0.09}_{-0.07}$

Table 3.3:: In this table we report the output estimates retrieved by `Bagpipes` with the `SExtractor` Auto input fluxes.

| ID	z	M_* [$\log_{10}(M_*/M_\odot)$]	SFR [$M_\odot\,\mathrm{yr}^{-1}$]	A_V [mag]
1	$8.9^{+2.7}_{-3.6}$	$10.98^{+0.85}_{-0.70}$	954^{+5317}_{-875}	$4.61^{+0.42}_{-0.31}$
2	5.45 ± 0.03	$9.70^{+0.07}_{-0.06}$	$60.6^{+7.0}_{-8.1}$	$1.89^{+0.04}_{-0.03}$
3	$4.55^{+0.19}_{-0.23}$	$10.10^{+0.09}_{-0.12}$	39^{+13}_{-9}	$3.39^{+0.20}_{-0.12}$
4	$3.9^{+0.19}_{-1.36}$	$9.64^{+0.08}_{-0.55}$	$10.6^{+2.9}_{-3.3}$	$2.08^{+0.88}_{-0.13}$
5	$5.4^{+2.5}_{-3.8}$	$8.52^{+0.38}_{-0.72}$	$1.6^{+2.9}_{-1.5}$	$1.52^{+1.23}_{-0.56}$
6	$1.51^{+2.47}_{-0.51}$	$7.65^{+0.57}_{-0.40}$	$0.06^{+0.50}_{-0.04}$	$0.88^{+1.34}_{-0.49}$
7	$0.22^{+1.62}_{-0.02}$	$6.35^{+1.19}_{-0.22}$	$0.00^{+0.13}_{-0.01}$	$1.73^{+0.44}_{-1.37}$
8	$5.29^{+0.23}_{-0.19}$	$6.95^{+0.97}_{-0.32}$	$0.09^{+0.61}_{-0.05}$	$0.48^{+0.82}_{-0.31}$
9	$0.6^{+13.4}_{-0.2}$	$7.18^{+1.11}_{-0.35}$	$0.01^{+1.88}_{-0.01}$	$3.47^{+1.59}_{-2.83}$
10	0.18 ± 0.01	$6.28^{+0.24}_{-0.17}$	0.00 ± 0.01	$0.65^{+0.21}_{-0.16}$
11	$2.99^{+0.25}_{-2.50}$	$7.49^{+0.09}_{-0.88}$	$0.21^{+0.06}_{-0.21}$	$0.66^{+1.28}_{-0.17}$
12	0.32 ± 0.02	$6.86^{+0.13}_{-0.35}$	0.00 ± 0.01	$1.29^{+0.48}_{-0.37}$
13	$0.68^{+2.05}_{-0.28}$	$7.38^{+0.67}_{-0.48}$	$0.02^{+0.24}_{-0.02}$	$1.12^{+0.82}_{-0.96}$
14	$9.2^{+2.3}_{-3.4}$	$10.81^{+0.81}_{-1.13}$	465^{+3039}_{-435}	$5.34^{+0.44}_{-0.78}$
15	0.03 ± 0.01	$5.73^{+0.13}_{-0.07}$	0.00 ± 0.01	$0.18^{+0.10}_{-0.09}$
16	$0.44^{+0.19}_{-0.11}$	$7.11^{+0.42}_{-0.26}$	$0.01^{+0.02}_{-0.01}$	$0.81^{+0.34}_{-0.43}$
17	0.32 ± 0.01	$8.33^{+0.02}_{-0.03}$	0.00 ± 0.01	$0.04^{+0.03}_{-0.02}$
18	$1.8^{+3.5}_{-1.1}$	$7.62^{+0.70}_{-0.71}$	$0.07^{+0.77}_{-0.06}$	$1.95^{+2.60}_{-0.84}$
19	2.22 ± 0.02	$8.31^{+0.08}_{-0.03}$	$2.38^{+0.59}_{-0.21}$	$0.86^{+0.08}_{-0.09}$

Table 3.4:: In this table we report the output estimates retrieved by `Bagpipes` with the `SExtractor` Aperture input fluxes.

ID	z	M_* [$\log_{10}(M_*/M_\odot)$]	SFR [$M_\odot\,\mathrm{yr}^{-1}$]	A_V [mag]
1	$1.84^{+3.09}_{-0.75}$	$7.01^{+0.55}_{-0.47}$	$0.02^{+0.11}_{-0.01}$	$0.59^{+0.93}_{-0.39}$
2	$5.17^{+0.23}_{-1.68}$	$10.41^{+0.09}_{-0.54}$	78^{+30}_{-32}	$3.32^{+0.89}_{-0.28}$
3	$2.5^{+2.3}_{-1.2}$	$7.27^{+0.39}_{-0.41}$	$0.05^{+0.12}_{-0.04}$	$0.25^{+0.28}_{-0.18}$
4	$4.99^{+0.69}_{-3.44}$	$8.10^{+0.24}_{-0.75}$	$0.65^{+0.38}_{-0.56}$	$0.22^{+0.17}_{-0.14}$
5	$3.3^{+2.4}_{-1.8}$	$7.94^{+0.32}_{-0.66}$	$0.33^{+0.43}_{-0.28}$	$0.21^{+0.19}_{-0.12}$
6	$4.1^{+1.6}_{-2.6}$	$7.99^{+0.28}_{-0.69}$	$0.47^{+0.39}_{-0.21}$	$0.19^{+0.13}_{-0.21}$
7	$5.01^{+0.39}_{-3.39}$	$8.16^{+0.12}_{-0.87}$	$0.82^{+0.29}_{-0.67}$	$0.16^{+0.15}_{-0.10}$
8	$5.00^{+0.70}_{-3.40}$	$7.85^{+0.22}_{-0.83}$	$0.33^{+0.15}_{-0.28}$	$0.19^{+0.15}_{-0.13}$
9	$1.60^{+2.05}_{-0.87}$	$6.87^{+0.52}_{-0.54}$	$0.01^{+0.07}_{-0.01}$	$0.75^{+1.36}_{-0.48}$
10	5.01 ± 0.01	$8.47^{+0.14}_{-0.09}$	$2.40^{+0.27}_{-0.14}$	$0.20^{+0.05}_{-0.06}$
11	$5.01^{+0.65}_{-3.44}$	$7.89^{+0.22}_{-0.84}$	$0.43^{+0.18}_{-0.36}$	$0.18^{+0.15}_{-0.10}$
12	$3.1^{+2.5}_{-1.6}$	$7.99^{+0.27}_{-0.85}$	$0.38^{+0.47}_{-0.30}$	$0.24^{+0.15}_{-0.16}$
13	$5.01^{+0.55}_{-3.40}$	$8.17^{+0.13}_{-0.91}$	$0.81^{+0.37}_{-0.66}$	$0.17^{+0.14}_{-0.11}$
14	$2.11^{+2.45}_{-0.93}$	$7.02^{+0.45}_{-0.41}$	$0.02^{+0.09}_{-0.02}$	$0.50^{+0.64}_{-0.32}$
15	5.01 ± 0.01	$9.12^{+0.06}_{-0.05}$	$10.30^{+0.32}_{-0.36}$	$0.20^{+0.02}_{-0.03}$
16	$4.99^{+0.63}_{-3.43}$	$8.18^{+0.22}_{-0.85}$	$0.79^{+0.48}_{-0.65}$	$0.21^{+0.17}_{-0.14}$
17	5.00 ± 0.01	$9.12^{+0.03}_{-0.02}$	$15.9^{+1.1}_{-0.7}$	0.30 ± 0.01
18	$3.7^{+2.0}_{-2.2}$	$7.63^{+0.29}_{-0.69}$	$0.15^{+0.19}_{-0.12}$	$0.21^{+0.21}_{-0.12}$
19	$6.04^{+0.06}_{-0.05}$	$9.06^{+0.06}_{-0.04}$	$11.62^{+0.59}_{-0.67}$	0.59 ± 0.05

Understanding the parameter distribution associated to each method for each one of these physical properties considered here through a histogram plot can be helpful to try to visualize whether the values found are in agreement between the different methods. The units are the same of the ones reported in Table 3.2.

For the redshift, the comparison with the values found in the early reduction, carried out by Rodighiero et al. this year [1], is also provided and it's visible in Fig. 3.8. These values refer to the photometric redshift of these objects, retrieved by the photometric analysis.

Figure 3.8: Histogram reporting the frequency of a certain range value of z in the sample analyzed in this work.
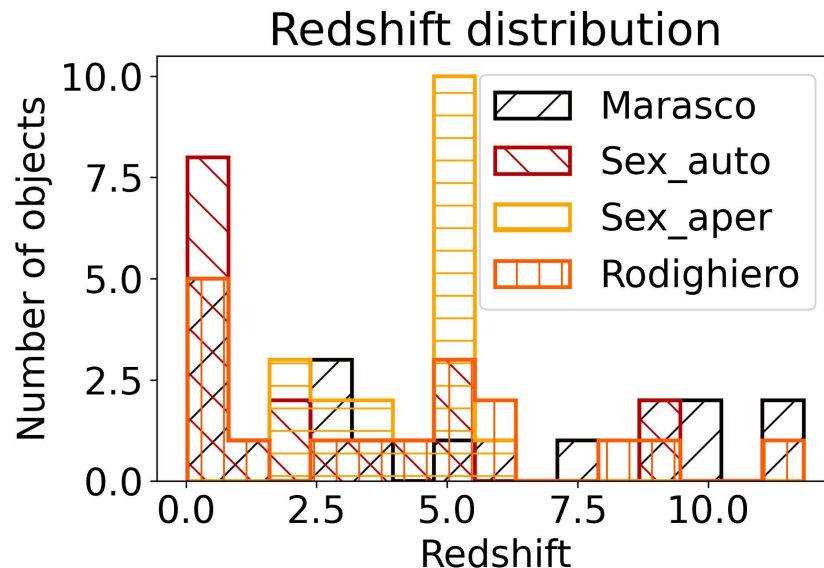
In addition, in Figure 3.9 the distribution of the dust extinction A_V is reported, in Figure 3.10 the one of the SFR, while the histogram of M_* is visible in Figure 3.11. Since in the paper the SFR parameter is reported in logarithmic form (as $log_{10}SFR$), to ensure a reasonable comparison the outputs in this work have also been converted to logarithm. To take care of the errors, the values of the 16 and 84 percentiles have been all converted, and subsequently the difference has been calculated, applying the same procedure explained before.

Figure 3.9: Histogram reporting the frequency of a certain range value of A_V in the sample analyzed in this work.
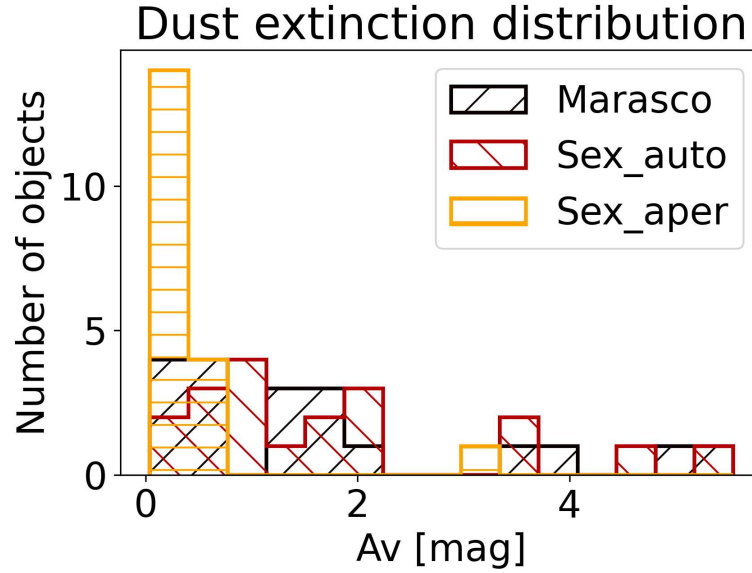

Figure 3.10: Histogram reporting the frequency of a certain range value of SFR in the sample analyzed in this work.
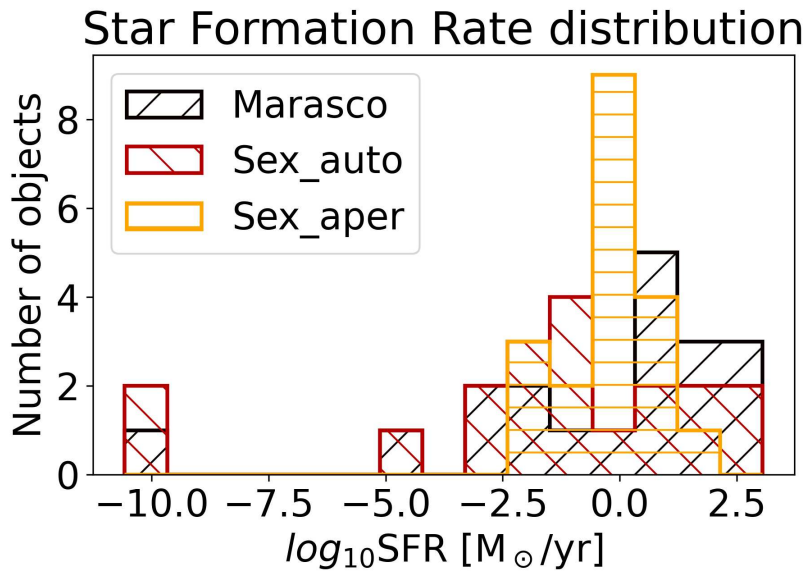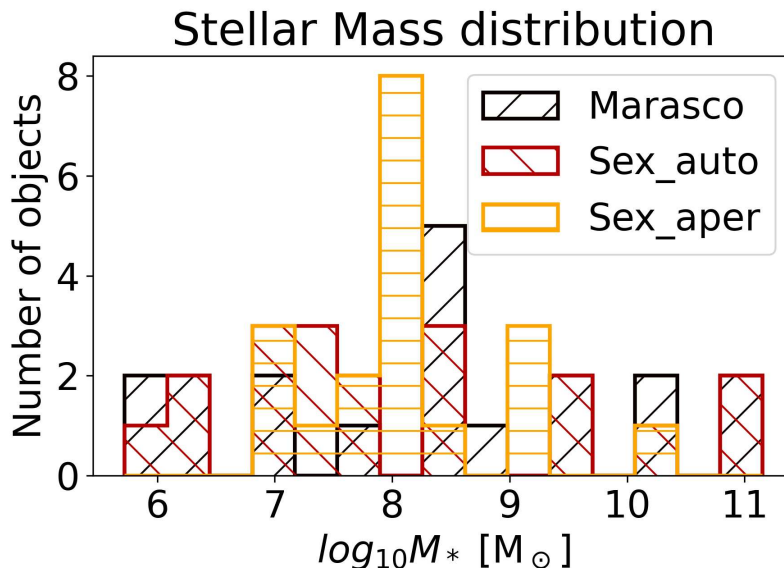
Figure 3.11: Histogram reporting the frequency of a certain range value of M_* in the sample analyzed in this work.

From these histograms, it is possible to notice how the measurements of the `SExtractor` Aperture technique are clearly in disagreement with the others: its distribution tends to be peaked just on one value, resulting in the same parameter estimation for all the objects in our sample.

This behaviour can be appreciated even when looking more carefully at the results through plotting the values from one method against the others, as done in Figure 3.12. Since the redshift is the most significant parameter, it is interesting to look at a complete comparison among all the available results. This monothonic trend shown by the `SExtractor` Aperture method is clearly visible from the distribution of the dark red symbols, which create an almost straight scattered line. The values found by the two other methods, the `SExtractor` Auto and the Marasco tool, in the majority of the cases are in quite good agreement, while in the remaining few a discrepancy is visible.

This tendency is none of a surprise, since already from the fluxes estimations it was evident the large discrepancy with the findings from the Aperture technique, while the two others showed a good agreement. This is reflected also in the physical parameters obtained through the SED fitting analyses.

The closeness with the dotted grey line, which represents the bisector, is an

indicator of the accordance with the Rodighiero's work estimates, since their measurements are plotted as the abscissa axis. A great scatter is visible, with only few points in proximity of the identity line.

Figure 3.12: The most probably value of the redshift estimation from all the methods applied in this work and the results coming from the first release are plotted here, with the legend explaining the symbols.

For the remaining parameters, only the comparison between the Marasco tool results and the values from the paper are reported. This choice is led by the scientific interest in looking at the evolution of these estimates from a first reduction to a statistical investigation conducted on brand new reduced images, where the calibration has been improved. Therefore, among the photometric tools used in this work, the Marasco tool has been chosen to maximize the comparability of the results, given that this tool has been exploited also by Rodighiero and her team.

This comparison can be observed in Figure 3.13 for the A_V parameter, in Figure 3.14 for the SFR and lastly the M_* comparison is reported in Figure 3.15.

Figure 3.13: Comparison between the most probable values of A_V from the Marasco tool analyses (this work) and the first reduction ones.
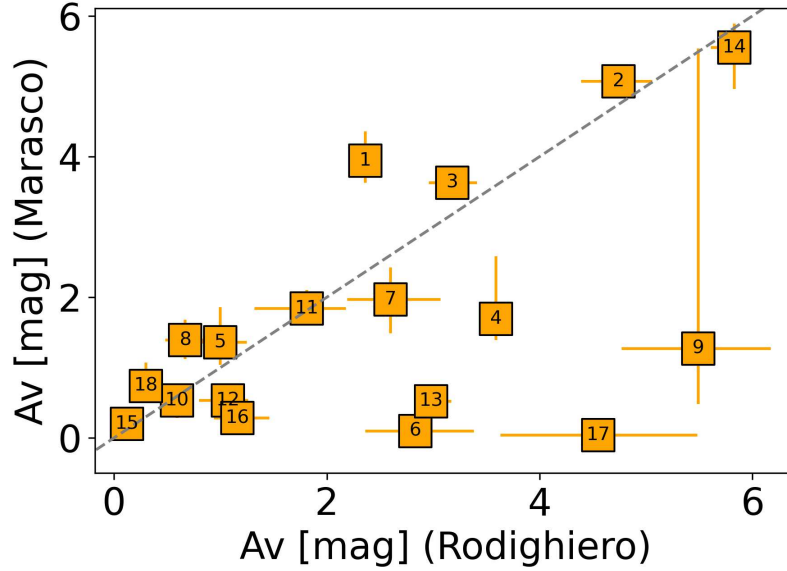

Figure 3.14: Comparison between the most probable values of SFR from the Marasco tool analyses (this work) and the first reduction ones.
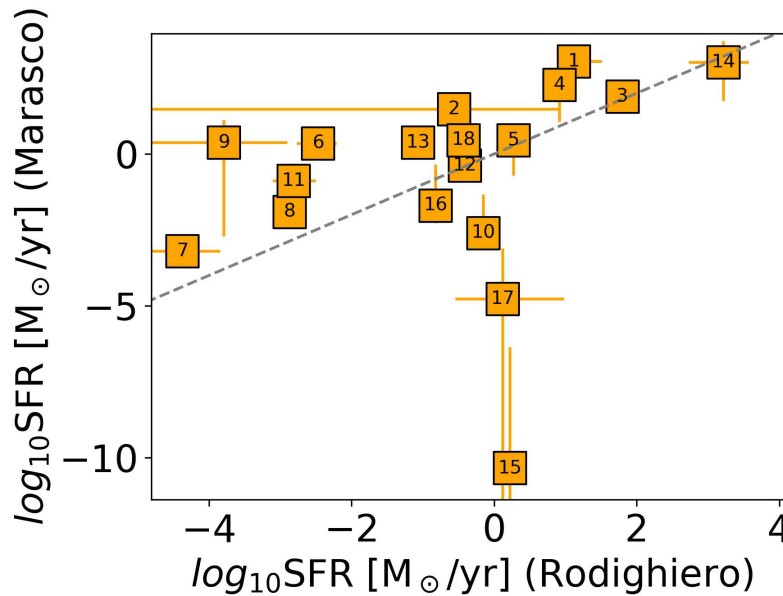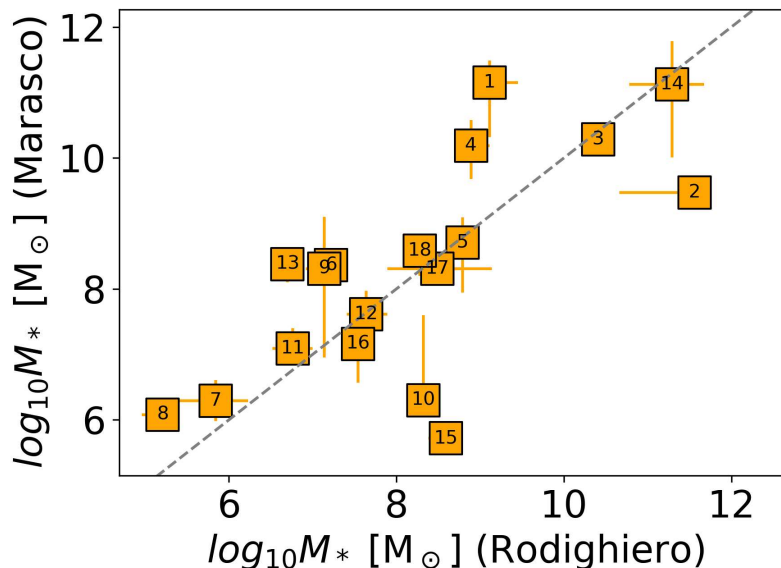
Figure 3.15: Comparison between the most probable values of M_* from the Marasco tool analyses (this work) and the first reduction ones.

The least discrepancy can be observed in the M_* parameter, in which 14 objects present measurements compatible within 3σ (ID = 1, 2, 3, 4, 5, 7, 9, 10, 11, 12, 14, 16, 17, 18) and 10 of them even inside 1σ (ID = 3, 5, 7, 9, 11, 12, 14, 16, 17, 18). The SFR estimates show a comparable agreement, with again 14 values compatible within 3σ (ID = 1, 2, 3, 4, 5, 7, 9, 10, 12, 14, 15, 16, 17, 18) and only one less estimation compatible within 1σ, with 9 objects instead of 10 (ID = 2, 3, 5, 9, 12, 14, 15, 16, 17). Furthermore, the situation is almost the same also for the A_V evaluations, with again the estimations of 14 galaxies showing a concordance within 3σ (ID = 2, 3, 4, 5, 7, 8, 9, 10, 11, 12, 14, 15, 16, 18) and only 8 of them agreeing within 1σ (ID = 2, 5, 7, 9, 10, 11, 14, 15). In conclusion, $\sim 77.8\%$ of this sample's estimations are in 3σ agreement with the values found in the first reduction analysis.

Apart from being whitin the 1σ range in the SFR comparison between the two estimates due to its large error, Hollar (ID = 15) shows a great discrepancy in all the physical parameters retrieved, minus the dust extinction estimation, as visible in the plots (see Fig. 3.14 and Fig. 3.15). Looking at the cutout image of this candidate, a companion is visible, which could be the reason of this result, disturbing the analysis with its emission.

Furthermore, it is worth noticing that the two candidates found at redshift greater than 10 in the first reduction, Pennar (ID = 1) and Kaberlaba (ID = 14),

remain at high redshift also in this new analyses, presenting the most probable value at $z = 10.1$ and $z = 9.7$, respectively. Even the amount of dust extinction remains quite high, moving from the values of 2.36 mag for Pennar and 5.83 mag for Kaberlaba found by Rodighiero et al. [1] to $A_V = 3.94$ mag and $A_V = 5.5$ mag found in this work, thus keeping showing an unexpectedly high dust content.

3.3   Impact on physical properties

This statistical investigation had the purpose of conducting a rigorous analyses, in order to understand if the comparison between physical parameters of galaxies extracted from different softwares and tools are reasonable, or if instead the discrepancy between the methods makes this approach not so useful.

This work hopes to be of some utility in understanding and learning which is in the end the best strategy to study a galaxy. The findings are that for point-like sources the choice does not impact so much on the final estimates, given that this type of objects are the easiest to analyze. Instead, for extended objects, a tool like the Marasco one is preferably. Furthermore, the Aperture technique is a valid choice, but the importance of an adequate radius size choice has been proved with the results of this work.

Moreover, for the situations where a nearby source acts as contaminant disturbing the analyses, as in the case of Klama and companion, the spatially resolved technique is the most suitable choice, given its intrinsic ability of being able of deblending any sources, thus successfully carrying on separate and independent analyses.

An important out-turn of this work is the evidence that, even within the same work group, applying a systematic and accurate analysis, the physical parameters obtained are not always consistent. Therefore, this investigation emphasizes the importance of the analysis method choice, stressing the need of taking this choice into consideration when doing comparisons to take out valuable considerations and results.

To conclude, it is fundamental to stress that the only way to obtain certain confirmations is through spectroscopic follow ups, as claimed by the majority of the scientific papers published in this field of research.

3.4 Future work

This investigation has made the effort of focusing on different photometric techniques available to conduct a photometric evaluation of the sources. However, the goal is to extend this inspection to also include the study of the effect of various SED fitting softwares choices. The offer in this sense is quite large, with not only the `Bagpipes` code to exploit, but other codes such as `EAZY` [95], `prospector` [96] and `CIGALE` [97], just to cite some of them.

Each one consists of different technical details, such as the possibility to provide an input range for the parameters, allowing the user to personalize the analyses, or being completely autonomous in the evaluation of their values, only basing the analyses on already built-in distributions. Furthermore, the difference stays also in the output parameters generated, since some of these softwares just provide a redshift estimation, while others are able to cover all the most important physical parameters in a galaxy. Therefore, based on the kind of analyses that one wants to conduct, also this choice becomes really fundamental and thus studying its effect is of notably importance.

The deepening of this investigation also depends on the enrichment of the sample: here the analyses has been carried out only on 20 objects, a quite small sample; thus, the future plan should focus on applying this systematic investigation on complete samples obtained from fields images available through the JWST observations.

3.4.1 Future paper on Klama

A paper reporting the peculiarities and the results regarding the spatially resolved SED fitting analysis of the Klama system is in preparation.

This paper will be focused on addressing the impact of merging processes in the stellar mass build up of the most massive dust obscured sources at $z > 3$. Since the interest concerns the identification of potential mergers among optically dark sources, it is very relevant to understand if the two objects belonging to the this system (the galaxies identified in this thesis by ID = 2 and 19) present in the small field of view are physically associated or if they simply sit along the same line of sight. The system is visible in Fig. 3.16, where also the arched structure is included. Therefore, an in depth investigation of the morphological and spatially resolved photometric properties of Klama and of its local environment is going to be conducted.

Figure 3.16: *Left panel.* RGB image of the Klama system combining F200W, F277W and F444W filters. *Central panel.* Redshift Probability Distribution Function, PDF(z), for the brightest pixel (in the F444W band) in each of the three main components A, B and C. *Right panel.* F356W highly contrasted image of the same region shown in the left panel.
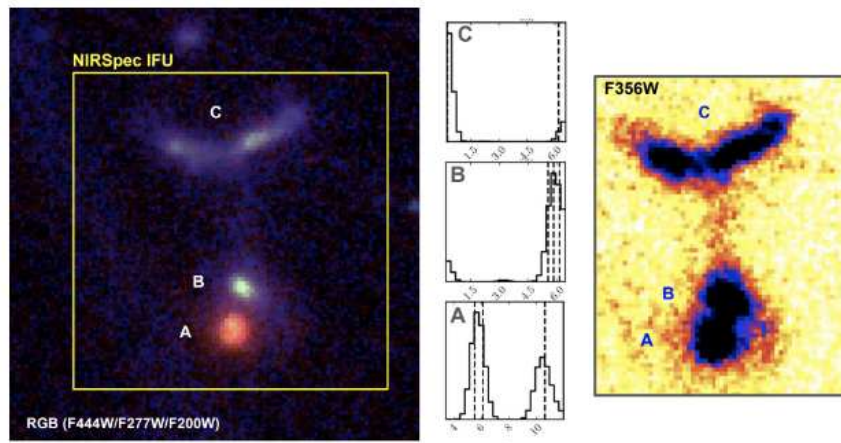
In the left panel, the NIRCam color map of the Klama system combining F200W, F277W and F444W filters (RGB image) shows all its three main components: Klama (in this thesis: ID = 2), which is the reddest object in the bottom part of the field (A component), its bluer close companion (in this thesis: ID = 19, B component) and the elongated structure in the upper part of the map (C component). While the blue colors of B and C might naturally indicate a different redshift as compared to the red A source, this paper will provide evidences for a physical connection among the three components. For reference, the yellow square marks the field of view of NIRSpec IFU (3" × 3"). The same field of view is presented in the right panel, but this time through a F356W highly contrasted image. Interestingly, a diffuse emission clearly rises as a bridge connecting the main system (A+B) to the queue (C).

Chapter 4

Summary and Conclusions

This thesis provides in Chapter 1 a precise description of the space telescope *James Webb*, presenting its capabilities and its instrumentation, including an accurate overview of the results coming from its observations, underling the possible tension with the actual standard ΛCDM cosmological model, of which a brief explanation of the formalism behind it has been discussed, along with the presentation of studies in which this tension is not found at all, or possible explanations are suggested, such as the concept of "Feedbak-Free starbursts" [64], expulsion of dust during the earliest phases of galaxy formation [65] or a top-heavy IMF [19].

Given the discrepancy between these results, assessing the reliability of the physical properties inferred from the observations of these high redshift galaxies is a crucial step. Therefore, this need has guided the choice for conducting a complete statistical investigation to understand the impact of different photometric extractions on these parameters estimation.

In Chapter 2, the softwares exploited in this work are presented, describing their functionalities, including `SExtractor` and the Marasco tool for the photometric reduction in addition to the `Bagpipes` code, used instead to infer the physical parameters through the SED fitting analyses. The details of how this sample was selected in the work done by Rodighiero et al. [1] are presented, along with the procedure of how this analyses has been conducted.

Its execution can be briefly summarized in the following points:

- the first step was to start with a trial run of the software `SExtractor` to be sure that the set up was working properly;

- secondly, the newly reduced images have been retrieved and a photometric

catalogue has been built through the `SExtractor` double image mode, allowing to fix the positions of the detections found in the deepest band available, F444W, even when processing the other bands;

- the catalogue obtained in this way has been crossmatched using the `TOPCAT` tool with the sample previously built by Rodighiero and her team;

- for this 18 galaxies the flux measurements conducted by `SExtractor` have been retrieved, both the ones already containing the total estimated emission and the ones in which the Aperture technique has been applied, with an aperture size chosen to be $\approx 0.1''$;

- the cutouts for each one of these sources have been built to be able to apply the Marasco tool, in order to gain an additional flux estimation from a third method;

- the fluxes coming from a technique using an aperture (all of the above, except for the `SExtractor` Auto) need to be corrected, applying the right factor to account for the source's emission placed outside the aperture. This step has been done exploiting the correction factors related to each band for the NIRCam instrument;

- these fluxes values retrieved by three different procedures have been submitted to the `Bagpipes` code, together with the input parameters ranges that have been evaluated to be the most suitable choice in this analyses, being able to obtain the most probable value of the physical parameters describing these sources;

- a separate strategy has been applied for the object 2, Klama, due to the presence of a nearby companion disturbing the analyses. Different settings have been used to be able to properly deblend the two sources, resulting in the inclusion of this companion in the sample (ID 19).

In Chapter 3 the results acquired through this procedure have been shown and commented. The most important conclusions can be summarize as:

- the choice of the radius size can really affect the goodness of the results. In the case here presented, the choice made in the `SExtractor` Aperture method was too small, resulting in a underestimation of the total emission, even after applying the correction factor, which is not enough to properly account for all the emission lost. This bad estimation of the fluxes was reflected in the physical parameters obtained through the SED fitting procedure, resulting in almost the same values for all the objects in the sample. This outcome does not mean

that the idea of the aperture analyses is not valid, as proven by the good results obtained by the Marasco tool, but as mentioned above, that the aperture choice is an important factor to consider;

- unfortunately, the most significant parameter, z, is the one presenting the least concordance between the results retrieved in this work from the two other techniques, `SExtractor` Auto and the Marasco tool, and the estimation obtained through the previous release. In fact, it shows a great dispersion when plotting the values one against each other. The other physical parameters show a better agreement, meaning that they are less sensitive to redshift variations (in particular the stellar mass), unless very discrepant redshifts values are present. In fact, the sources showing the biggest discrepancies in the redshift estimation ($ID = 9, 15, 17$) are also the ones presenting the less agreement in the other physical quantities;

- some discrepancies are already present between the same images analyzed by the same SED fitting technique, just changing the photometric analyses and the reduction effectuated on the images. This led to think that the comparison between the results from different groups, using all different tools and carrying on the procedure in slightly different ways, should be taken with a grain of salt.

In conclusion, the main outcome of this investigation is that spectroscopic confirmation is the only way to surely acquire informations about the nature of these galaxies, confirming the reason of the already high demand for spectroscopic follow ups, especially with JWST.

Acknowledgments

Thank people here.

References

[1] Giulia Rodighiero, Laura Bisigello, Edoardo Iani, Antonino Marasco, Andrea Grazian, Francesco Sinigaglia, Paolo Cassata, and Carlotta Gruppioni. Jwst unveils heavily obscured (active and passive) sources up to $z \sim 13$. *Monthly Notices of the Royal Astronomical Society: Letters*, 518(1):L19–L24, 2023.

[2] A Marasco, F Belfiore, G Cresci, F Lelli, G Venturi, LK Hunt, A Concas, A Marconi, F Mannucci, M Mingozzi, et al. Shaken, not blown: the gentle baryonic feedback of nearby starburst dwarf galaxies. *arXiv e-prints*, pages arXiv–2209, 2022.

[3] Brant E Robertson. Galaxy formation and reionization: key unknowns and expected breakthroughs by the james webb space telescope. *Annual Review of Astronomy and Astrophysics*, 60:121–158, 2022.

[4] Katherine E Whitaker, Alexandra Pope, Ryan Cybulski, Caitlin M Casey, Gergö Popping, and Min S Yun. The constant average relationship between dust-obscured star formation and stellar mass from $z = 0$ to $z = 2.5$. *The Astrophysical Journal*, 850(2):208, 2017.

[5] T Wang, D Elbaz, C Schreiber, M Pannella, X Shu, SP Willner, MLN Ashby, J-S Huang, Adriano Fontana, A Dekel, et al. Infrared color selection of massive galaxies at $z > 3$. *The Astrophysical Journal*, 816(2):84, 2016.

[6] P Jakobsen, P Ferruit, C Alves de Oliveira, S Arribas, G Bagnasco, R Barho, TL Beck, S Birkmann, T Böker, AJ Bunker, et al. The near-infrared spectrograph (nirspec) on the james webb space telescope-i. overview of the instrument and its capabilities. *Astronomy & Astrophysics*, 661:A80, 2022.

[7] Marcia J Rieke, Douglas M Kelly, and Scott D Horner. Overview of james webb space telescope and nircam's role. In *Cryogenic Optical Systems and Instruments XI*, volume 5904, page 590401. SPIE, 2005.

REFERENCES

[8] Jonathan P Gardner, John C Mather, Mark Clampin, Rene Doyon, Matthew A Greenhouse, Heidi B Hammel, John B Hutchings, Peter Jakobsen, Simon J Lilly, Knox S Long, et al. The james webb space telescope. *Space Science Reviews*, 123:485–606, 2006.

[9] Jonathan P Gardner, John C Mather, Mark Clampin, Rene Doyon, Kathryn A Flanagan, Marijn Franx, Matthew A Greenhouse, Heidi B Hammel, John B Hutchings, Peter Jakobsen, et al. The james webb space telescope. In *Astrophysics in the Next Decade: The James Webb Space Telescope and Concurrent Facilities*, pages 1–29. Springer, 2009.

[10] Phillip A Sabelhaus and John E Decker. An overview of the james webb space telescope (jwst) project. *Optical, Infrared, and Millimeter Space Telescopes*, 5487:550–563, 2004.

[11] Michael W McElwain, Lee D Feinberg, Marshall D Perrin, Mark Clampin, C Matt Mountain, Matthew D Lallo, Charles-Philippe Lajoie, Randy A Kimble, Charles W Bowers, Christopher C Stark, et al. The james webb space telescope mission: Optical telescope element design, development, and performance. *Publications of the Astronomical Society of the Pacific*, 135(1047):058001, 2023.

[12] Jane Rigby, Marshall Perrin, Michael McElwain, Randy Kimble, Scott Friedman, Matt Lallo, René Doyon, Lee Feinberg, Pierre Ferruit, Alistair Glasse, et al. The science performance of jwst as characterized in commissioning. *Publications of the Astronomical Society of the Pacific*, 135(1046):048001, 2023.

[13] Jason Kalirai. Scientific discovery with the james webb space telescope. *Contemporary Physics*, 59(3):251–290, 2018.

[14] Gillian S Wright, George H Rieke, Luis Colina, Ewine van Dishoeck, Greg Goodson, Tom Greene, Pierre-Olivier Lagage, Avinash Karnik, Scott D Lambros, Dietrich Lemke, et al. The jwst miri instrument concept. In *Optical, Infrared, and Millimeter Space Telescopes*, volume 5487, pages 653–663. SPIE, 2004.

[15] Scott D Horner and Marcia J Rieke. The near-infrared camera (nircam) for the james webb space telescope (jwst). In *Optical, Infrared, and Millimeter Space Telescopes*, volume 5487, pages 628–634. SPIE, 2004.

[16] René Doyon, John B Hutchings, Mathilde Beaulieu, Loic Albert, David Lafrenière, Chris Willott, Driss Touahri, Neil Rowlands, Micheal Maszkiewicz, Alex W Fullerton, et al. The jwst fine guidance sensor (fgs) and near-infrared imager and slitless spectrograph (niriss). In *Space telescopes and instrumentation*

REFERENCES

2012: Optical, infrared, and millimeter wave, volume 8442, pages 1005–1017. SPIE, 2012.

[17] Winfried Posselt, Wolfgang Holota, Ernst Kulinyak, Guenther Kling, Thomas Kutscheid, Olivier Le Fevre, Eric Prieto, and Pierre Ferruit. Nirspec: near-infrared spectrograph for the jwst. In *Optical, Infrared, and Millimeter Space Telescopes*, volume 5487, pages 688–697. SPIE, 2004.

[18] Alistair Glasse, GH Rieke, Eva Bauwens, Macarena García-Marín, ME Ressler, Steffen Rost, Tuomo Ville Tikkanen, Bart Vandenbussche, and GS Wright. The mid-infrared instrument for the james webb space telescope, ix: predicted sensitivity. *Publications of the Astronomical Society of the Pacific*, 127(953):686, 2015.

[19] Steven L Finkelstein, Micaela B Bagley, Henry C Ferguson, Stephen M Wilkins, Jeyhan S Kartaltepe, Casey Papovich, LY Aaron Yung, Pablo Arrabal Haro, Peter Behroozi, Mark Dickinson, et al. Ceers key paper. i. an early look into the first 500 myr of galaxy formation with jwst. *The Astrophysical Journal Letters*, 946(1):L13, 2023.

[20] NJ Adams, CJ Conselice, L Ferreira, D Austin, JAA Trussler, I Juodžbalis, SM Wilkins, J Caruana, P Dayal, A Verma, et al. Discovery and properties of ultra-high redshift galaxies ($9 < z < 12$) in the jwst ero smacs 0723 field. *Monthly Notices of the Royal Astronomical Society*, 518(3):4755–4766, 2023.

[21] Marco Castellano, Adriano Fontana, Tommaso Treu, Paola Santini, Emiliano Merlin, Nicha Leethochawalit, Michele Trenti, Eros Vanzella, Uros Mestric, Andrea Bonchi, et al. Early results from glass-jwst. iii. galaxy candidates at $z \sim 9 - 15$. *The Astrophysical Journal Letters*, 938(2):L15, 2022.

[22] Ivo Labbé, Pieter van Dokkum, Erica Nelson, Rachel Bezanson, Katherine A Suess, Joel Leja, Gabriel Brammer, Katherine Whitaker, Elijah Mathews, Mauro Stefanon, et al. A population of red candidate massive galaxies ~ 600 myr after the big bang. *Nature*, 616(7956):266–269, 2023.

[23] Rohan P Naidu, Pascal A Oesch, David J Setton, Jorryt Matthee, Charlie Conroy, Benjamin D Johnson, John R Weaver, Rychard J Bouwens, Gabriel B Brammer, Pratika Dayal, et al. Schrodinger's galaxy candidate: Puzzlingly luminous at $z \approx 17$, or dusty/quenched at $z \approx 5$? *arXiv preprint arXiv:2208.02794*, 2022.

[24] CT Donnan, DJ McLeod, JS Dunlop, RJ McLure, AC Carnall, R Begley, F Cullen, ML Hamadouche, RAA Bowler, D Magee, et al. The evolution of

REFERENCES

the galaxy uv luminosity function at redshifts $z \simeq 8 - 15$ from deep jwst and ground-based near-infrared imaging. *Monthly Notices of the Royal Astronomical Society*, 518(4):6011–6040, 2023.

[25] Yuichi Harikane, Kimihiko Nakajima, Masami Ouchi, Hiroya Umeda, Yuki Isobe, Yoshiaki Ono, Yi Xu, and Yechi Zhang. Pure spectroscopic constraints on uv luminosity functions and cosmic star formation history from 25 galaxies at $z_{spec} = 8.61 - 13.20$ confirmed with jwst/nirspec. *arXiv preprint arXiv:2304.06658*, 2023.

[26] LD Bradley, A Zitrin, D Coe, R Bouwens, M Postman, I Balestra, C Grillo, A Monna, P Rosati, S Seitz, et al. Clash: A census of magnified star-forming galaxies at $z \sim 6 - 8$. *The Astrophysical Journal*, 792(1):76, 2014.

[27] Rychard J Bouwens, GD Illingworth, PA Oesch, M Trenti, I Labbé, L Bradley, M Carollo, PG Van Dokkum, V Gonzalez, B Holwerda, et al. Uv luminosity functions at redshifts $z \sim 4$ to $z \sim 10$: 10,000 galaxies from hst legacy fields. *The Astrophysical Journal*, 803(1):34, 2015.

[28] DJ McLeod, RJ McLure, and JS Dunlop. The $z = 9 - 10$ galaxy population in the hubble frontier fields and clash surveys: the $z = 9$ luminosity function and further evidence for a smooth decline in ultraviolet luminosity density at $z \geq 8$. *Monthly Notices of the Royal Astronomical Society*, 459(4):3812–3824, 2016.

[29] Masafumi Ishigaki, Ryota Kawamata, Masami Ouchi, Masamune Oguri, Kazuhiro Shimasaku, and Yoshiaki Ono. Full-data results of hubble frontier fields: Uv luminosity functions at $z \sim 6 - 10$ and a consistent picture of cosmic reionization. *The Astrophysical Journal*, 854(1):73, 2018.

[30] PA Oesch, RJ Bouwens, GD Illingworth, I Labbé, and M Stefanon. The dearth of $z \sim 10$ galaxies in all hst legacy fields-the rapid evolution of the galaxy population in the first 500 myr. *The Astrophysical Journal*, 855(2):105, 2018.

[31] P Ade Planck Collaboration, N Aghanim, M Alves, M Arnaud, D Arzoumanian, J Aumont, C Baccigalupi, J Banday, R Barreiro, et al. Planck intermediate results. xxxiii. signature of the magnetic field geometry of interstellar filaments in dust polarization maps. *A&A*, 586:A136, 2016.

[32] Judd D Bowman, Alan EE Rogers, Raul A Monsalve, Thomas J Mozdzen, and Nivedita Mahesh. An absorption profile centred at 78 megahertz in the sky-averaged spectrum. *Nature*, 555(7694):67–70, 2018.

[33] Andrea Pallottini and Andrea Ferrara. Stochastic star formation in early galaxies: Implications for the james webb space telescope. *Astronomy & Astrophysics*, 677:L4, 2023.

REFERENCES

[34] Klaus M Pontoppidan, Jaclyn Barrientes, Claire Blome, Hannah Braun, Matthew Brown, Margaret Carruthers, Dan Coe, Joseph DePasquale, Néstor Espinoza, Macarena Garcia Marin, et al. The jwst early release observations. *The Astrophysical Journal Letters*, 936(1):L14, 2022.

[35] Haojing Yan, Zhiyuan Ma, Chenxiaoji Ling, Cheng Cheng, and Jia-Sheng Huang. First batch of $z \approx 11 - 20$ candidate objects revealed by the james webb space telescope early release observations on smacs 0723-73. *The Astrophysical Journal Letters*, 942(1):L9, 2022.

[36] Dan Coe, Brett Salmon, Maruša Bradač, Larry D Bradley, Keren Sharon, Adi Zitrin, Ana Acebron, Catherine Cerny, Nathália Cibirka, Victoria Strait, et al. Relics: reionization lensing cluster survey. *The Astrophysical Journal*, 884(1):85, 2019.

[37] Hakim Atek, Marko Shuntov, Lukas J Furtak, Johan Richard, Jean-Paul Kneib, Guillaume Mahler, Adi Zitrin, HJ McCracken, Stéphane Charlot, Jacopo Chevallard, et al. Revealing galaxy candidates out to $z \sim 16$ with jwst observations of the lensing cluster smacs0723. *Monthly Notices of the Royal Astronomical Society*, 519(1):1201–1220, 2023.

[38] Larry D Bradley, Dan Coe, Gabriel Brammer, Lukas J Furtak, Rebecca L Larson, Felipe Andrade-Santos, Rachana Bhatawdekar, Marusa Bradac, Tom Broadhurst, Adam Carnall, et al. High-redshift galaxy candidates at $z = 9 - 13$ as revealed by jwst observations of whl0137-08. *arXiv preprint arXiv:2210.01777*, 2022.

[39] Sandro Tacchella, Daniel J Eisenstein, Kevin Hainline, Benjamin D Johnson, William M Baker, Jakob M Helton, Brant Robertson, Katherine A Suess, Zuyi Chen, Erica Nelson, et al. Jades imaging of gn-z11: Revealing the morphology and environment of a luminous galaxy 430 myr after the big bang. *arXiv preprint arXiv:2302.07234*, 2023.

[40] Christina C Williams, Sandro Tacchella, Michael V Maseda, Brant E Robertson, Benjamin D Johnson, Chris J Willott, Daniel J Eisenstein, Christopher NA Willmer, Zhiyuan Ji, Kevin N Hainline, et al. Jems: A deep medium-band imaging survey in the hubble ultra-deep field with jwst nircam & niriss. *arXiv preprint arXiv:2301.09780*, 2023.

[41] Francesco Ziparo, Andrea Ferrara, Laura Sommovigo, and Mahsa Kohandel. Blue monsters. why are jwst super-early, massive galaxies so blue? *Monthly Notices of the Royal Astronomical Society*, 520(2):2445–2450, 2023.

REFERENCES

[42] Rychard J Bouwens, Mauro Stefanon, Gabriel Brammer, Pascal A Oesch, Thomas Herard-Demanche, Garth D Illingworth, Jorryt Matthee, Rohan P Naidu, Pieter G van Dokkum, and Ivana F van Leeuwen. Evolution of the uv lf from $z \sim 15$ to $z \sim 8$ using new jwst nircam medium-band observations over the hudf/xdf. *Monthly Notices of the Royal Astronomical Society*, 523(1):1036–1055, 2023.

[43] Caitlin M Casey, Hollis B Akins, Marko Shuntov, Olivier Ilbert, Louise Paque-reau, Maximilien Franco, Christopher C Hayward, Steven L Finkelstein, Michael Boylan-Kolchin, Brant E Robertson, et al. Cosmos-web: Intrinsically lumi-nous $z \gtrsim 10$ galaxy candidates test early stellar mass assembly. *arXiv preprint arXiv:2308.10932*, 2023.

[44] Maximilien Franco, Hollis B Akins, Caitlin M Casey, Steven L Finkelstein, Marko Shuntov, Katherine Chworowsky, Andreas L Faisst, Seiji Fujimoto, Olivier Ilbert, Anton M Koekemoer, et al. Unveiling the distant universe: Characterizing $z \geqslant 9$ galaxies in the first epoch of cosmos-web. *arXiv preprint arXiv:2308.00751*, 2023.

[45] T Treu, G Roberts-Borsani, M Bradac, G Brammer, Adriano Fontana, A Henry, C Mason, T Morishita, Laura Pentericci, X Wang, et al. The glass-jwst early release science program. i. survey design and release plans. *The Astrophysical Journal*, 935(2):110, 2022.

[46] Haojing Yan, Lifan Wang, Zhiyuan Ma, and Lei Hu. Pointlike sources among $z > 11$ galaxy candidates: Contaminants due to supernovae at high redshifts? *The Astrophysical Journal Letters*, 947(1):L1, 2023.

[47] Dale D Kocevski, Guillermo Barro, Elizabeth J McGrath, Steven L Finkelstein, Micaela B Bagley, Henry C Ferguson, Shardha Jogee, Guang Yang, Mark Dick-inson, Nimish P Hathi, et al. Ceers key paper. ii. a first look at the resolved host properties of agn at $3 < z < 5$ with jwst. *The Astrophysical Journal Letters*, 946(1):L14, 2023.

[48] Rebecca L Larson, Steven L Finkelstein, Dale D Kocevski, Taylor A Hutchison, Jonathan R Trump, Pablo Arrabal Haro, Volker Bromm, Nikko J Cleri, Mark Dickinson, Seiji Fujimoto, et al. A ceers discovery of an accreting supermassive black hole 570 myr after the big bang: Identifying a progenitor of massive $z > 6$ quasars. *The Astrophysical Journal Letters*, 953(2):L29, 2023.

[49] Jan Scholtz, Callum Witten, Nicolas Laporte, Hannah Ubler, Michele Perna, Roberto Maiolino, Santiago Arribas, William Baker, Jake Bennett, Francesco D'Eugenio, et al. Gn-z11: The environment of an agn at $z = 10.603$. *arXiv preprint arXiv:2306.09142*, 2023.

REFERENCES

[50] Piero Madau and Mark Dickinson. Cosmic star-formation history. *Annual Review of Astronomy and Astrophysics*, 52:415–486, 2014.

[51] Andrea Enia, Margherita Talia, Francesca Pozzi, Andrea Cimatti, Ivan Delvecchio, Gianni Zamorani, Quirino D'Amato, Laura Bisigello, Carlotta Gruppioni, Giulia Rodighiero, et al. A new estimate of the cosmic star formation density from a radio-selected sample, and the contribution of h-dark galaxies at $z \geq 3$. *The Astrophysical Journal*, 927(2):204, 2022.

[52] Jorge A Zavala, Véronique Buat, Caitlin M Casey, Steven L Finkelstein, Denis Burgarella, Micaela B Bagley, Laure Ciesla, Emanuele Daddi, Mark Dickinson, Henry C Ferguson, et al. Dusty starbursts masquerading as ultra-high redshift galaxies in jwst ceers observations. *The Astrophysical journal letters*, 943(2):L9, 2023.

[53] RJ McLure, JS Dunlop, F Cullen, N Bourne, PN Best, S Khochfar, RAA Bowler, AD Biggs, JE Geach, D Scott, et al. Dust attenuation in $2 < z < 3$ star-forming galaxies from deep alma observations of the hubble ultra deep field. *Monthly Notices of the Royal Astronomical Society*, 476(3):3991–4006, 2018.

[54] L Bisigello, G Gandolfi, A Grazian, G Rodighiero, L Costantin, AR Cooray, A Feltre, C Gruppioni, NP Hathi, BW Holwerda, et al. Delving deep: a population of extremely dusty dwarfs observed by jwst. *arXiv preprint arXiv:2302.12270*, 2023.

[55] Richard G Bower. The evolution of groups of galaxies in the press–schechter formalism. *Monthly Notices of the Royal Astronomical Society*, 248(2):332–352, 1991.

[56] William H Press and Paul Schechter. Formation of galaxies and clusters of galaxies by self-similar gravitational condensation. *Astrophysical Journal, Vol. 187, pp. 425-438 (1974)*, 187:425–438, 1974.

[57] Pierluigi Monaco. Dynamics in the cosmological mass function (or, why does the press & schechter work?). *arXiv preprint astro-ph/9811085*, 1998.

[58] Marc Davis, George Efstathiou, Carlos S Frenk, and Simon DM White. The evolution of large-scale structure in a universe dominated by cold dark matter. *Astrophysical Journal, Part 1 (ISSN 0004-637X), vol. 292, May 15, 1985, p. 371-394. Research supported by the Science and Engineering Research Council of England and NASA.*, 292:371–394, 1985.

REFERENCES

[59] JR Bond, Shaun Cole, George Efstathiou, and Nick Kaiser. Excursion set mass functions for hierarchical gaussian fluctuations. *Astrophysical Journal, Part 1 (ISSN 0004-637X), vol. 379, Oct. 1, 1991, p. 440-460. Research supported by NSERC, NASA, and University of California.*, 379:440–460, 1991.

[60] Ravi K Sheth and Giuseppe Tormen. Large-scale bias and the peak background split. *Monthly Notices of the Royal Astronomical Society*, 308(1):119–126, 1999.

[61] Cedric Lacey and Shaun Cole. Merger rates in hierarchical models of galaxy formation. *Monthly Notices of the Royal Astronomical Society*, 262(3):627–649, 1993.

[62] Scott Dodelson and Fabian Schmidt. *Modern cosmology.* Academic press, 2020.

[63] Fergus Cullen, RJ McLure, DJ McLeod, JS Dunlop, CT Donnan, AC Carnall, RAA Bowler, R Begley, ML Hamadouche, and TM Stanton. The ultraviolet continuum slopes (β) of galaxies at $z \simeq 8 - 16$ from jwst and ground-based near-infrared imaging. *Monthly Notices of the Royal Astronomical Society*, 520(1):14–23, 2023.

[64] Avishai Dekel, Kartick C Sarkar, Yuval Birnboim, Nir Mandelker, and Zhaozhou Li. Efficient formation of massive galaxies at cosmic dawn by feedback-free starbursts. *Monthly Notices of the Royal Astronomical Society*, 523(3):3201–3218, 2023.

[65] Andrea Ferrara, Andrea Pallottini, and Pratika Dayal. On the stunning abundance of super-early, luminous galaxies revealed by jwst. *Monthly Notices of the Royal Astronomical Society*, 522(3):3986–3991, 2023.

[66] Tiger Yu-Yang Hsiao, Dan Coe, Lily Whitler, Intae Jung, Gourav Khullar, Ashish Kumar Meena, Pratika Dayal, Kirk SS Barrow, Lillian Santos-Olmsted, Adam Casselman, et al. Jwst reveals a possible $z \sim 11$ galaxy merger in triply lensed macs0647–jd. *The Astrophysical Journal Letters*, 949(2):L34, 2023.

[67] Charlotte A Mason, Michele Trenti, and Tommaso Treu. The brightest galaxies at cosmic dawn. *Monthly Notices of the Royal Astronomical Society*, 521(1):497–503, 2023.

[68] Julian B Muñoz, Jordan Mirocha, Steven Furlanetto, and Nashwan Sabti. Breaking degeneracies in the first galaxies with clustering. *arXiv preprint arXiv:2306.09403*, 2023.

REFERENCES

[69] Guochao Sun, Claude-André Faucher-Giguère, Christopher C Hayward, Xuejian Shen, Andrew Wetzel, and Rachel K Cochrane. Bursty star formation naturally explains the abundance of bright galaxies at cosmic dawn. *The Astrophysical Journal Letters*, 955(2):L35, 2023.

[70] Marijn Franx, Garth D Illingworth, Daniel D Kelson, Pieter G van Dokkum, and Kim-Vy Tran. A pair of lensed galaxies at $z = 4.92$ in the field of cl 1358+ 62. *The Astrophysical Journal*, 486(2):L75, 1997.

[71] Larry D Bradley, RJ Bouwens, HC Ford, GD Illingworth, MJ Jee, N Benítez, TJ Broadhurst, M Franx, BL Frye, L Infante, et al. Discovery of a very bright strongly lensed galaxy candidate at $z \approx 7.6$. *The Astrophysical Journal*, 678(2):647, 2008.

[72] Marc Postman, Dan Coe, Narciso Benitez, Larry Bradley, Tom Broadhurst, Megan Donahue, Holland Ford, Or Graur, Genevieve Graves, Stephanie Jouvel, et al. The cluster lensing and supernova survey with hubble: an overview. *The Astrophysical Journal Supplement Series*, 199(2):25, 2012.

[73] Dan Coe, Larry Bradley, and Adi Zitrin. Frontier fields: High-redshift predictions and early results. *The Astrophysical Journal*, 800(2):84, 2015.

[74] Brett Salmon, Dan Coe, Larry Bradley, Rychard Bouwens, Marusa Bradač, Kuang-Han Huang, Pascal A Oesch, Daniel Stark, Keren Sharon, Michele Trenti, et al. Relics: The reionization lensing cluster survey and the brightest high-z galaxies. *The Astrophysical Journal*, 889(2):189, 2020.

[75] C Steidel, Max Pettini, and Donald Hamilton. Lyman limit imaging of high redshift galaxies. iii. new observations of 4 qso fields. *arXiv preprint astro-ph/9509089*, 1995.

[76] AC Carnall. Galaxy physical parameters from spectroscopy with bagpipes. *The Art of Measuring Galaxy Physical Properties*, page 44, 2019.

[77] GS Da Costa. Basic photometry techniques. In *Astronomical CCD Observing and Reduction Techniques*, volume 23, page 90, 1992.

[78] Emmanuel Bertin and Stephane Arnouts. Sextractor: Software for source extraction. *Astronomy and astrophysics supplement series*, 117(2):393–404, 1996.

[79] Francesco Valentino, Gabriel Brammer, Katriona ML Gould, Vasily Kokorev, Seiji Fujimoto, Christian Kragh Jespersen, Aswin P Vijayan, John R Weaver, Kei Ito, Masayuki Tanaka, et al. An atlas of color-selected quiescent galaxies at $z > 3$ in public jwst fields. *The Astrophysical Journal*, 947(1):20, 2023.

REFERENCES

[80] Mark B Taylor. Topcat & stil: Starlink table/votable processing software. In *Astronomical data analysis software and systems XIV*, volume 347, page 29, 2005.

[81] E Merlin, N Bourne, M Castellano, HC Ferguson, T Wang, S Derriere, JS Dunlop, D Elbaz, and A Fontana. T-phot version 2.0: Improved algorithms for background subtraction, local convolution, kernel registration, and new options. *Astronomy & Astrophysics*, 595:A97, 2016.

[82] Victoria G Laidler, Casey Papovich, Norman A Grogin, Rafal Idzi, Mark Dickinson, Henry C Ferguson, Bryan Hilbert, Kelsey Clubb, and Swara Ravindranath. Tfit: A photometry package using prior information for mixed-resolution data sets. *Publications of the Astronomical Society of the Pacific*, 119(861):1325, 2007.

[83] C De Santis, A Grazian, A Fontana, and P Santini. Convphot: A profile-matching algorithm for precision photometry. *New Astronomy*, 12(4):271–288, 2007.

[84] Chien Y Peng, Luis C Ho, Chris D Impey, and Hans-Walter Rix. Detailed decomposition of galaxy images. ii. beyond axisymmetric models. *The Astronomical Journal*, 139(6):2097, 2010.

[85] Russ R Laher, Varoujan Gorjian, Luisa M Rebull, Frank J Masci, John W Fowler, George Helou, Shrinivas R Kulkarni, and Nicholas M Law. Aperture photometry tool. *Publications of the Astronomical Society of the Pacific*, 124(917):737, 2012.

[86] Yen-Ting Lin, Po-Feng Wu, Masayuki Akiyama, et al. Introducing pixedfit: A spectral energy distribution fitting code designed for resolved sources. *The Astrophysical Journal Supplement Series*, 254(1):15, 2021.

[87] Dan Coe, Intae Jung, Henry C Ferguson, Gabriel Brammer, Kartheik G Iyer, Larry D Bradley, Pratika Dayal, Rogier A Windhorst, Adi Zitrin, Ashish Kumar Meena, et al. Spatially resolved stellar populations of 0.3¡ z¡ 6.0 galaxies in whl 0137–08 and macs 0647+ 70 clusters as revealed by jwst: How do galaxies grow and quench over cosmic time? *The Astrophysical Journal*, 945(2):117, 2023.

[88] Pablo G Pérez-González, Guillermo Barro, Marianna Annunziatella, Luca Costantin, Ángela García-Argumánez, Elizabeth J McGrath, Rosa M Mérida, Jorge A Zavala, Pablo Arrabal Haro, Micaela B Bagley, et al. Ceers key paper. iv. a triality in the nature of hst-dark galaxies. *The Astrophysical Journal Letters*, 946(1):L16, 2023.

[89] Ángela García-Argumánez, Pablo G Pérez-González, Armando Gil de Paz, Gregory F Snyder, Pablo Arrabal Haro, Micaela B Bagley, Steven L Finkelstein,

Jeyhan S Kartaltepe, Anton Koekemoer, Casey Papovich, et al. Probing the earliest phases in the formation of massive galaxies with simulated hst+ jwst imaging data from illustris. *The Astrophysical Journal*, 944(1):3, 2023.

[90] Gustavo Bruzual and Stephane Charlot. Stellar population synthesis at the resolution of 2003. *Monthly Notices of the Royal Astronomical Society*, 344(4):1000–1028, 2003.

[91] Daniela Calzetti, Lee Armus, Ralph C Bohlin, Anne L Kinney, Jan Koornneef, and Thaisa Storchi-Bergmann. The dust content and opacity of actively star-forming galaxies. *The Astrophysical Journal*, 533(2):682, 2000.

[92] Jason A Cardelli, Geoffrey C Clayton, and John S Mathis. The relationship between infrared, optical, and ultraviolet extinction. *Astrophysical Journal, Part 1 (ISSN 0004-637X), vol. 345, Oct. 1, 1989, p. 245-256.*, 345:245–256, 1989.

[93] Stéphane Charlot and S Michael Fall. A simple model for the absorption of starlight by dust in galaxies. *The Astrophysical Journal*, 539(2):718, 2000.

[94] AC Carnall, RJ McLure, JS Dunlop, and R Davé. Inferring the star formation histories of massive quiescent galaxies with bagpipes: evidence for multiple quenching mechanisms. *Monthly Notices of the Royal Astronomical Society*, 480(4):4379–4401, 2018.

[95] Gabriel B Brammer, Pieter G van Dokkum, and Paolo Coppi. Eazy: a fast, public photometric redshift code. *The Astrophysical Journal*, 686(2):1503, 2008.

[96] Benjamin D Johnson, Joel Leja, Charlie Conroy, and Joshua S Speagle. Stellar population inference with prospector. *The Astrophysical Journal Supplement Series*, 254(2):22, 2021.

[97] Denis Burgarella, Veronique Buat, and Jorge Iglesias-Paramo. Star formation and dust attenuation properties in galaxies from a statistical ultraviolet-to-far-infrared analysis. *Monthly Notices of the Royal Astronomical Society*, 360(4):1413–1425, 2005.